HIGH RESOLUTION DIRECTION OF ARRIVAL ESTIMATION ANALYSIS AND IMPLEMENTATION IN A SMART ANTENNA SYSTEM

by

Ahmed Khallaayoun

A dissertation submitted in partial fulfillment
of the requirements for the degree

of

Doctor of Philosophy

in

Electrical Engineering

MONTANA STATE UNIVERSITY
Bozeman, Montana

May, 2010

APPROVAL

of a dissertation submitted by

Ahmed Khallaayoun

This dissertation has been read by each member of the dissertation committee and has been found to be satisfactory regarding content, English usage, format, citation, bibliographic style, and consistency and is ready for submission to the Division of Graduate Education.

Dr. Richard Wolff

Approved for the Department of Electrical and Computer Engineering

Dr. Robert Maher

Approved for the Division of Graduate Education

Dr. Carl A. Fox

STATEMENT OF PERMISSION TO USE

In presenting this dissertation in partial fulfillment of the requirements for a doctoral degree at Montana State University, I agree that the Library shall make it available to borrowers under rules of the Library. I further agree that copying of this dissertation is allowable only for scholarly purposes, consistent with "fair use" as prescribed in the U.S. Copyright Law. Requests for extensive copying or reproduction of this dissertation should be referred to ProQuest Information and Learning, 300 North Zeeb Road, Ann Arbor, Michigan 48106, to whom I have granted "the exclusive right to reproduce and distribute my dissertation in and from microform along with the non-exclusive right to reproduce and distribute my abstract in any format in whole or in part."

Ahmed Khallaayoun

May, 2010

ACKNOWLEDGEMENTS

My deepest thanks go to my Prof. Richard Wolff and Dr. Yikun Huang. I thank them for their support, care, encouragements, and for giving me the opportunity to pursue my doctoral studies under their supervision. I would also like to thank my mentor, Mr. Andy Olson for always being there for me and for all the help and support both professionally and personally. I thank my fellow graduate students and colleagues, Raymond Weber, Will Tidd, and Aaron Taxinger for their valuable help and team spirit. In addition, I would like to thank the committee members for all their valuable help.

I would like to thank Montana Board of Research and Commercialization Technology (MBRCT # 07-11) and Advanced Acoustic Concepts (AAC) for their financial contributions and their interest in our research.

I would also like to give my utmost respect, love, and thanks to my parents, Abdelwahed Khallaayoun and Soad Benohoud, and my sisters Houda and Sara for their unconditional and constant love and support.

Most of all, I would like to thank God, for the blessings and sound belief in Him, health, and sanity and for putting me in a path that allowed me to meet people that have been kind to me and allowing me the opportunity to reciprocate

TABLE OF CONTENTS

TABLE OF CONTENTS - CONTINUED

LIST OF TABLES

Table Page

LIST OF FIGURES

Figure Page

LIST OF FIGURES - CONTINUED

Figure Page

LIST OF FIGURES - CONTINUED

Figure Page

LIST OF FIGURES - CONTINUED

Figure Page

ABSTRACT

The goal of this research is to equip the smart antenna system designed by the telecommunication group at the department of Electrical and Computer Engineering at Montana State University with high resolution direction of arrival estimation (DOA) capabilities; the DOA block should provide accurate estimates of emitters' DOAs while being computationally efficient. Intensive study on DOA estimation algorithms was carried out to pinpoint the most suitable algorithm for the application of interest, and the spectral methods were chosen for this study. The outcome of the study consisted of generating a novel algorithm, spatial selective MUSIC, which is comparable in accuracy to other high resolution algorithms but does not require the intensive computational burden that is typical of high resolution spectral methods. Spatial selective MUSIC is compared in terms of bias, resolution, robustness and computational efficiency against the most widely used DOA estimation algorithms, namely, Bartlett, Capon, MUSIC, and beamspace MUSIC. The design, troubleshooting, and implementation of the hardware needed to implement the DOA estimation in a real case scenario was achieved. Two design phases were necessary to implement the center piece of the hardware needed to achieve DOA estimation. The 5.8 GHz 8 channel receiver board along with a casing that egg crates the RF channels for channel-to-channel isolation was designed and built. A National Instrument data acquisition card was used to simultaneously sample all the 8 channels at 2.5 MSPS, the data was processed using the PC interface built in LabView. Phase calibration that accounts for the overall system magnitude and phase differences along with a novel calibration method to mitigate the effects of magnitude and phase variations along with mutual coupling was produced during this research and was imperative to achieving high resolution DOA estimation in the lab. The DOA estimation capabilities of the built system was tested within the overall smart antenna system and showed promising results. The overall performance enhancement that the DOA estimation block can provide cannot however be fully realized until the beamforming block is revised to provide accurate and deep null placing along with a narrower beam width. This cannot be achieved with the current system due to limitations in the number of the array elements used and the granularity in the phase shifters and attenuators used in the analog beamformer.

CHAPTER ONE

INTRODUCTION

Providing connectivity in rural and sparely populated areas remains the last hurdle in achieving a ubiquitous and worldwide network. Relying on conventional infrastructure will be inefficient and costly. Smart antennas in conjunction with recently emerging radio standards may prove to be a feasible, efficient, and reliable alternative. By being able to determine and track the directions of users in the coverage area and directionally transmit and receive, smart antennas will enhance the ability of the new radio standards (e.g. WiMAX) in terms of coverage, quality of service, and throughput [1]. The demand for global connectivity has seen an increase in the last decade especially in rural and sparsely populated areas where the lack of infrastructure leaves most occupants with little or no connectivity. Applications for the proposed approach extend beyond providing connectivity to sparsely populated areas to other commercial applications, namely use in animal tracking, farming and agriculture, avalanche victims localization, backup to already existing system (e.g. airport radar systems) in case of massive failure. In addition, DOA estimation is important for military tactical operations, public safety, and interference reduction in existing communication systems which will result in capacity enhancement.

The concept of adaptive antennas [2, 3] is not new and has been developed decades ago. Early smart antennas were designed for governmental use in military applications, which used directional beams to hide transmissions from an enemy. Implementation required very large antenna structures and time-intensive processing

along with significant financial input. With the advancements in digital signal processing, adaptive smart antenna systems (ASASs) have received an enormous interest lately. Compared to a conventional omnidirectional antenna, ASASs offer the benefit of increased gain (range), reduced interference, provide spatial diversity, and are power efficient [4]. Merging ASASs with new generation radio system promises an even greater potential.

In our open loop adaptive approach, the first and critical step into establishing communication in an ASAS is to spatially map the system's coverage area. Having the latter information readily available enables the beamformer to optimally form beams towards the users and suppress interferences. The scope of this research consists of introducing Direction of Arrival (DOA) estimation capabilities to the ASAS. The DOA estimation module should provide accurate and high resolution 2-D (azimuth plan) bearing estimates while being computationally efficient. In the context of sparse networks reducing the computational burden is possible since the numbers of users and interferers are limited.

In addition to providing the bearings of users in sparse networks which is imperative in controlling directional antennas in a communication system, DOA estimation can be used to find the positions for shipwrecked people. The latter can be achieved by use of triangulation of bearings provided by multiple arrays.

To achieve the mentioned scope a number of tasks were carried out. The first step consisted of an in-depth study of DOA estimation algorithms that included an intensive simulation study. The study led to a novel algorithm that provides high resolution

estimates while being computationally efficient compared to conventional high resolution DOA estimation algorithms (e.g. MUSIC and beamspace MUSIC), the Spatial Selective MUltiple SIgnal Classification or S2-MUSIC was first discussed in [5]. Conventional and subspace based spectral algorithms were considered in this work.

The design and implementation of the necessary hardware to prove the feasibility of high resolution DOA estimation was achieved. Two design phases were carried out to build the hardware. The first generation hardware was built for proof of concept, where DOA estimates of a single source and multiple sources showed promising results. A second generation hardware, where significant improvements have been added, was also designed and implemented. Improvements such as high channel-to-channel isolation, better end-to-end gain, symmetry in RF and local oscillator (LO) drive were added along with mechanical stability. In addition, the LO distribution along with the variable gain control were all integrated within the same board.

The DOA estimation block used relies on a path that is independent from the beamformer signal path, making the adaptive smart antenna system open loop. The open loop approach was chosen over the closed loop design because systems using the latter exhibit performance functions that do not have unique optima and might converge to a local optimum, or even worse, the algorithm might diverge. In addition, in any closed loop system the desired signal must be known in advance (or its reference must be known in advance) while the open loop approach is a blind approach and does not need knowledge of the signal. Finally, in closed loop system, instability becomes a concern.

Though theoretically subspace DOA estimation algorithms are shown to approach the Cramér–Rao Bound (CRB) under the right conditions (high signal to noise ratio (SNR) and sample rate) [6], practically, many DOA estimation systems failed to come even close to the predicted theoretical performance. The key to improving on previous systems consists of building the right hardware that exhibit high channel-to-channel isolation along with stable phase and gain across all channels. Mitigating the element-to-element mutual coupling in the antenna array remains a key component into achieving accurate bearing estimates. In addition, mutual coupling mitigation proved crucial to achieving high resolution DOA estimation performance. A calibration approach is discussed in chapter VI that significantly improves the performance of the estimates.

My contribution to this field of research consists of generating a novel DOA estimation algorithm, namely, S2 MUSIC that is suited best for rural and sparse networks but not necessarily limited to it. In addition, I have used a variety of engineering tools to design and implement a hardware design that partially or fully mitigates the factors leading to degrading the performance of the DOA estimation block in the adaptive smart antenna system. Finally, data post processing which included a calibration method was necessary to improve the system's performance.

In the chapter that follows, a concise background on smart antenna systems with an emphasis on the fundamentals of direction finding using an 8 element uniform circular array is presented. Chapter three is dedicated to explaining the mechanisms of conventional and high resolution direction finding algorithms in general and the S2-MUSIC algorithm in particular. Simulation results are presented in chapter four where

all the algorithms are compared in terms of bias, resolution, and computation needs. Chapter five discusses the design and implementation of the DOA estimation block hardware and final test results are presented in chapter six. Chapter seven contains conclusions pertaining to the presented research and suggested future work.

CHAPTER TWO

TECHNOLOGY AND BACKGROUND

This chapter explains the concept of ASAS and introduces the fundamentals of DOA estimation. By definition, a smart antenna shapes a pattern according to various optimization criteria. When the term “smart” is associated with “antenna” it implies the use of signal processing, giving the system the ability to shape the beam pattern according to particular conditions. Smart antennas are also referred to as digital beamforming (DBF) arrays when digital processing is performed, and when adaptive algorithms are employed the term adaptive arrays is used. Compared to omidirectional antennas, an ASAS offers increased gain, lower interference, spatial diversity and improved power efficiency making it a very attractive solution to a system requiring range or capacity. ASAS are also useful when the network topology is dynamic because of its ability to track mobile users and interferers.

Adaptive Smart Antenna System Description

The ASAS test bed designed by our group contains, as shown in Figure 1, a radio module (e.g. WiMAX radios, Airspan radios, Harris radios….) consisting of a Base Station (BS) and Subscriber Station(s) (SS), a horn antenna (or multiple antennas each connected to a different SS), an eight element Uniform Circular Array (UCA), a receiver board, a beamformer board, a Data AcQuisition (DAQ) system along with a PC interface.

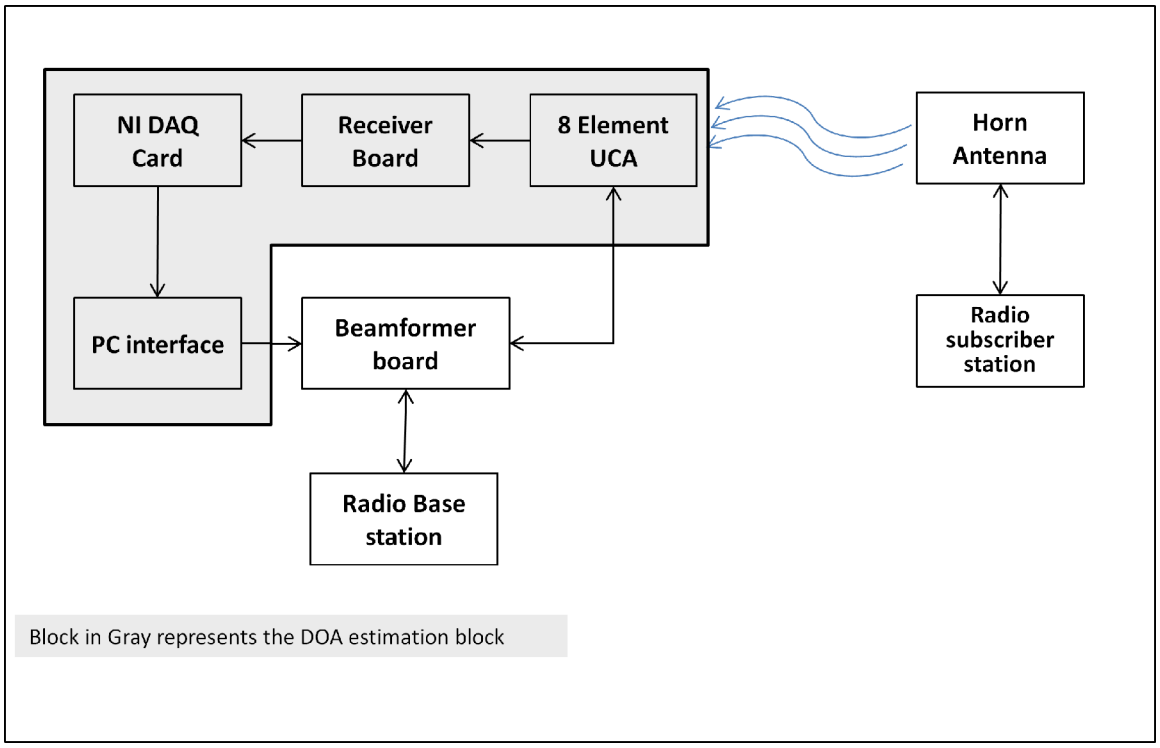

Figure 1 Adaptive smart antenna system major components

The adaptive smart antenna system beamforming procedure which operates at 5.8GHz starts by locating the bearings of the users and interference sources using the DOA estimation block. Once the impinging signals are acquired the processing is done via the PC which exploits a variety of algorithms to estimate the bearings of users and interference sources. The next step consists of calculating the appropriate weights necessary to form beams toward the desired users and to form nulls in the directions of interference signals. The beamforming and nullsteering are achieved by translating the calculated weights into phase and magnitude settings (for the array elements) which are sent to a DAQ card incorporated in the beamformer then to the CPLD (Complex Programmable Logic Device). Both the DAQ card and the CPLD are incorporated in the

beamformer board. The beamforming algorithms used are based on cophasal beamforming (on transmission) and nullsteering (on reception). The radio's incoming or outgoing signals are fed to the beamforming board and become subject to spatial multiplexing. The beamforming capabilities of the system will not be discussed in details. The interested reader can refer to [7] and for beamforming techniques one can refer to [8].

Uniform Circular Array

The 8 element UCA used in the system is an eight element circular array with an electric size $\beta\rho = 3.05$, where β is the wave-number and ρ is the antenna array radius. Each element is a monopole mounted on a ground skirt as shown Figure 2.

Figure 2 8 element UCA on a ground skirt

The UCA was designed to operate at a center frequency of 5.8 GHz. The choice of a UCA came from the fact that in such geometry, a 360 degree beam steering can take place in the azimuth plane without a significant effect on the beam-shape along with the

fact that effects of mutual coupling are easily compensated because of the basic symmetry in the UCA. In addition, no azimuthal angular estimation ambiguity is inherent in the system as is the case of uniform linear arrays.

Receiver Board

The receiver board is designed to translate the impinging signals from 5.8 GHz to baseband and to deliver the information to the Data AcQuisition (DAQ) Card or A/D board. The RF signal is amplified, filtered and mixed using a distributed Local Oscillator (LO) (the signal from one local oscillator was distributed via power division to all the eight channels in the board to provide mixing to all the channels simultaneously). The oscillator can be tuned to any desired frequency within the LO band enabling the RF signals to be down-converted to baseband for DOA estimation. Two versions of the receiver board were implemented. For the first version, a maximum baseband signal bandwidth of 1 MHz was used since the maximum sampling frequency of the data acquisition system is 2.5 MSPS. Manual gain control settings are used to provide an acceptable level to the DAQ card.

The second version of the board consists of integrating all the parts into one four layer board, namely, the local oscillator and the variable gain control which were separate parts in the first version. In addition, the board was designed to acquire signals that are 1 MHz and 10 MHz wide, the latter addition was necessary to accommodate for wideband signals (e.g. WiMAX) which are up to 10MHz wide. To mitigate co-channel interference at RF, an enclosure was designed to provide isolation between channels. The details of design and implementation of the receive board is discussed in chapter four.

Beamformer Board

The beamformer module forms beams toward desired users and places nulls in the interference bearings. As depicted in Figure 3, the beamformer board consists of an 8 way power divider/combiner which splits/combines the signal into/from 8 channels, each channel contains an analog phase shifter and attenuator controlled by an FPGA. The latter acquires the calculated weights from the PC interface and translates them into phase and magnitude settings for the currents driving the elements in the antenna array. The switch allow the beamformer to perform in transmit or receiver mode. The beamformer was designed by the communication group at MSU and is shown in Figure 4 [9]. A detailed schematic of the beamformer board is given in Appendix A.

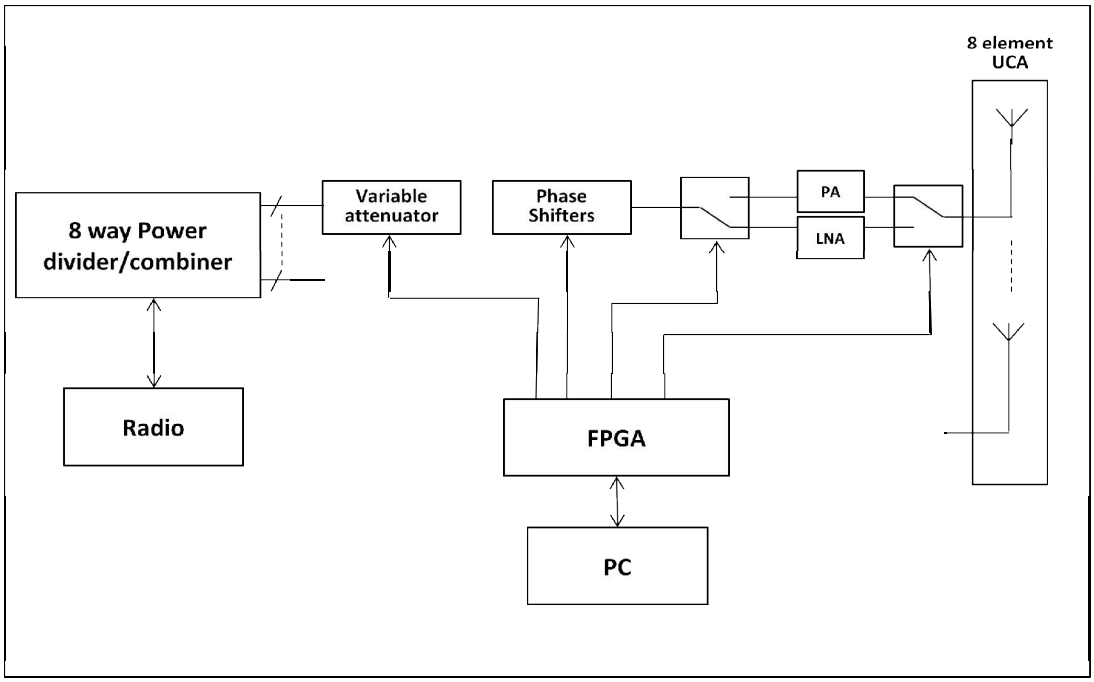

Figure 3 Simplified block diagram of the beamformer board

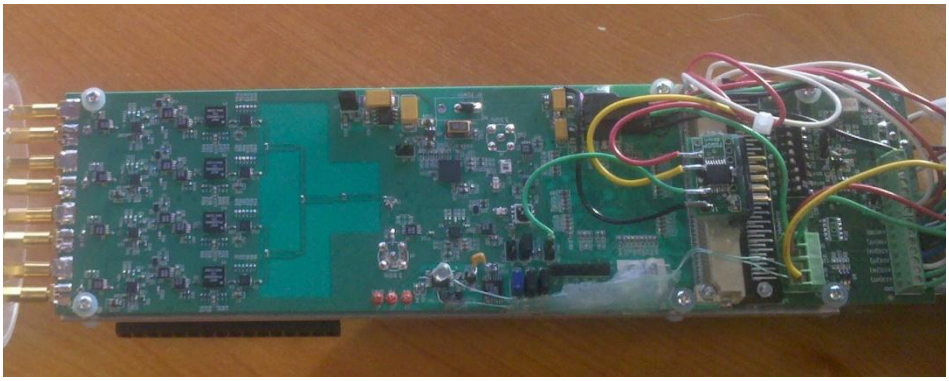

Figure 4 The beamformer board designed
by the MSU communication group

An anechoic chamber measurement comparing the measured accuracy of the pointing angle, the height of the sidelobes and the depth the nulls with simulation results was carried out. Figure 5 depicts a comparison of a measured beam pattern with the simulated pattern with cophasal beamforming.

The simulated and measured beams are very similar. The measured maximum beam point is within a few degrees of the expected bearing. The sidelobes measured were at the same location and just a few dB higher than the simulated results. The beamforming hardware and algorithms performed very well and almost matched the simulation results. Cophasal excitation and several window beamforming algorithms, including a Chebyshev window beamforming were tested and showed comparable results to theoretical expectations.

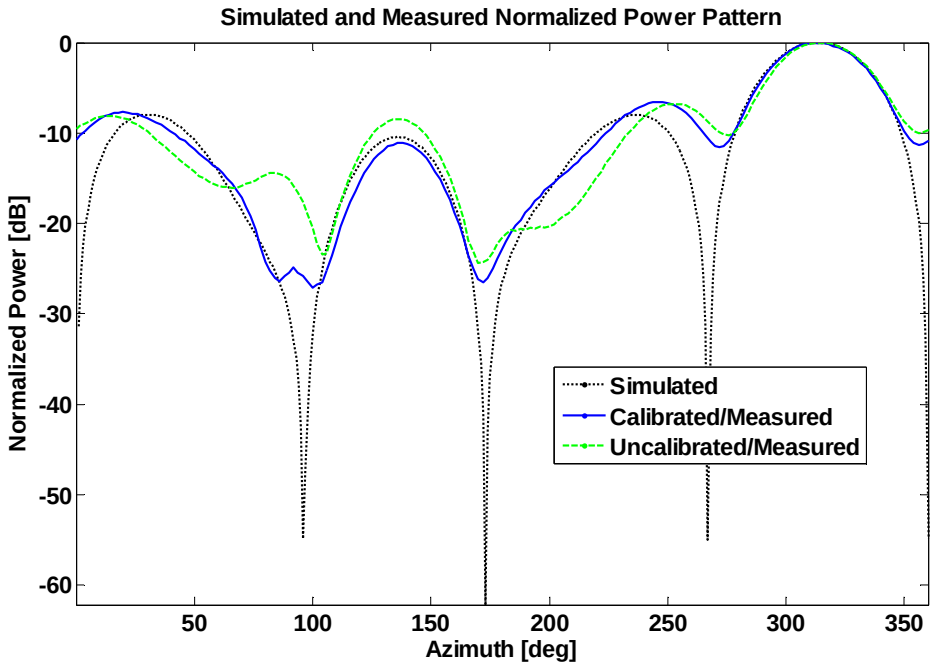

Figure 5 Comparison of simulation with measured results for beamforming [10]

For nullsteering, our group used the algorithm discussed in [11]. The results indicated that the null in the measured pattern is about 3degrees away from the interference location. The depth of the null was measured as -22 dB. Due to the granularity of the phase shifters (5.6 degrees steps) and attenuators (0.5 dB steps), accurate and deep nulls are hard to achieve with the current hardware. In [7], the author mentions that the beamformer performs well when shift and sum beamforming is applied but for better nullsteering finer resolution control over gain and phase are needed to achieve satisfactory nullsteering. Calibration for the beamformer board was imperative to achieving beams with the desired beam shape and pointing angle. The beamformer calibration is discussed in details in [10].

DAQ Card

A National Instrument (NI) PCI6133 DAQ card is used in the current system. The card is able to sample at a maximum rate of 2.5 Mbps per channel (8 channels simultaneously). A BNC-2110 Noise-Rejecting BNC I/O Connector Block was also used as intermediary between the receiver output and the DAQ card, and used a SH68-68-EP Noise-Rejecting Shielded Cable. Figure 6 shows the data acquisition system.

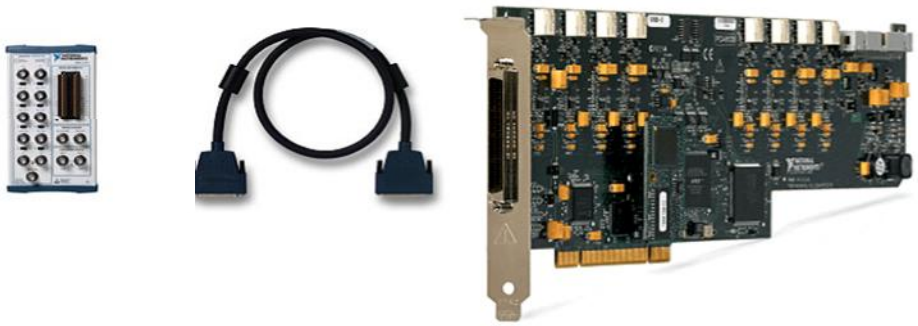

Figure 6 Data acquisition system used
(Pictures acquired from the NI website)

For faster sampling, to capture the full bandwidth of the a WiMAX signal, an A/D board with two quad, 8-bit, and serial LVDS A/D converters running at a sampling rate of 25 MSPS was designed by our group. Before addressing memory issues with the current A/D board, the lab tests carried out using the second generation receiver board relied on the NI DAQ card.

DOA Estimation Fundamentals

Steering Vector

A steering vector that has a dimension equal to the number of elements in the antenna array can be defined for any antenna. It contains the responses of all elements of the array to a source with a single frequency component of unit power. The steering vector exhibits an angular dependence since the array response is different in different directions. The array geometry defines the uniqueness of this association. For an array of identical elements, each component of this vector has unit magnitude. The phase of its n^{th} component is equal to the phase difference between signals induced on the m^{th} element and the reference element due to the source associated with the steering vector. The reference element usually is set to have zero phase [12]. Sometimes, the steering vector is referred to in the literature as the space vector, array response vector or the array manifold when the subspace approach is considered.

Considering a uniform circular array with radius ρ and M identical elements, the phase difference relative of the m^{th} element of the array relative to element M is given as:

$$\Delta\varphi_m = 2\pi\left(\frac{m}{M}\right), m = 1, 2, \dots, M \qquad \text{Eq 1}$$

If we assume that the wavefront passes through the origin at time $t = 0$, then the wavefront impinges the m^{th} element at time,

$$\tau_m = -\frac{\rho}{c}\sin\theta\cos(\varphi - \Delta\varphi_m), \qquad m = 1, 2, \dots, M \qquad \text{Eq 2}$$

where, c is the speed of light in free space and θ is the elevation angle. One should note that negative time delay mean that the wavefront hits the elements before it passes the origin and a positive time delay means that the wavefront hits the element after it has passed the origin. The element space circular array steering vector is given by

$$\vec{a}(\varphi) = \left[e^{\beta\rho \sin\theta \cos(\varphi-\Delta\varphi_1)},\ e^{\beta\rho \sin\theta \cos(\varphi-\Delta\varphi_2)}, \ldots, e^{\beta\rho \sin\theta \cos(\varphi-\Delta\varphi_m)}\right]^T \qquad \text{Eq 3}$$

where, $\beta = \frac{2\pi}{\lambda}$ is the wave number, $\vec{\ }$ represents the vector notation, and superscript T is the transpose operator. The elevation dependence in the steering vector is on $\beta\rho \sin\theta$ while the azimuth dependence is on $\cos(\varphi - \varphi_m)$. For a full derivation of the steering vector of a UCA, one can refer to [13, 14]. The reader should note that the UCA we are using consists of 8 dipoles over a ground plane, Eq 3 is an approximation that is valid for $0 \leq \theta \leq \frac{\pi}{4}$. The use of dipoles over a ground plan introduces a beam tilt in the elevation compared to a UCA with monopole.

Received Signal Model

Throughout the algorithm study the prevailing signal model that is used is described in this section. Let us consider a uniform circular array with M identical elements or sensors. The elements are simultaneously sampled and produce a vector as a function of time $\vec{x}(t)$ which might contain information from one or multiple emitters. Let us assume *K* uncorrelated narrowband sources (in other words, the signals are not a scaled and delayed version of each other) impinging on the array, the narrowband assumption dictates that as the signal propagates through the array its envelope remains

unchanged which holds true in our case since the operating frequency is much larger than the signal bandwidth. The latter assumption also means that the receiving system is linear, hence enabling the use of superposition. Noise is assumed additive, and is added to $\vec{x}(t)$. The output vector takes the form shown in Eq 4:

$$\vec{x}(t) = \sum_{k=1}^{K} \vec{a}\,(\varphi_k) s_k(t) + \vec{n}(t) \qquad \text{Eq 4}$$

The steering vector $\vec{a}(\varphi_k) \epsilon\, \mathbb{C}^M$, which is of size $M \times K$, and $s_k(t)$ represents the incoming plane wave from the k^{th} source at time *t* impinging from a particular direction φ_k. $\vec{n}(t) \epsilon\, \mathbb{C}^M$ represents noise which can be either inherent in the incoming signals themselves or due to instrumentation. The reader should note that the term "snapshot" represents a single observation of the vector $\vec{x}(t) \epsilon\, \mathbb{C}^M$, in other words, a single sample of $\vec{x}(t)$ which represents the complex baseband equivalent received signal vector at the antenna array at time t.

In matrix notation one can rewrite Eq 4 as:

$$\vec{x}(t) = \vec{A}\vec{s}(t) + \vec{n}(t) \qquad \text{Eq 5}$$

where, $\vec{A} = [\vec{a}(\varphi_1), \vec{a}(\varphi_2), \ldots, \vec{a}(\varphi_K)]$ represents the array response matrix, each signal source is represented by a column in $\vec{A} \epsilon\, \mathbb{C}^{M \times K}$. $\varphi = [\varphi_1, \varphi_2, \ldots, \varphi_K]$ represents the vector of all the DOAs. $\vec{s}(t) = [s_1(t), s_2(t), \ldots, s_k(t)]$ represents the incoming signal in phase and amplitude from each signal source at time *t*, where $\vec{s}(t) \epsilon\, \mathbb{C}^K$.

The Nyquist sampling criterion should be met to allow reconstruction of the baseband signal occupying B bandwidth (sampling frequency $\geq$ 2B). A set of data observation of the form below can be formed where *T*, the number of samples is larger then *K*.

$$\vec{X} = [\vec{x}(1), \vec{x}(2), .., \vec{x}(T)] \quad \text{Eq 6}$$

$$\vec{S} = [s(1), s(2), .., s(T)] \quad \text{Eq 7}$$

$$\vec{N} = [\vec{n}(1), \vec{n}(2), .., \vec{n}(T)] \quad \text{Eq 8}$$

Where $\vec{X} \epsilon \mathbb{C}^{M \times N}$ and $\vec{S} \epsilon \mathbb{C}^{K \times N}$, For convenience we rewrite Eq 5 as,

$$\vec{X} = \vec{A}\vec{S} + \vec{N} \quad \text{Eq 9}$$

Subspace Data Model and the Geometrical Approach

When subspace methods are of interest, methods of linear algebra, multidimensional geometry along with multivariate statistics are needed. A look at the problem from a geometrical perspective is imperative to understanding the algorithm mechanics.

Array Manifold and Signal Subspaces

Vectors $\vec{a}(\varphi_i)$, the columns of $\vec{A}$, are elements of a set (not a subspace), termed array manifold, in other words, the set of array response vectors corresponding to all possible direction of arrival. Each element in the array manifold a_{ij} $(i = 1, 2, \ldots, K\,; j = 1, 2, \ldots, M)$ corresponds to the response of the j^{th} element to a signal incident from the direction of the i^{th} signal. It is imperative to have complete knowledge of the array manifold either estimated analytically or via measurement. To achieve a DOA estimate using the subspace methods for the UCA used in this research, the array manifold was extracted analytically and is shown in Eq 3.

An array manifold is said to be unambiguous if any collection of $K \leq M$ distinct vectors from the array manifold form a linearly independent set. If the latter is violated, the two vectors $\vec{a}(\varphi_1), \vec{a}(\varphi_2)$ will be linearly dependent which is analogous to saying that $\varphi_1 = \varphi_2$, making the distinction between the two angles inherently impossible. In this case, the array manifold is said to be ambiguous.

Another unwanted possibility consists of having a signal subspace with rank less than *K*. The situation might rise when the sample matrix $\overrightarrow{S}$ has rank less then *K*, which means that the signals of interest are a linear combination of each other. These signals are known as coherent or fully correlated signals. The same situation may rise in a case where multipath is prominent and also if the samples used are fewer then the signal sources.

The output vector $\vec{x}(t)$ can be thought of as a sequence of *M* dimensional vectors. The *M* dimensional vector space has axes defined by the unit orthogonal vectors corresponding to *M* individual antennas. Basically, $\vec{x}(t)$ spans the *K* dimensional subspace which means that it is confined to the signal subspace. When only one signal source is present the received vector $\vec{x}(t)$ is confined to a one dimensional subspace which is a line though the origin defined by $\vec{a}(\varphi_1)$. The received vector amplitude can vary but its direction cannot. When two signal sources are present, $\vec{x}(t)$ is the weighted vector sum of the vectors due to each source, and in this case $\vec{x}(t)$ is confined the plane spanned by the vectors $\vec{a}(\varphi_1)$ and $\vec{a}(\varphi_2)$. In general, when *K* independent sources are present, $\vec{x}(t)$ is confined to a *K* dimensional subspace of $\mathbb{C}^M$. The subspace is denoted the signal subspace since it is defined by the number of signals impinging on the array.

Intersections as Solutions

In the absence of noise and assuming uncorrelated signal sources, one can visualize a solution. The output of the array lies in the K dimensional subspace of $\mathbb{C}^M$ spanned by the columns of $\overrightarrow{A}$. Once K independent vectors are observed, the signal subspace becomes known and the intersections between the signal subspace and the array manifold representing the solutions as illustrated in Figure 7. Each intersection corresponds to a response vector of one of the signals. When two signals are present and three intersections occur between the signal subspace and the array manifold, the manifold is deemed ambiguous.

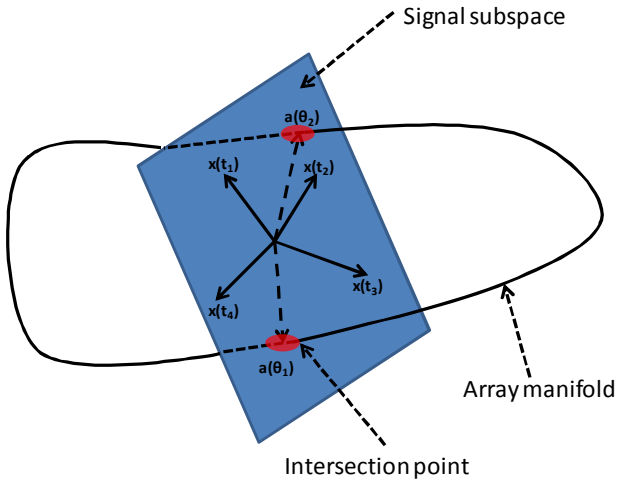

Figure 7 Intersection as a solution in the absence of noise

Additive Noise

Noise can infiltrate the array measurements either internally or externally. Internal noise is due to the receiver electronics (thermal noise, quantization effects, channel to channel interference…, etc.). External noise can be caused by random

background radiation and clutter, in addition to any factor that might produce an array manifold that is different from the assumed one (wideband signals, near field signals…, etc.).

It is often assumed that the noise is zero mean and additive. More particularly, the noise is assumed to be a complex stationary circular Gaussian random process. It is further assumed to be uncorrelated from snapshot to snapshot. The spatial characteristics which are important to the subspace approach are discussed in the next section.

Second Order Statistics

Since the parameters of interest in DOA estimation are spatial in nature, one would require the cross covariance information between the various antenna elements. The received signal estimated covariance matrix R_{xx} is defined as [15]:

$$\vec{R}_{xx} = E\{\vec{x}(t)\vec{x}^H(t)\} \quad \text{Eq 10}$$

If limited sampling is used,

$$\vec{R}_{xx} = \frac{1}{T}\sum_{t=1}^{T} \vec{x}(t)\vec{x}^H(t) \quad \text{Eq 11}$$

where $E\{.\}$ denotes the statistical expectation and superscript H denotes the Hermitian or the complex conjugate transpose matrix operation, T denotes the number of samples of snapshots used. Eq 10 can be further written as:

$$\vec{R}_{xx} = \vec{A}E\{s(t)s^H(t)\}\vec{A}^H + E\{\vec{n}(t)\vec{n}^H(t)\} \quad \text{Eq 12}$$

The desired signal covariance matrix R_{ss} is defined in Eq 13 and the noise covariance matrix is defined in Eq 14 :

$$\vec{R}_{ss} = E\{s(t)s^H(t)\} \quad \text{Eq 13}$$

$$\vec{R}_{nn} = E\{\vec{n}(t)\vec{n}^H(t)\} \quad \text{Eq 14}$$

Most of the algorithms require that the spatial covariance of the noise be known and is denoted as

$$\vec{R}_{nn} = \sigma^2\vec{\Sigma} \quad \text{Eq 15}$$

where, σ^2 is the noise power and $\vec{\Sigma}$ is normalized such that det($\vec{\Sigma}$) = 1. By further assuming that the noise is spatially white ($\vec{\Sigma} = \vec{I}$) one can rewrite Eq 12,

$$\vec{R}_{xx} = \vec{A}\,\vec{R}_{ss}\vec{A}^H + \sigma^2\vec{I} \quad \text{Eq 16}$$

The source covariance matrix is assumed to be full-rank (nonsingular). In other words, the signals are non-coherent which make the columns of R_{ss} linearly independent. In the case where the signals are coherent, R_{ss}will be rank deficient or near singular for highly correlated signals.

Assumptions and Their Effects on DOA Estimation

In practice, assuming knowledge of the array response vector and the noise covariance matrix is not valid, and if not taken into account will degrade the system performance significantly. When taking calibration measurements, phase and magnitude errors are inherent in these measurements, which will yield lower performance than theoretical expectations. In estimating the array response vector (in our case analytically), one is assuming identical elements which in practice is very hard to achieve. In addition, the element locations within the array are not highly accurate unless machined with very high precision. The degree of degradation depends highly on how

the estimated array response vector differs from its nominal value [16]. The latter motivated the investigation on how the phase and amplitude error affect the performance of the DOA estimation algorithms accuracy and resolution. The results are shown in Chapter three.

The assumption that the noise is white Gaussian is not critical when the system's SNR is high since the noise does not contribute significantly to the statistics of the signal received by the array. In low SNR cases, however, severe degradation of the performance will occur spatially in subspace methods.

CHAPTER THREE

DIRECTION OF ARRIVAL ESTIMATION ALGORITHMS AND SIMULATION RESULTS

DOA estimation requires estimating a set of constant parameters that depend on true signals in a noisy environment. When the impinging waveforms reach the antenna elements, a set of signals (sampled data) is gathered and used to estimate the locations of the emitters. Throughout the literature one can find a multitude of approaches to solving this problem. The next section presents a chronological literature review on the progress made in DOA estimation algorithms and the following sections will describe in detail the mechanisms behind conventional and subspace-based spectral algorithms.

Literature Review

Attempts to perform wireless direction finding date back to the early years of the 20^{th} century, Belinni and Tosi [17] along with Marconi [18] attempted to use directive characteristics of antenna elements to perform direction finding. Attempts to make use of multiple antennas for direction finding were proposed by Adcock [19] and Keen [20].

Though technological advances, such as electronics enabling accurate phase and amplitude measurement and high speed processing, were imperative to the evolution of direction finding, algorithm development by many authors propelled direction of arrival estimation to become highly accurate and able to provide very high resolution results. The first attempt to automatically estimate the locations of emitters using sensor arrays was presented in 1950 by Bartlett [21]. The method applied classical spectral Fourier

analysis to spatial analysis. For a give input signal, the Bartlett algorithm maximizes the power of the beamforming output. The Bartlett method, however, shares the same resolution as the Periodogram, and it is mainly dependent on the beamwidth, which is governed primarily by the number of elements used in the antenna array [22]. In 1967, Burg in [23] presented the now well recognized maximum entropy (ME) spectral estimate, which is derived from a linear prediction filter. The leading coefficient for the filter is unity, and the remaining coefficients are chosen to minimize its expected output power or the predicted error. Capon presented his famous method in [24]. It relies on the a simple yet elegant idea of putting a constraint on the gain of the array, constraining the latter to be unity in a given direction φ, while simultaneously minimizing the output power in other directions. This problem is easily solved by means of LaGrange multipliers as shown in chapter three. Variations of the Capon method were presented by Borgiottia and Kaplan in [25], the Adapted Angular Response (AAR), and Gabriel [26], the Thermal Noise Algorithms (TNA).

Subsequent to the methods mentioned above, which suffered from bias and sensitivity in parameter estimate limitations [27], Pisarenko [28] was the first to introduce the idea of exploiting the structure of the data model in parameter estimation in noise using the covariance approach. The high resolution method was based on the use of the projection onto the vector in the estimated noise subspace that corresponds to the smallest eigenvalue. The latter method was prone to often estimating false peaks. Independently, Schmidt [29, 30] and Bienvenue and Kopp [31] were the first to use the idea of exploiting the data model applied to sensor arrays of arbitrary form. A multitude of Eigen-space

spectrum based estimation methods followed in an attempt to improve their performance. Notably, the Min-Norm method proposed in [32] and [33], The beamspace method proposed in [34] and [35]. Paulraj and Roy in [36] and [37] proposed the estimation of signal parameters via rotational invariance techniques or ESPRIT. Other methods that showed promise in direction finding are the state space approach [38] and the matrix pencil approach [39].

Conventional DOA Estimation Algorithms

As mention above the first attempt to automatically localize signal sources using an antenna array was proposed by Bartlett. This method is referred to in the literature as the shift and sum beamforming method or Bartlett method, and is based on maximizing the power of the beamforming output for a given input signal. The other conventional method is known as the Capon algorithm, which adds the constraints of making the gain of the array unity in the direction of arrival and then minimizing the output power in the other directions.

Bartlett Algorithm

The Bartlett algorithm consists of combining the antenna outputs so that the signals at a given direction line up and add coherently (hence the name shift and sum). The latter is the fundamental method used in array processing applications. The signals will line up in phase if the proper delays (or phases in the case of narrowband signals) that correspond to a particular direction are applied to them, and the output signal at the receiver is consequently enhanced by a factor M. If a different set of weights is applied

that correspond to a different angle is applied the signals, they will not line up and will not add up coherently making the power at that angle lower. The signal power at the beamformer output will then be maximized at the direction that corresponds to the signal source. The array response is steered by forming a linear combination of the sensor outputs and is represented in

$$y(t) = \vec{w}^H \vec{x}(t) \qquad \text{Eq 17}$$

where $\vec{w}^H$ is the weight vector.

For a set of samples *T*, the output power can be written as

$$P(\varphi) = \frac{1}{T}\sum_{t=1}^{T} |y(t)|^2 = \frac{1}{T}\sum_{t=1}^{T} \vec{w}^H \vec{x}(t)\vec{x}^H(t)\vec{w} = \vec{w}^H \vec{R}_{xx}\vec{w} \qquad \text{Eq 18}$$

where, φ represents the azimuth angle. The goal is to find the best weights that maximize $P(\varphi)$, with a normalized steering vector such that $\vec{a}(\varphi)^H\vec{a}(\varphi) = \mathrm{I}$, one of the weight vectors that maximizes the power is $\vec{w}_{Bar} = \vec{a}(\varphi)$. Inserting the optimum weight in to the output power equation, the resulting Bartlett power spectrum is

$$P_{Bar}(\varphi) = \vec{a}(\varphi)^H \vec{R}_{xx}\vec{a}(\varphi) \qquad \text{Eq 19}$$

Capon Algorithm

In mathematical terms, given the array output power $P(\varphi) = \vec{w}^H\vec{R}_{xx}\vec{w}$, the gain is constrained to unity in the direction φ, in other words, $\vec{w}^H\vec{a}(\varphi) = 1$. Introducing a new variable λ or a Lagrange multiplier, one can write the Lagrange function as, $\vec{J}(w, \lambda) =$

$\vec{w}^H \vec{R}_{xx} \vec{w} - \lambda(\vec{w}^H \vec{a}(\varphi) - 1)$. Taking the derivative of J as a function of $\vec{w}$ and λ, the following two equations are obtained:

$$\frac{\partial \vec{J}}{\partial \vec{w}} = \vec{w}^H \vec{R}_{xx} + \lambda \vec{a}(\varphi) = 0 \quad \text{Eq 20}$$

$$\frac{\partial \vec{J}}{\partial \lambda} = \vec{w}^H \vec{a}(\varphi) - 1 = 0 \quad \text{Eq 21}$$

Performing a right-hand multiply in Eq 20 by $\vec{w}$ one can see that the power estimate and the Lagrangian are the same numerically. The Capon power estimate is obtained by solving for the weight in Eq 20 by replacing λ by P and substituting the result in the array output equation as shown below,

$$\vec{w}^H R_{xx} = P \vec{a}(\varphi) \quad \text{Eq 22}$$

$$\vec{w}^H = P \vec{a}(\varphi) \vec{R}_{xx}^{-1} \quad \text{Eq 23}$$

$$P = \vec{w}^H \vec{R}_{xx} \vec{w} = P \vec{a}(\varphi) \vec{R}_{xx}^{-1} \vec{R}_{xx} \left[\vec{R}_{xx}^{-1}\right]^H \vec{a}^H(\varphi) P^H \quad \text{Eq 24}$$

$$P_{Capon} = \frac{1}{\left[\vec{a}(\varphi)\left[\vec{R}_{xx}^{-1}\right]^H \vec{a}^H(\varphi)\right]^H} = \frac{1}{\vec{a}^H(\varphi) \vec{R}_{xx}^{-1} \vec{a}(\varphi)} \quad \text{Eq 25}$$

Subspace Based Algorithms

In this section two types of subspace based algorithms are discussed, namely, the element space MUSIC proposed by Schmidt and the beam-space MUSIC proposed by Mathews and Zoltowski [40]. Subspace based methods rely on using the orthogonality between the signal and noise subspaces to extract the DOA estimation solution. Other methods have been proposed to transform the element space to beamspace as in [41, 42],

but the one adopted in this research relied on using a beamformer that is completely based on the principle of phase mode excitation that transforms the element space into a real beamspace. The choice for the latter algorithm arose from the fact that the method reduces the size of the covariance matrix depending on the number of modes used to pre-multiply the receiver data vector. As will be discussed in subsequent sections, the reduction of the covariance matrix is also used in S2 MUSIC (without the need to pre-multiply receiver data vector) and this similarity will give an insight on how S2 MUSIC compares in performance to another algorithm that relies on the reduction of the covariance matrix.

MUSIC Algorithm

Based on the data model described earlier that is sampled *N* times,

$$\vec{X} = \vec{A}\vec{S} + \vec{N}$$

The complete data matrix $\vec{X}$ is of size $[M \times T]$, and $\vec{S}$ and $\vec{N}$ are of size $[K \times T]$ and $[M \times T]$, respectively. The steering vector $\vec{A}$ is of size $[M \times K]$. The complex impinging waveforms are represented in the columns of $\vec{S}$, and the noise at each element is represented in the columns of $\vec{N}$. For $\vec{A}$, which is also complex, the k^{th} column vector represents the M vector of array element responses to a signal waveform from direction φ_k. Based on the Schmidt method and based on Eq 16, and employing eigenvalue decomposition (EVD) on the received signal covariance matrix, R_{xx} can hence be represented by

$$\vec{R}_{xx} = \vec{A}\,\vec{R}_{ss}\vec{A}^{H} + \sigma^2\vec{I} = \vec{\mathrm{U}}\vec{\Lambda}\vec{\mathrm{U}}^{\mathrm{H}} \quad \text{Eq 26}$$

$\vec{\mathrm{U}}$ represents the unitary matrix (analogous to an orthonormal matrix if $R_{xx}$is real) and $\vec{\Lambda}$ is a diagonal matrix of real eigenvalues ordered in a descending order (first eigenvalue is largest)

$$\vec{\Lambda} = \mathrm{diag}\{\lambda_1, \lambda_2, \ldots, \lambda_{\mathrm{M}}\} \quad \text{Eq 27}$$

Any vector orthogonal to $\vec{A}$ is an eigenvector of $\vec{R}_{xx}$ with value σ^2 and there exist *M-K* such vectors. The remaining eigenvalues are larger than σ^2, which enables one to separate two distinct eigenvectors-eigenvalues pairs, the signal pairs and the noise pairs. The signal pairs are governed by the signal eigenvalues-eigenvectors pairs corresponding to the eigenvalues $\lambda_1 \geq \cdots \geq \lambda_{\mathrm{K}} \geq \sigma^2$, and the noise pairs are governed by the noise eigenvalues eigenvectors pairs corresponding to the eigenvalues $\lambda_{\mathrm{K+1}} = \cdots = \lambda_{\mathrm{M}} = \sigma^2$
One can further express the received signal covariance matrix as

$$\vec{R}_{xx} = \vec{\mathrm{U}}_{\mathrm{s}}\vec{\Lambda}_{\mathrm{s}}\vec{\mathrm{U}}_{\mathrm{s}}{}^{\mathrm{H}} + \vec{\mathrm{U}}_{\mathrm{n}}\vec{\Lambda}_{\mathrm{n}}\vec{\mathrm{U}}_{\mathrm{n}}{}^{\mathrm{H}}$$

where, $\vec{\mathrm{U}}_{\mathrm{s}}$ and $\vec{\mathrm{U}}_{\mathrm{n}}$ are the signal and noise subspace unitary matrices.

The key issue in estimating the direction of arrival consists of observing that all the noise eigenvectors are orthogonal to $\vec{A}$, the columns of $\vec{\mathrm{U}}_{\mathrm{s}}$ span the range space of $\vec{A}$ and the columns of $\vec{\mathrm{U}}_{\mathrm{n}}$span the orthogonal complement of $\vec{A}$. The orthogonal complement of $\vec{A}$ is in fact the nullspace of $\vec{A}^H$. By definition the projection operators onto the noise and signal subspaces are:

$$\vec{P}_s = \vec{U}_s\vec{U}_s^H = \vec{A}\left(\vec{A}^H\vec{A}\right)^{-1}\vec{A}^H \quad \text{Eq 28}$$

$$\vec{P}_n = \vec{U}_n \vec{U}_n^H = \vec{I} - \vec{A}\left(\vec{A}^H \vec{A}\right)^{-1} \vec{A}^H \quad \text{Eq 29}$$

Assuming $\vec{A}\,\vec{R}_{ss}\vec{A}^H$ is full rank (the signals are linearly independent), and since the eigenvectors in $\vec{U}_n^H$ are orthogonal to $\vec{A}$, it is clear that,

$$\vec{U}_n^H \vec{A} = 0, \varphi \in \{\varphi_1, \ldots, \varphi_K\} \quad \text{Eq 30}$$

Unless the steering vector ambiguous, the estimates will be unique. The estimated signal covariance matrix (from measurements) will produce an estimated orthogonal projection onto the noise subspace $\widehat{\vec{P}_n} = \widehat{\vec{U}_n}\widehat{\vec{U}_n^H}$. The MUSIC spatial "pseudo-spectrum" is defined as (from here forward the spatial "pseudo-spectrum" of subspace based methods will be referred to as spectrum from convenience):

$$P_{MUSIC}(\varphi) = \frac{1}{\vec{a}^H(\varphi)\,\widehat{\vec{P}_n}\vec{a}(\varphi)} \quad \text{Eq 31}$$

The MUSIC algorithm basically estimates the distance between the signal and noise subspaces, in a direction where a signal is present and since the two subspaces are orthogonal to each other, the distance between then at that very angle will be zero or near zero. Similarly, if no signal is present at a particular direction the subspaces are not orthogonal and the result will be zero.

Real Beamspace MUSIC

The beamspace method proposed in [40], relies on implementing a beamspace transformation to the UCA manifold $\vec{a}(\varphi)$ onto the beamspace manifold $\vec{b}(\varphi)$ employing the beamformer $\vec{T}_r^H$ (subscript r means that the beamformer synthesizes a real valued

beamspace manifold). It was noted by the authors in [40] that the highest order mode that can be excited by the aperture at a reasonable strength can be estimated as $T \approx \beta\rho$, where, β is the wave-number and ρ is the antenna array radius. In our case since $\beta\rho = 3.05$, the highest order mode that one can use is 3.

Another limitation concerns the relationship between the number of antenna elements and the highest mode number, $M > 2T$. If we consider a phase mode excitation for an M element UCA, the normalized beamforming weight vector that excites the array with phase mode t, while $|t| \leq T$ is

$$\vec{w}_t^H = \left[e^{jt\varphi_0}, e^{jt\varphi_1}, \ldots, e^{jt\varphi_{M-1}}\right] \quad \text{Eq 32}$$

where the angular position φ_m was defined in Eq 1. Another beamformer notation $\vec{T}_{pm}^H$ is introduced and it denotes the beamformer that is completely based on phase mode excitation.

$$\vec{a}_{pm}(\varphi) = \vec{T}_{pm}^H \vec{a}(\varphi) \quad \text{Eq 33}$$

The transformation makes $\vec{a}_{pm}(\varphi)$ centro-Hermitian and premultiplying it by $\vec{w}_t^H$, which has centro-Hermitian rows, leads to a real-valued beamspace manifold that in azimuth exhibits similar variation as a ULA Vandermonde structured array manifold,

$$\vec{T}_r^H = \vec{w}_t^H \vec{T}_{pm}^H \quad \text{Eq 34}$$

One should note that the manifolds synthesized are of dimension (T') lower than the original manifold $T' = 2T + 1$.

The beamformer matrix $\vec{T}_{pm}^H$ is defined as,

$$\vec{T}_{pm}^H = \vec{C}_v \vec{V}^H \quad \text{Eq 35}$$

where $\vec{C}_v = diag\{j^{-T}, \ldots, j^{-1}, j^0, j^{-1}, \ldots, j^{-T}\}$ and $\vec{V} = \sqrt{M}[\vec{w}_{-T} \vdots \cdots \vec{w}_0 \vdots \cdots \vdots \vec{w}_T]$. The vector $\vec{w}_t^H$ excites the UCA with phase modes t leading to a pattern $f_t^s = j^{|t|}J_{|t|}(\xi)e^{jt\varphi}$, where $\xi = \beta\rho \sin\theta$ and $J_t(\xi)$ is the Bessel function of the first kind of order t.

One can then deduce the beamspace manifold

$$\vec{b}(\varphi) = \vec{T}_r^H \vec{a}(\varphi) \qquad \text{Eq 36}$$

Extracting the spatial pseudo spectrum of the real beamspace MUSIC begins by applying the beamformer $\vec{T}_r^H$ to make the transformation from element space to beamspace to the data matrix $\vec{x}(t)$, resulting in a transformed data matrix

$$\vec{y}(t) = \vec{T}_r^H \vec{A}(\vec{\Phi})\vec{s}(t) + \vec{T}_r^H \vec{n}(t) = \vec{B}(\vec{\Phi})\vec{s}(t) + \vec{T}_r^H \vec{n}(t) \qquad \text{Eq 37}$$

$$\vec{R}_{yy} = \vec{B}\,\vec{R}_{ss}\vec{B}^H + \sigma^2\vec{I} \qquad \text{Eq 38}$$

Real eigenvalue decomposition is applied to $\vec{R}_{yy}$, resulting in a beamspace signal and noise subspace and extracting the spatial pseudo-spectrum is the same as described in the previous section. If the orthogonal projection onto the beamspace noise subspace is denoted $\vec{P}_{n-beam}$ then,

$$P_{Beam}(\varphi) = \frac{1}{\vec{b}^H(\varphi)\,\vec{P}_{n-Beam}\vec{b}(\varphi)} \qquad \text{Eq 39}$$

Spatial Selective MUSIC

A novel algorithm, namely, the spatial selective MUSIC (S2-MUSIC) was proposed by this author and reported in [5]. The method consists of two searches, namely, rough and smooth searches. In the rough search step, a standard switched beam

is used for spatial selective beamforming, the method previously chosen for the smart antenna system designed by our group. In the smooth search, optimal element reduction is applied for DOA estimation of the desired users by modifying the classical MUSIC algorithm. The novelty of the S2 MUSIC consists of reducing the search to a limited range instead of searching the entire space. S2-MUSIC offers a significant reduction on the computation time without a significant impact on the accuracy on the DOA estimates.

Description of Switched Beam Smart Antenna

One of the conventional smart antenna systems built for wireless applications is the switched beam array. A specific beam pattern is formed such that the main beam is directed towards the user signal. Gain is increased in the direction of the desired user and the co-channel signals that are in different directions are greatly suppressed. The switched beam array creates a group of overlapping beams that together result in omni-directional coverage. In general an M-element array may generate an arbitrary number of beam patterns. It is however much simpler to form qM beam patterns, where q=1, 2,…,Q with the rule of thumb that $360°/QM \geq 1/10$ of the half-power beamwidth. The beam pattern is generated using specific weights applied to the array elements. In our system, M-beams are generated for M-element array.

After identifying the received signals as signals of desired users, they are averaged over several sets of consecutive phase delays, and the directions corresponding to the beams with the largest outcome (above a preset threshold) are selected as the DOA estimates. For an M-element circular array, the entire space is split into M sectors each with one element located in the center, as shown in Figure 8. Before the operation, an M

set of the spatial signatures of the fixed beams are predetermined and saved in the system, making the operation computationally efficient.

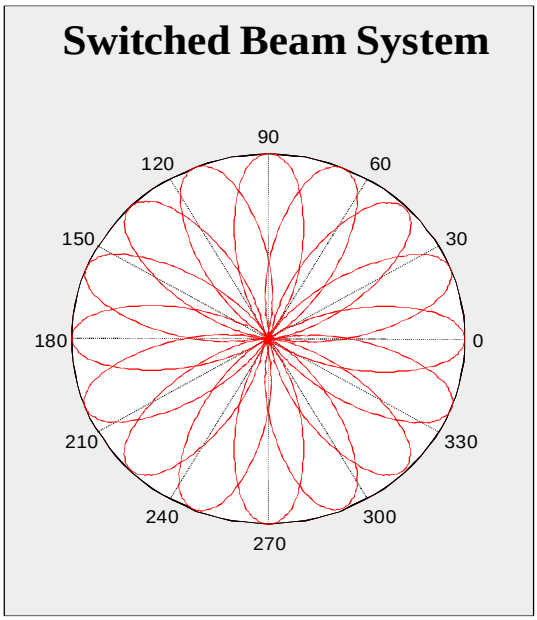

Figure 8 Switched beam system showing a multitude of overlapping beams enabling an omni-directional coverage

The saved weight coefficients can be generated with co-phasal excitation or by using window functions. In the co-phasal case, a weight vector can be defined and kept in the smart antenna system memory based on the spatial signature received. Weights are applied over a sequence of time (each set of weights is generated at a particular time) to cover the overall field of view. The i^{th} time slot such that the weight coefficient vector will match the spatial signature vector. Each beam T has a specified spatial signature,

$$\vec{a}_{\mathrm{t}}(\varphi) = [\vec{a}(\varphi)_1, \vec{a}(\varphi)_2, \dots, \vec{a}(\varphi)_{\mathrm{T}}]^{\mathrm{H}} \qquad \text{Eq 40}$$

The switched beam array output vector is

$$\vec{x}(t) = [\vec{a}(\varphi)_1, \vec{a}(\varphi)_2, \dots, \vec{a}(\varphi)_{\mathrm{T}}]^{\mathrm{H}} \vec{s}(t) \qquad \text{Eq 41}$$

Assuming only one source, when an $\vec{a}_t(\varphi)$ is equal or very close to the signal spatial signature $\vec{a}_k(\varphi)$ with k being the number of incident signals, the t^{th} element in the output vector will be equal or very close to the signal strength received

$$\vec{s}(t) = [0, \dots, \sqrt{P_t}, \dots, 0]^T \quad \text{Eq 42}$$

Thus, the desired user is in the region of the t^{th} beam. If there is more than one desired user, a predefined threshold for the system can be set, once the received power at one beam passes the threshold, it will be assumed that a desired user is located in that beam range exists.

To reduce the side lobes of beam patterns, the channel signals are shaped by a windowing function such as Chebyshev, Hamming, Hanning, Cosine, or triangular, among others. This is the simplest way to beamform to maximize the signal to interference ratio of a switched beam array without using adaptive beamforming. By carefully controlling the side lobes in the non-adaptive windowed array, most interference can be reduced to achieve a significant increase in the signal to interference ratio.

S2 MUSIC Implementation Method

The method is implemented as follows. When the system is powered up, the array will be in the receiving mode and it will directionally receive from beam 1 to beam M. The beam t^{th} with the maximum received power will be selected. Once the sector of arrival is determined, the number of elements used to compute the data covariance matrix is reduced, and we name the new number of elements chosen m_{s2}, such that $m_{s2} \leq M$.

An inherent reduction in the received signal covariance matrix is achieved. In addition, the steering vector size used to compute the spatial pseudo-spectrum is also reduced. Figure 9 shows that once the desired user is detected using the switched beam system, the sector of arrival is determined and only a portion of the elements are used to construct the received data vector. One should note that the electric size of the array is dependent on the number of elements used and has to be taken into account. For the 8 element UCA, the following equation governs the array electric size as a function of the number of elements used, $\beta\rho = 0.3812 \times m, (m = 1, \dots, M)$.

In summary the following steps are taken to implement S2-MUSIC:

- A switched beam system is used for rough search the location of the desired user(s).
- Certain number of the array elements are selected for the received data vector
- A reduced covariance matrix is constructed
- A reduced steering vector is used for the computation of the spatial pseudo-spectrum.

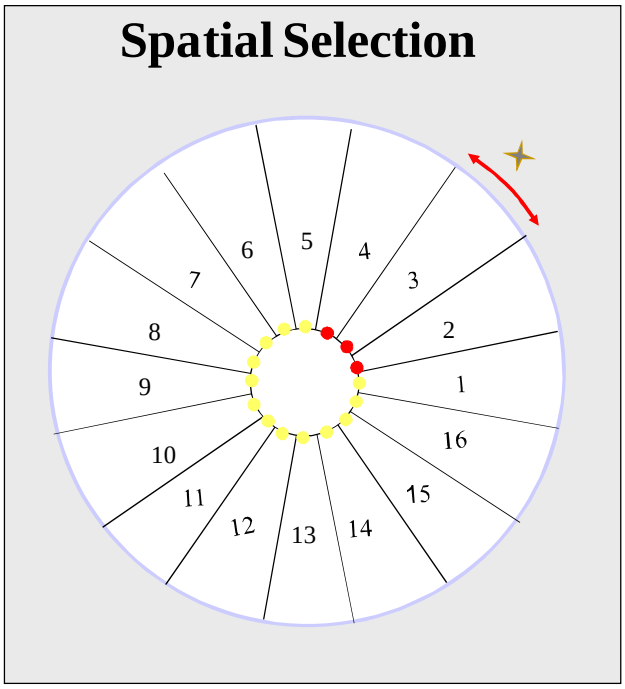

Figure 9 Spatial section based on determining the sector of arrival first and then using a reduced element (shown in red) to obtain the received signal data vector

CHAPTER FOUR

DIRECTION OF ARRIVAL ESTIMATION SIMULATION STUDY RESULTS

The first attempt to comprehensively achieve a comparative study of spectral direction of arrival estimation algorithms was carried out in 1984 and revised in the summer of 1998 in [43]. The study considered five algorithms described in Chapter three, namely, AAR, BSA, MEM, MLM, TNA and MUSIC. The means of comparison used were bias, sensitivity, and resolution. The report defined a super-high resolution algorithm as one that is able to resolve emitters that are 0.1 beamwidth apart. It was deduced that super-high resolution is possible to achieve in theory but in practice high SNR will be a highly important system characteristic. Data examination revealed that for limited observations (~10 samples), it is difficult to achieve high resolution, but if the number of observations is increased by an order of magnitude one sees significant improvements, particularly with MUSIC. In fact, MUSIC was determined to be asymptotically more sensitive to SNR than other spectral algorithms, and it tends to approach the Cramer-Rao bound as SNR or samples are large enough, which suggests that MUSIC is asymptotically efficient.

In spite of its relatively poor sensitivity MUSIC is generally superior in terms of producing more accurate estimates than any other spectral algorithms assuming a large enough SNR. In other words, MUSIC was found to be a little more sensitive but has smaller bias and lower false peaks rate. With the use of root finding algorithms [44] an improvement in sensitivity was deduced especially at low sampling.

In this chapter, various spectral based algorithms have been considered. Bartlett and Capon being the conventional ones and MUSIC, beamspace MUSIC and S2-MUSIC as the high resolution algorithms. All these algorithms have been compared in terms of accuracy, resolution, and computational complexity. The algorithms were rated according to how much bias they exhibit under perfect conditions, their resolution under perfect conditions and how robust they are when subject to magnitude error, phase error, low SNR, and mutual coupling. In beamspace, the number of modes was also varied while in S2 MUSIC the number of elements was varied. In most simulations, the number of modes used was 3 (corresponding to 7 beams) and for most simulations involving S2 MUSIC, 5 elements were usually used.

Unless stated otherwise, each of the results consists of an average over 200 runs. A 5.8 GHz sinwave was used as a source and 1000 samples were taken. The simulations investigate an 8 element UCA with 3.05 electric radius. The elevation angle was set to 90 degrees. The field of view was split into 3600 sectors. White Gaussian additive noise was used to simulate a noisy environment. The base algorithms code along with an example of the simulations and processing are shown in Appendix C. The Root Mean Square Error (RMSE) was used as a measure of the error in the simulations.

DOA Estimation Accuracy

The first step in the simulation study consisted of investigating how the DOA estimation accuracy of the algorithms was affected when the SNR and number of elements in the array are varied. Results for a varying SNR are depicted in Figure 10

where the RMSE was computed while varying the SNR from 0 to 20 dB in 2 dB increments. It is observed that at low SNR the subspace based methods exhibit a larger error compared to the conventional methods (Bartlett and Capon), but as the SNR becomes large enough the RMSE tends to zero making MUSIC, beamspace and S2 MUSIC consistent since their RMSE tends to zero when the number of samples is large enough and the SNR level is high enough.

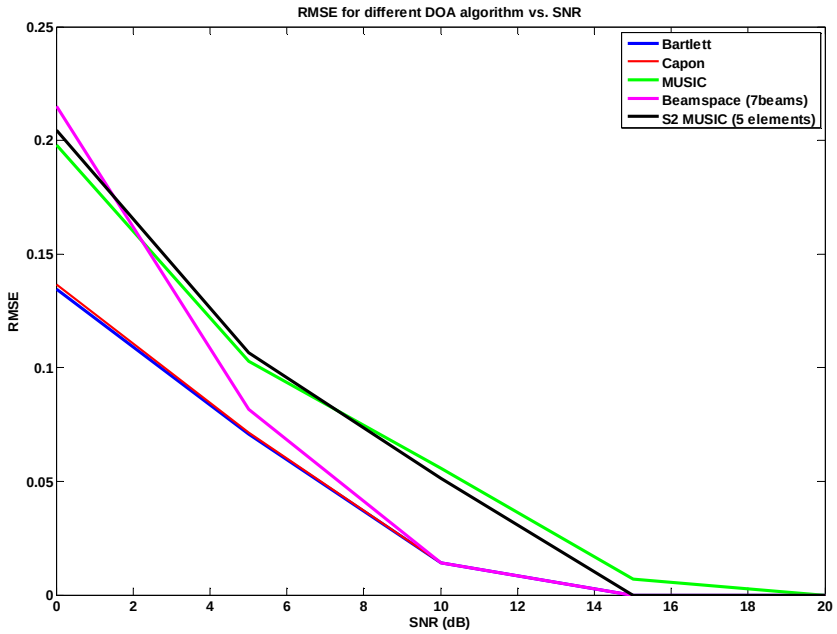

Figure 10 RMSE for different algorithms vs. SNR

In Figure 11 the relationship between the RMSE and SNR is depicted for different numbers of elements used for S2 MUSIC. It is clear that as the number of elements decreases the error becomes more pronounced. Reducing the size of the covariance matrix is analogous to reducing the size of the noise subspace which leads to an increase in the RMSE.

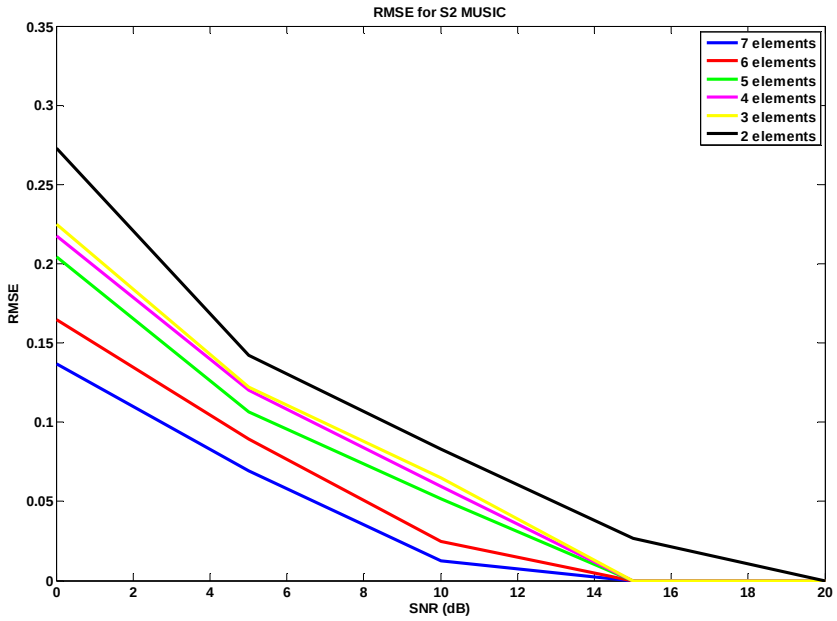

Figure 11 RMSE vs. SNR for S2- MUSIC for a varying number of elements

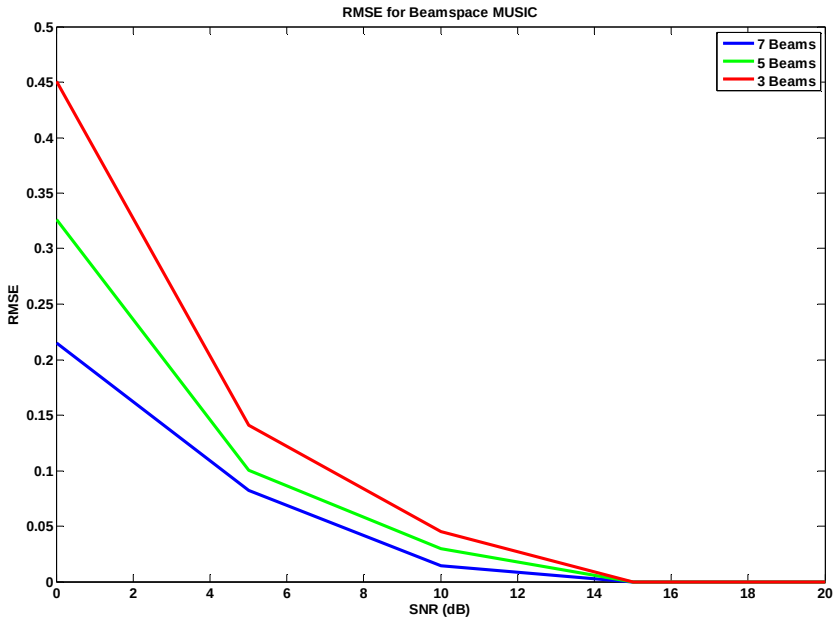

Figure 12 RMSE vs. SNR for beamspace MUSIC for a varying number of beams

In the case of beamspace MUSIC, the number of beams used to pre-multiply the received data vector was varied. The results are illustrated in Figure 12 and show that the

RMSE increases as fewer beams are used. The use of fewer beams is analogous to a reduced size covariance matrix leading to a noise subspace with a lower dimension causing the RMSE increase.

The second set of simulations consisted of investigating the effect of the array element spacing on algorithm accuracy. The SNR was fixed to 10 dB while 5 elements were used in the S2 MUSIC and 7 beams were used in the beamspace MUSIC. The inter-element spacing was varied from 0.1 λ to 1.5 λ in 0.1 λ increments.

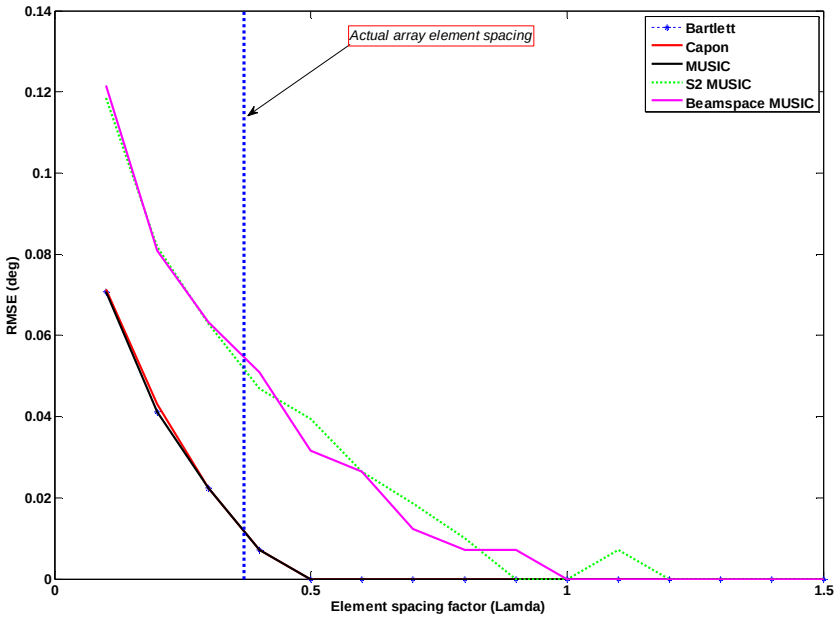

Figure 13 RMSE for varying element spacing in the UCA

The results are depicted in Figure 13, showing that at 0.5 λ spacing and above the RMSE for Bartlett, Capon, and MUSIC tends to zero while for S2 MUSIC and beamspace MUSIC, the RMSE tends to go to zero around 1λ. The actual array inter-element spacing in UCA designed by our group is 0.375λ which is not optimal for DOA estimation according to these simulation results. One should keep in mind that the UCA

was designed specifically to optimize the elevation and azimuthal beam shapes of the beams formed. These results suggest that for future array design, both beamforming and DOA estimation should be considered to find the right spacing to optimize the beam shape while minimizing the RMSE for the desired algorithm.

Another important parameter to consider is the number of samples of the impinging signals. This effect was examined in a series of simulations where the SNR was fixed to 10 dB. The performance of the algorithm accuracy was studied by varying the number of samples from 10, 20, 50, 100, 200, 500, 1000, to 5000.

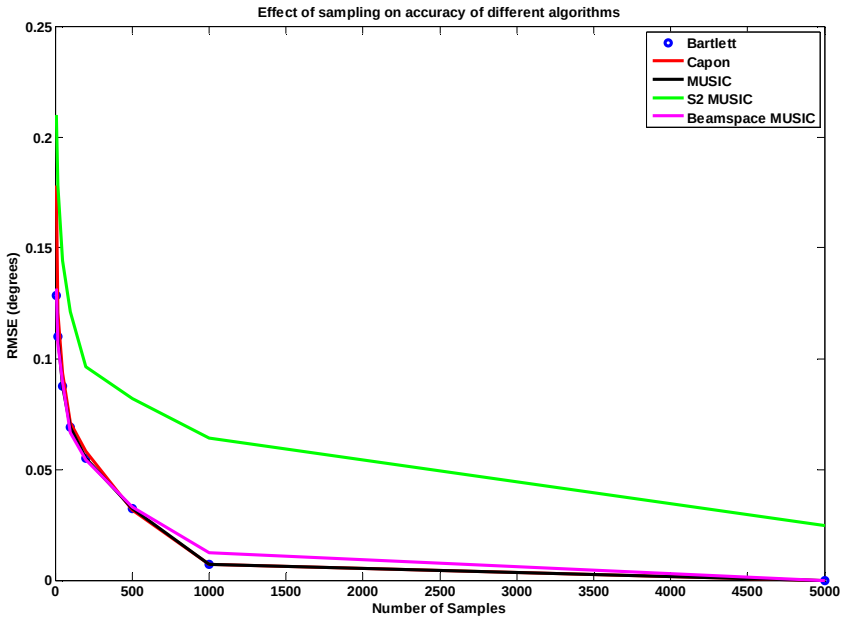

Figure 14 RMSE for different algorithms for a varying number of samples

Figure 14 depicts the results for the considered algorithms, where 5 elements were used in S2 MUSIC and 7 beams were used in the case of beamspace MUSIC. The results indicate that as the number of samples increase, the RMSE tends to zero. S2 MUSIC

seems to result in more error but the increase is not sufficiently significant to cause a dramatic error in the DOA estimates.

The number of elements used in the UCA was also investigated, where the number of elements was varied from 2 to 10. The electrical radius was varied accordingly ($\beta\rho = 0.380 \times M$). At least two elements have to be used in the case where only one signal source is present, and at least three elements have to be used when two sources are present. This limitation arises from the fact that in the subspace methods the signal covariance correlation matrix has to be singular or rank deficient, which is imperative to obtaining a signal and noise subspace.

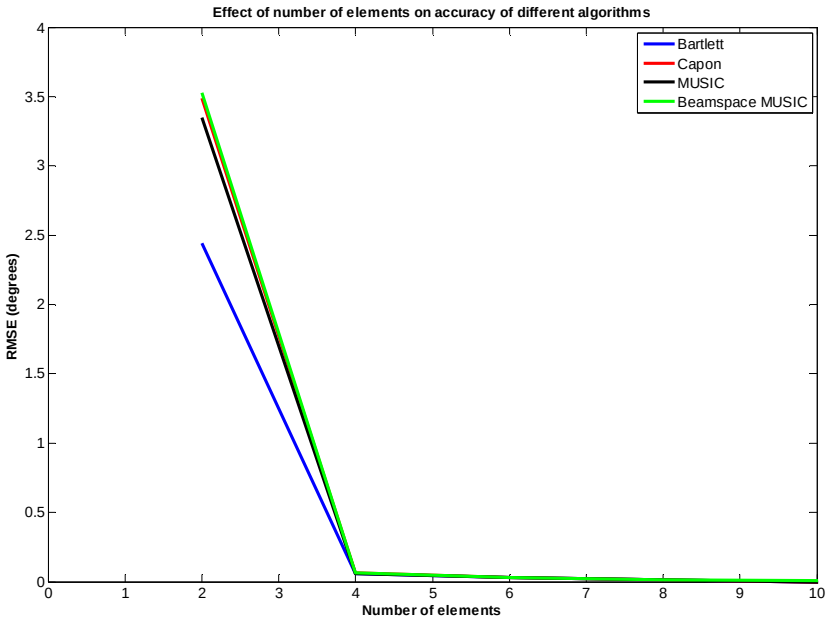

Figure 15 RMSE for different algorithms as the number of elements in the UCA is varied

As depicted in Figure 15, the RMSE becomes significant when the number of elements is decreased, which is similar to deceasing the dimension of the noise subspace. This observation is critical as it points out that the accuracy of S2 MUSIC will inherently

be affected, since the latter is based on a reduced number of elements, which also applies to beamspace MUSIC. However when 4 or more elements are used, the RMSE is not significant.

The most important parameter that affects algorithms accuracy is mutual coupling. To simulate the effect of mutual coupling, an 8-by-8 mutual coupling matrix was constructed and used to pre-multiply the received signal data vector. The diagonal of the mutual coupling matrix was set to unity while that first off diagonal elements where varied from -30 to -5 dB, the higher order diagonal elements were set to zero. This simulation considered mutual coupling as it affects adjacent elements only, the simulation can easily be extended to include the effects of mutual coupling to all elements by populating the high order diagonal elements of the mutual coupling matrix. The SNR for this investigation was set to 20 dB.

The results depicted in Figure 16 show that as the coupling between adjacent elements increases the RMSE becomes more pronounced. S2 MUSIC seemed to be more susceptible to mutual coupling than the other algorithms, followed by beamspace MUSIC, which showed a slightly higher RMSE then the rest of the algorithms.

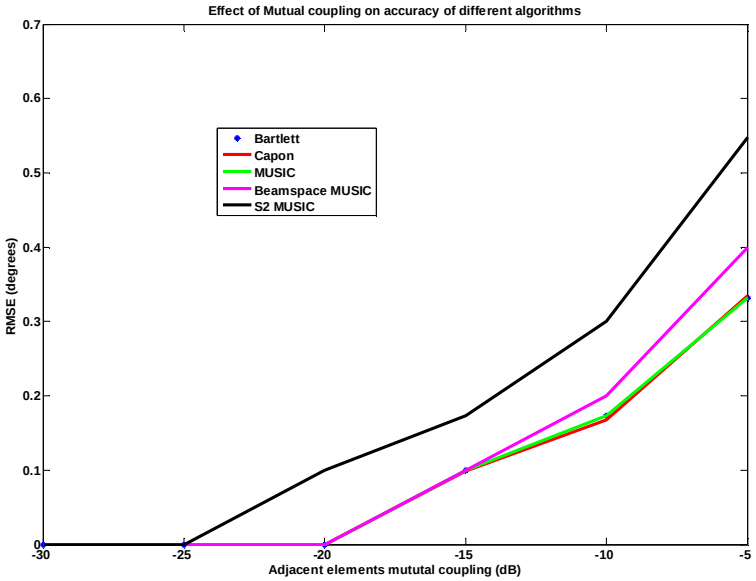

Figure 16 RMSE of different algorithms for varying mutual coupling

Phase and Magnitude Error Effect on Accuracy

The accuracy of the algorithms was examined as phase and amplitude errors were introduced. The "rand" function in Matlab was used to simulate the phase and magnitude errors. The function generates pseudo-random values drawn from a uniform distribution on the unit interval. The SNR was set to 20dB and 1000 samples were used for the 8 element UCA. The phase error was varied from 5 degrees to 60 degrees in 5 degree steps. The amplitude error was introduced as a percentage of the actual amplitude and was varied from 5% to 50% in 5% increments. The RMSE was computed over 20 runs for each phase and magnitude error.

Figure 17 depicts the RMSE vs. phase error showing a steady increase in RMSE as the phase error increases. Results for S2 MUSIC showed a slightly higher RMSE

compared to the other algorithms. Figure 18 shows the amplitude error, where capon and beamspace MUSIC were the only algorithms where the amplitude RMSE was observed.

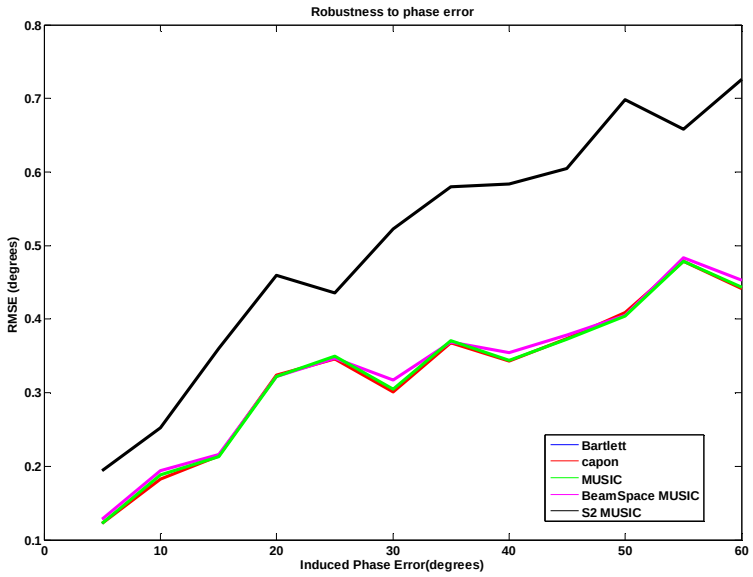

Figure 17 RMSE for different algorithms for a varying induced phase error

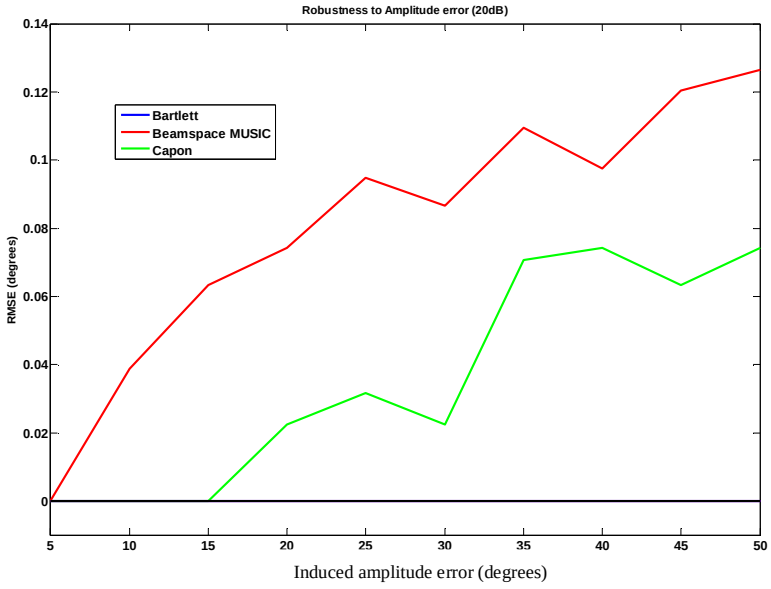

Figure 18 RMSE for different algorithms for a varying induced amplitude error

Resolution

To investigate how various parameters in the system affect the resolution of algorithms, two sources (sinwaves) set 10 MHz apart were used in the simulation. One of the sources was fixed at 180 degrees while the other was swept over the entire azimuth range in 1 degree increments. The number of samples used was 1000 and azimuth range was divided into 360 sectors. The results here are based on a single run; Monte Carlo simulations should be carried out in the future to further validate the results. For S2 MUSIC, 5 elements were used and 7 beams were used in beamspace MUSIC. The first parameter considered was SNR, where it was varied from 20 dB to 0 dB in 5 dB increments.

Two types of plots are used to better visualize the results. The first is a histogram of the bearings detected, with the y axis representing the fixed source while the x axis represents the actual detected bearing, which corresponds to the peak that has the highest power in the spectrum or the spatial pseudo-spectrum. The second plot, which is based on the same results, is a power color map that enables one to visualize the power levels for each of the signal sources detected over the entire azimuth range.

Only 20 dB SNR and 0 dB SNR results are shown, the rest of the results for SNR 15 dB, 10 dB, and 5 dB are included in Appendix D. Figure 19 depicts the histogram of the results for 20dB and Figure 20 depicts the results for 0 dB. In the case where the SNR is 20 dB, except Bartlett, all the algorithms seemed to have superb resolution at high SNR. A closer look at the data revealed that Bartlett cannot resolve signals that are less

than 40 degree apart, while the Capon results show that it can resolve signals that are spatially separated by more than 4 degrees.

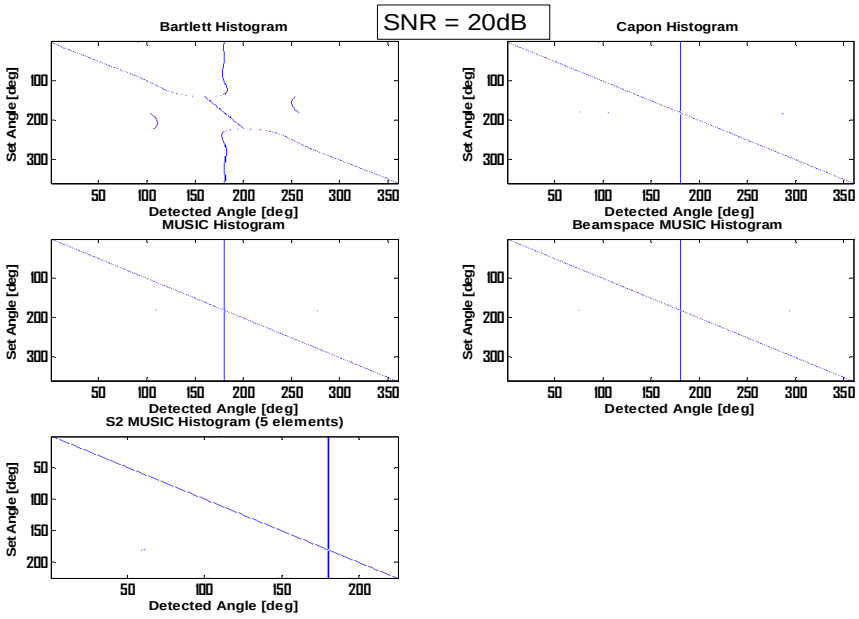

Figure 19 Various algorithms histogram for an SNR of 20 dB

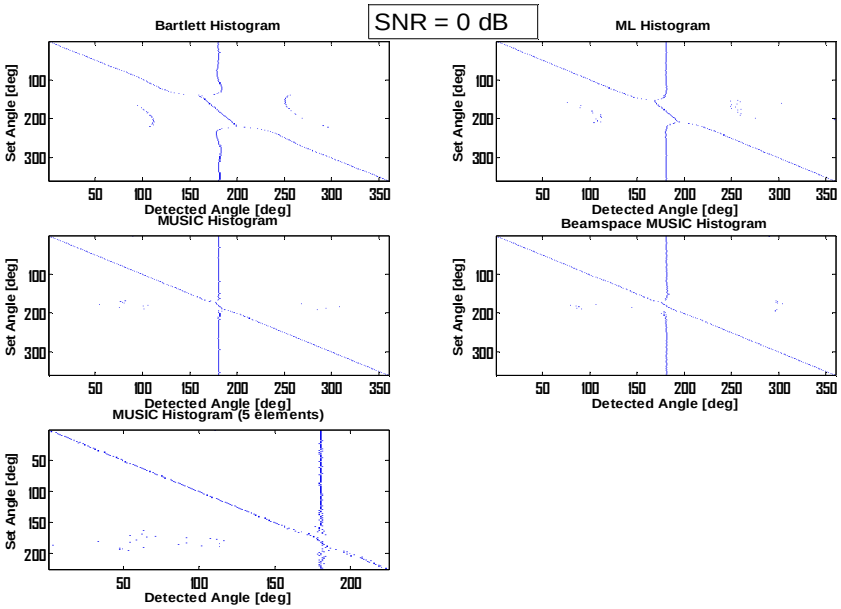

Figure 20 Various algorithms histogram for an SNR of 0 dB

MUSIC, S2 MUSIC, and beamspace MUSIC all showed the ability to resolve the two sources to within a degree at high SNR. At 0dB SNR, the ability to resolve spatially close sources was dramatically affected. Bartlett could not resolve signals that were less than 70 degrees apart and the deviation from the true peak reached a maximum of 2 degrees. Capon was unable to distinguish sources less than 54 degrees apart with a maximum deviation from the true angle of 3 degrees. MUSIC exhibited the best behavior with the ability to resolve to within 19 degrees and 2 degrees of maximum deviation. Beamspace MUSIC failed to resolve signals within 27 degrees of spatial separation with a maximum deviation of 3 degrees. S2 MUSIC achieved the same resolution as MUSIC (20 degrees) but showed a maximum deviation error of 8 degrees.

In Figure 21 (SNR 20 dB) and Figure 22 (SNR 0 dB), the power of the spectrum for each run over the entire field of view is plotted with a power color map. At 20 dB SNR, the detected power spectrums obtained by using Bartlett revealed that the peaks tend to merge at a faster rate compared to the other algorithms; the color map reveals that the level of the sidelobes is very high. The other algorithms showed a good peak separation along with a large peak to floor ratio, particularly for the high resolution algorithms. Compared to the 20 dB SNR case, the 0 dB SNR case showed that as the SNR decreases, the floor rises making the peak to floor ratio lower, affecting the resolution performance. The histogram of S2 MUSIC is depicted in Figure 23.

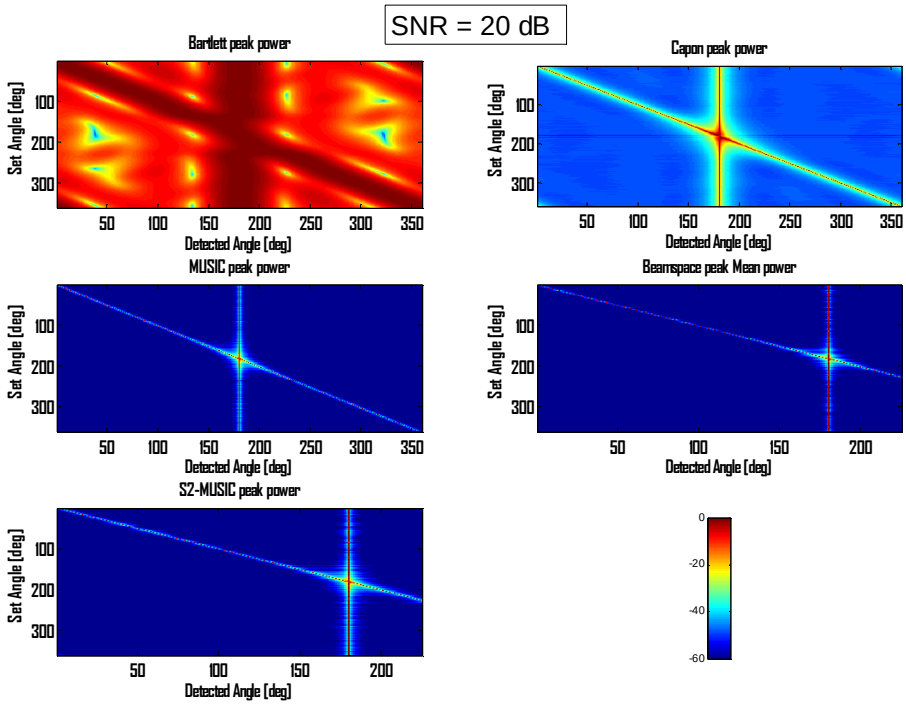

Figure 21 Power color map plot for various algorithms with a set SNR of 20 dB

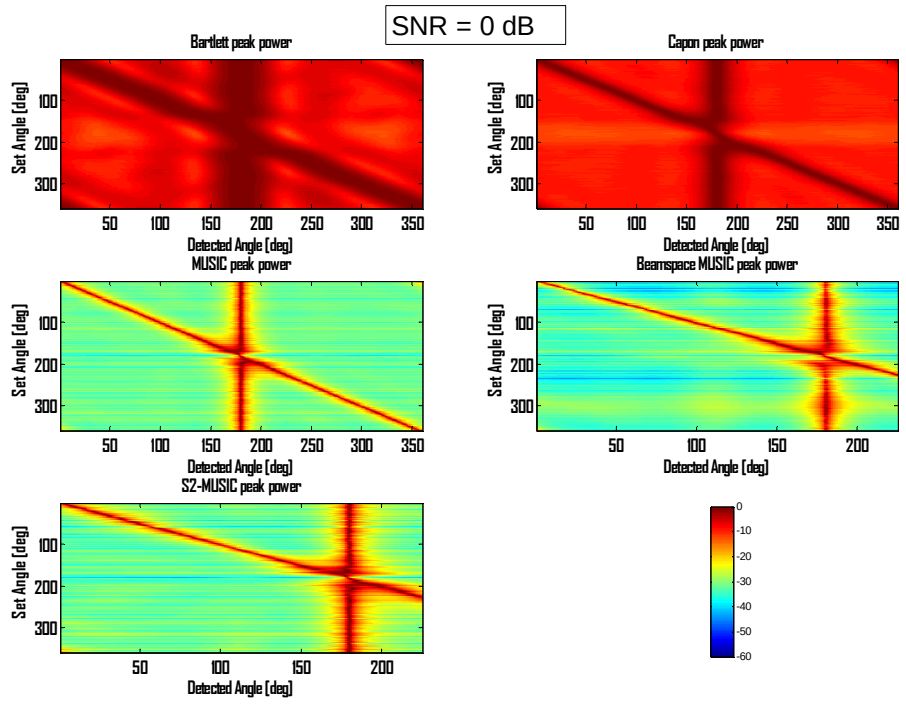

Figure 22 Power color map plot for various algorithms with a set SNR of 20 dB

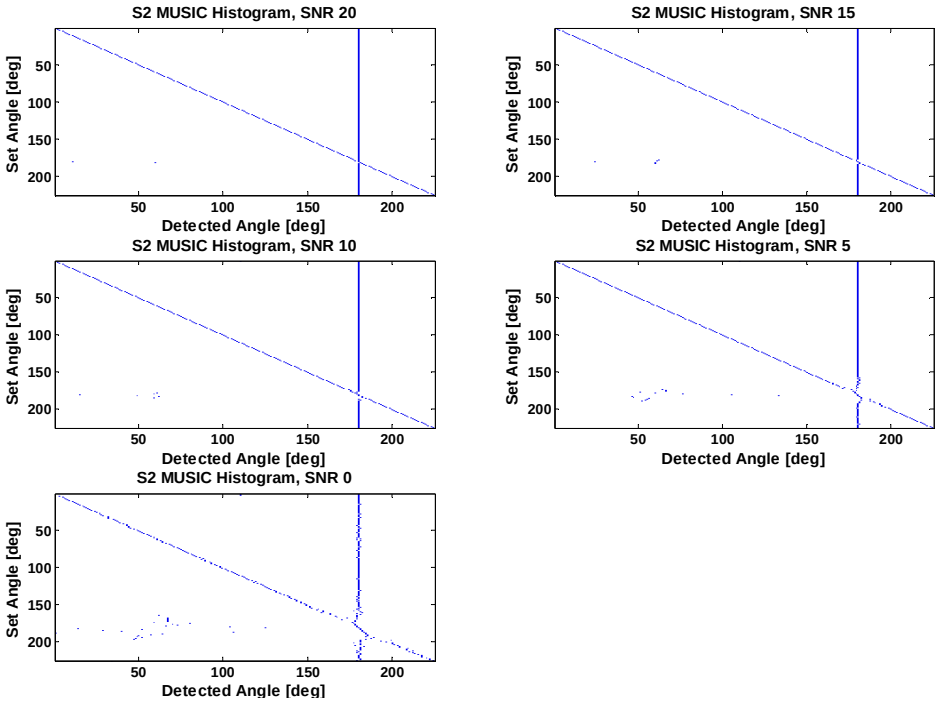

Figure 23 Histogram for S2 MUSIC for varying SNR

Figure 23 shows how S2 MUSIC is affected by varying the SNR for a fixed number of elements (5 elements). Above 10 dB SNR, the algorithm behaves well in terms of resolution and accuracy, but below 10 dB SNR the ability to resolve closely spaced sources is diminished along with noticeable degradation in accuracy.

The next step consisted of investigating how the number of samples used affects the resolution of the algorithms. In this case, the SNR was fixed at 20 dB, 5 elements were used for S2 MUSIC and 7 beams were used for beamspace MUSIC. The number of samples were 10, 100, and 1000. The results in a histogram format that show the set angle vs. the detected angle are depicted in Figure 24, Figure 25, and Figure 26, respectively. Comparing 10 sample and 100 sample results, it is clear that a low sample number tends to degrade the resolution capability of all the algorithms. Capon in

particular resulted in more false peaks than any other algorithm. The results obtained when 1000 samples were used are comparable to when 100 samples were used.

The number of adjacent elements in the array was also varied to examine its effect on resolution. The SNR was set to 10 dB, 1000 samples were used and 7 beams were used for beamspace MUSIC. The results when the number of elements used was 4, 6, and 10 are presented in Figure 27, Figure 28, and Figure 29, respectively. It is clear that as the number of elements increases, the resolution is improved. Bartlett showed the largest effect since its resolution is directly dependent on the number of elements used. Capon resulted in a better resolution than Bartlett and was more affected by the decrease in the number of elements than the high resolution algorithms.

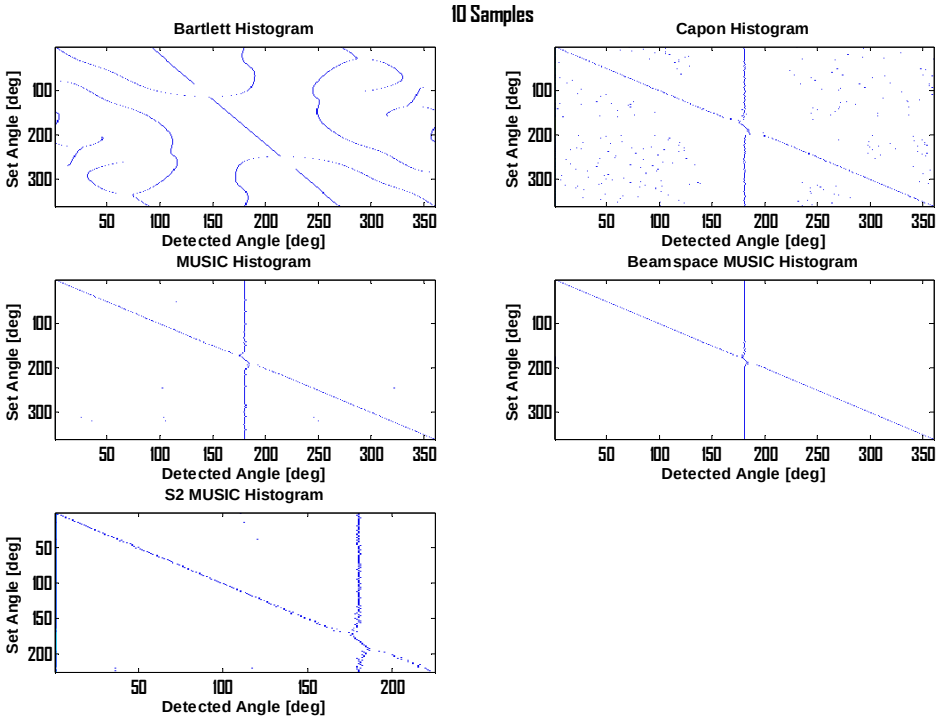

Figure 24 Histogram for various algorithms for a received data vector sampled 10 times

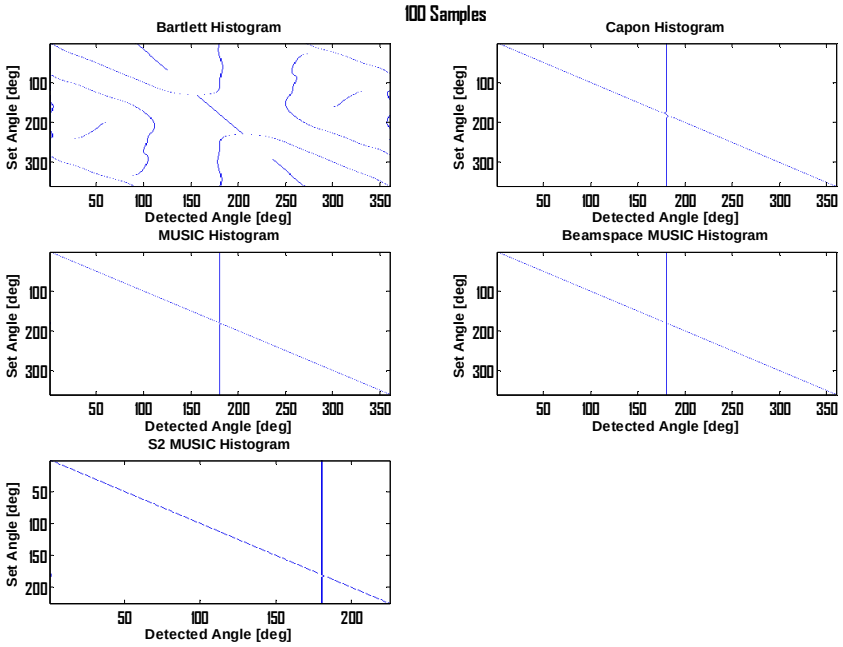

Figure 25 Histogram for various algorithms for a received data vector sampled 100 times

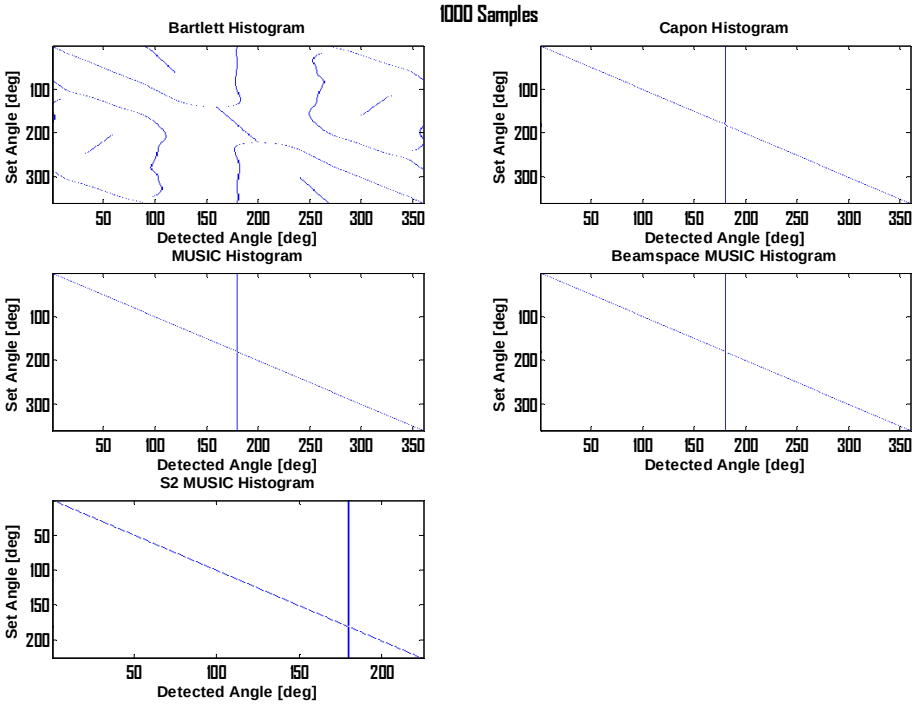

Figure 26 Histogram for various algorithms for a received data vector sampled 1000 times

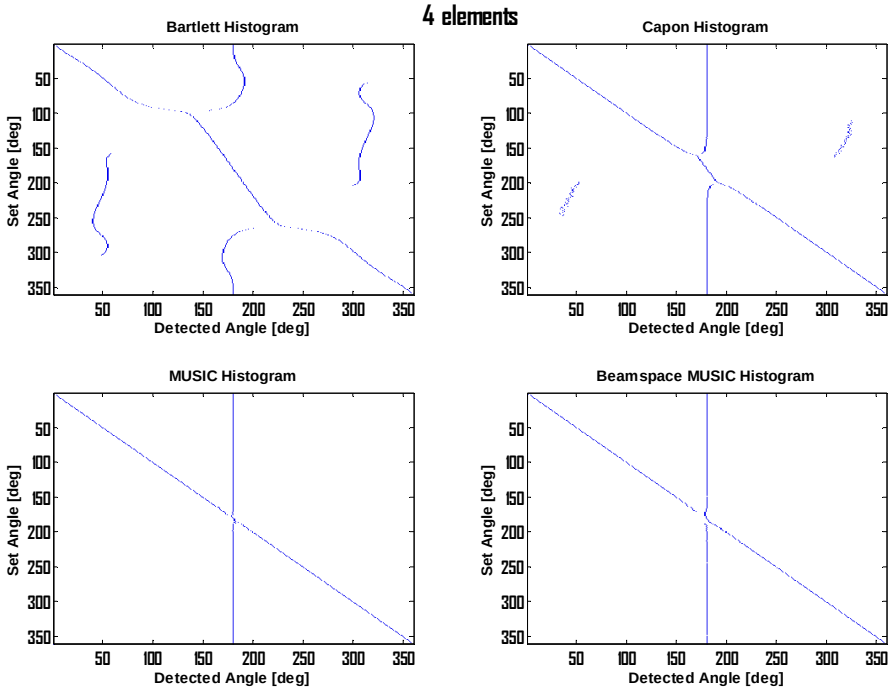

Figure 27 Histogram for various algorithms when a 4 element UCA is used

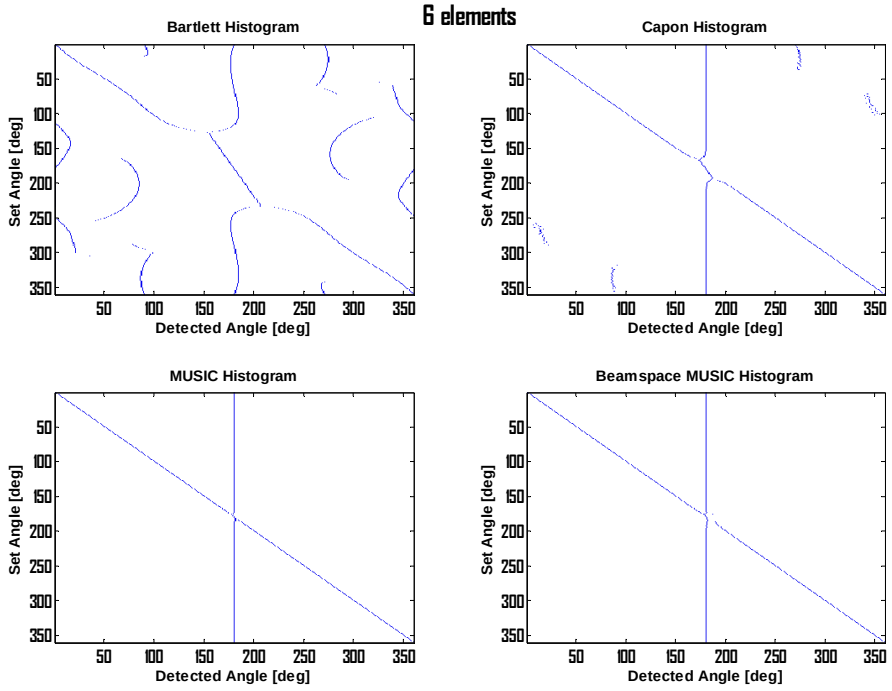

Figure 28 Histogram for various algorithms when a 6 element UCA is used

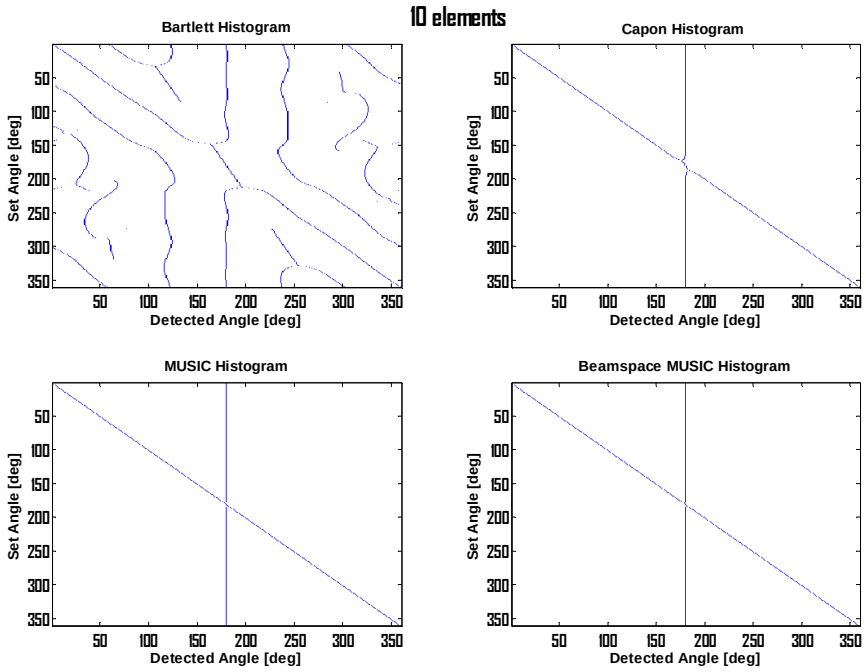

Figure 29 Histogram for various algorithms when a 10 element UCA is used

Robustness Towards Phase and Magnitude Error

In this section the resilience of the algorithms when subjected to phase and magnitude error is examined. Figure 30, Figure 32, and Figure 34 represent the histogram results for the set angle vs. the detected angle when the induced angle error was set to 5 degrees, 20 degrees, and 40 degrees, respectively. The power color map plots are shown in Figure 31, Figure 33, and Figure 35 for the same simulation conditions. The results indicate that at as the phase error is increased, resolution capability is reduced and the floor rises significantly. In addition, the accuracy is affected and the algorithms' error increased significantly with an increased phase error. S2 MUSIC was affected the most compared to the other high resolution algorithms because less elements were used.

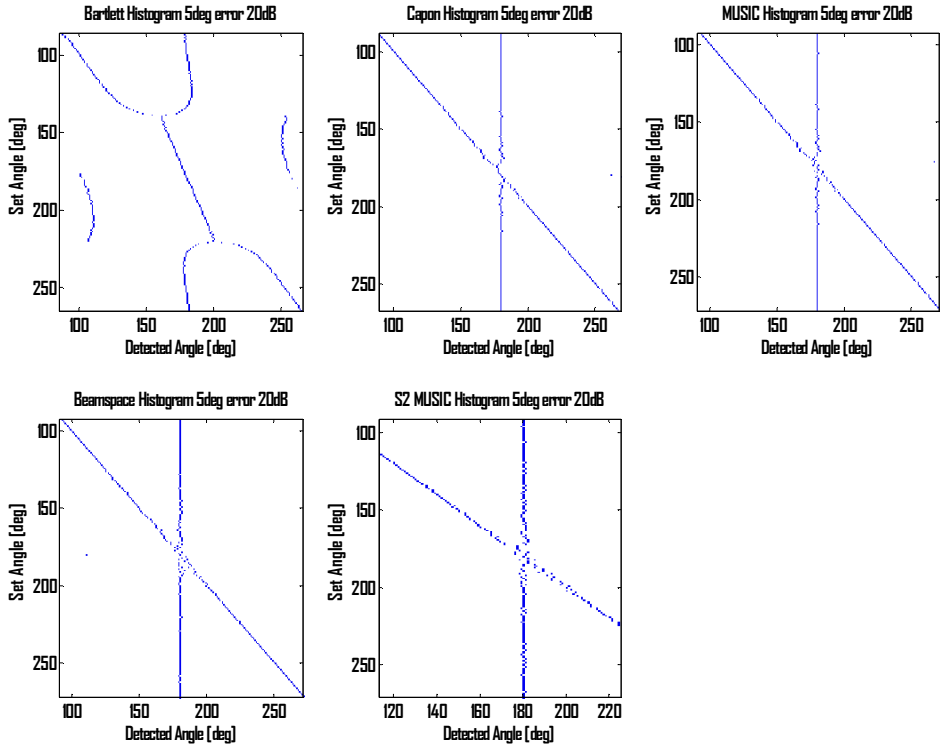

Figure 30 Histogram for various algorithms when a 5 degree phase error is induced

Figure 36, Figure 38, and Figure 40, respectively, show the histogram results when 5%, 20% and 40% amplitude error is introduced. Figure 37, Figure 39, and Figure 41show the power color map when the amplitude error was varied from 5%, 20%, to 40% respectively. The results indicate that the resolution of the algorithms along with the peak-to-floor ratio deteriorate as the amplitude error is increased, and S2 MUSIC seemed the least resilient to amplitude error.

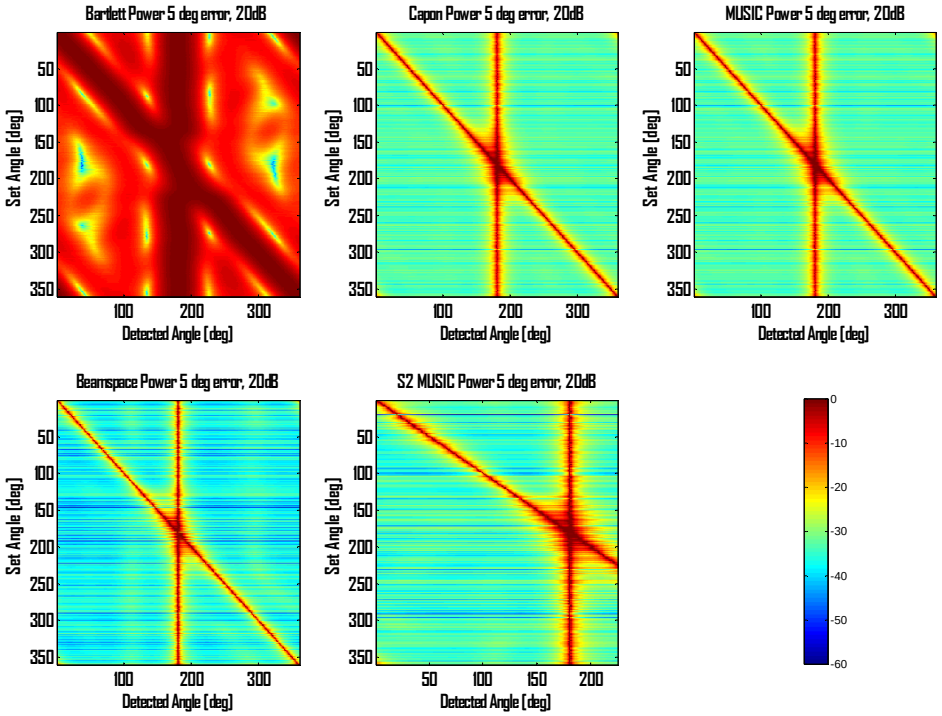

Figure 31 Spectrum power plot for various algorithms when a 5 degree phase error is induced

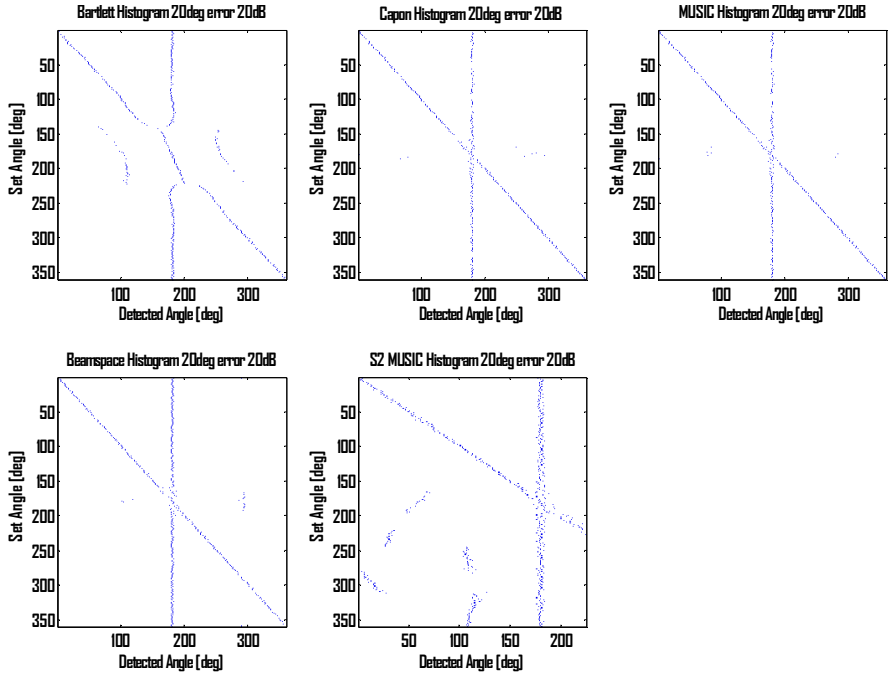

Figure 32 Histogram for various algorithms when a 20 degree phase error is induced

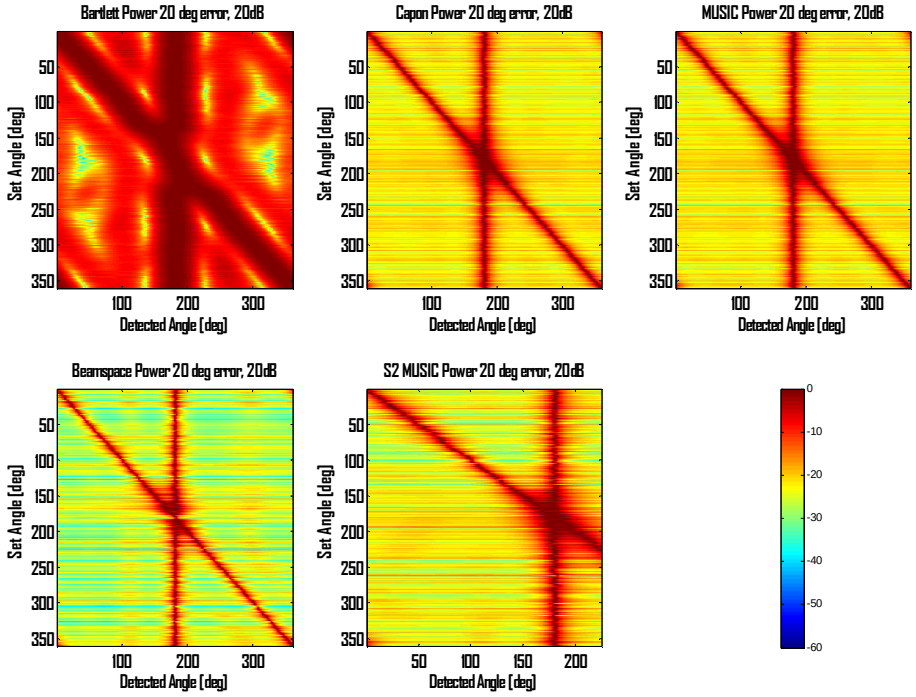

Figure 33 Spectrum power plot for various algorithms when a 20 degree phase error is induced

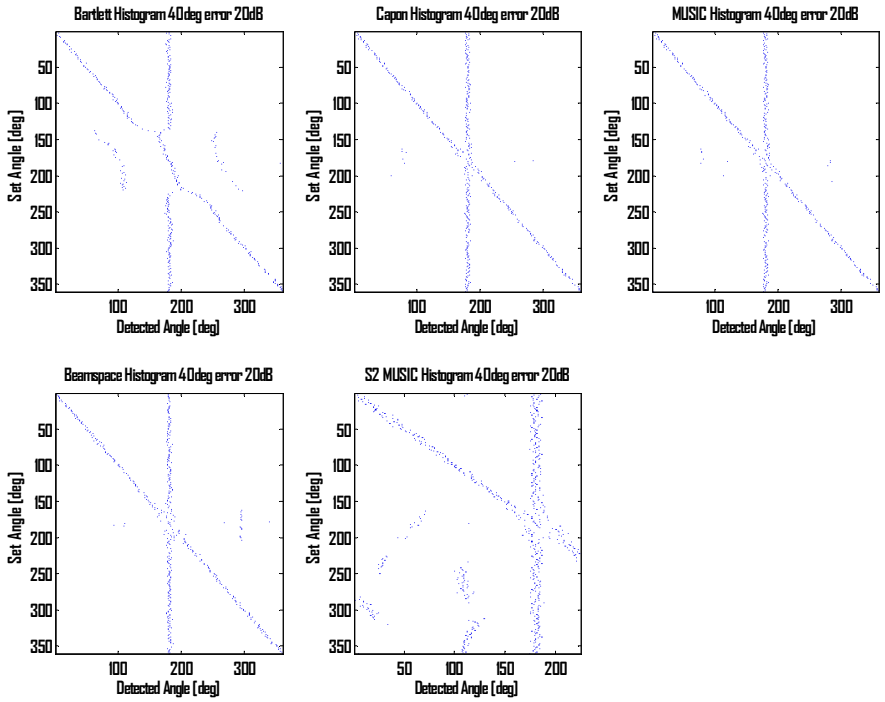

Figure 34 Histogram for various algorithms when a 40 degree phase error is induced

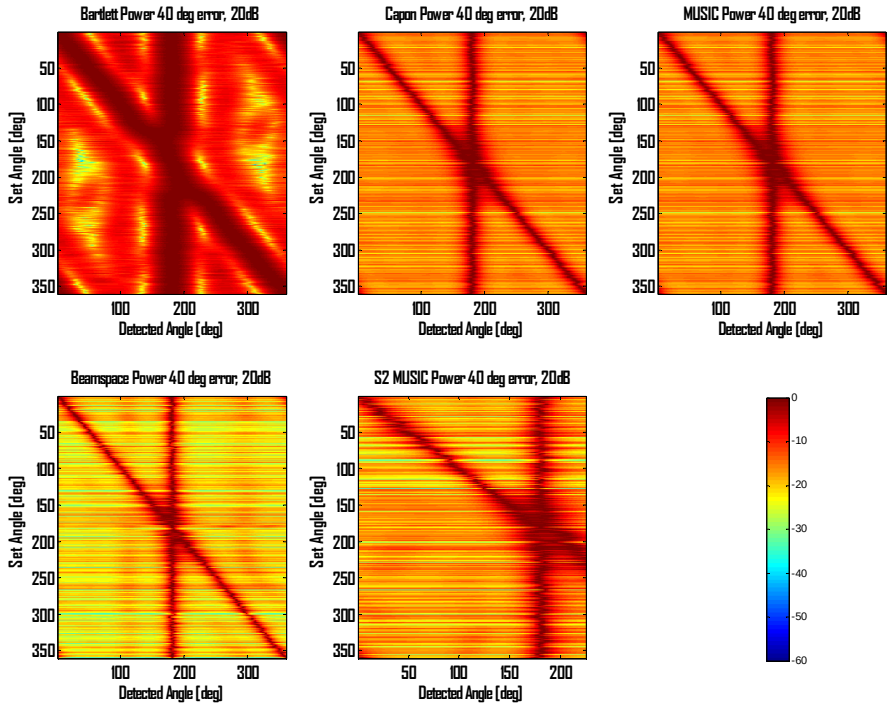

Figure 35 Spectrum power plot for various algorithms when a 40 degree phase error is induced

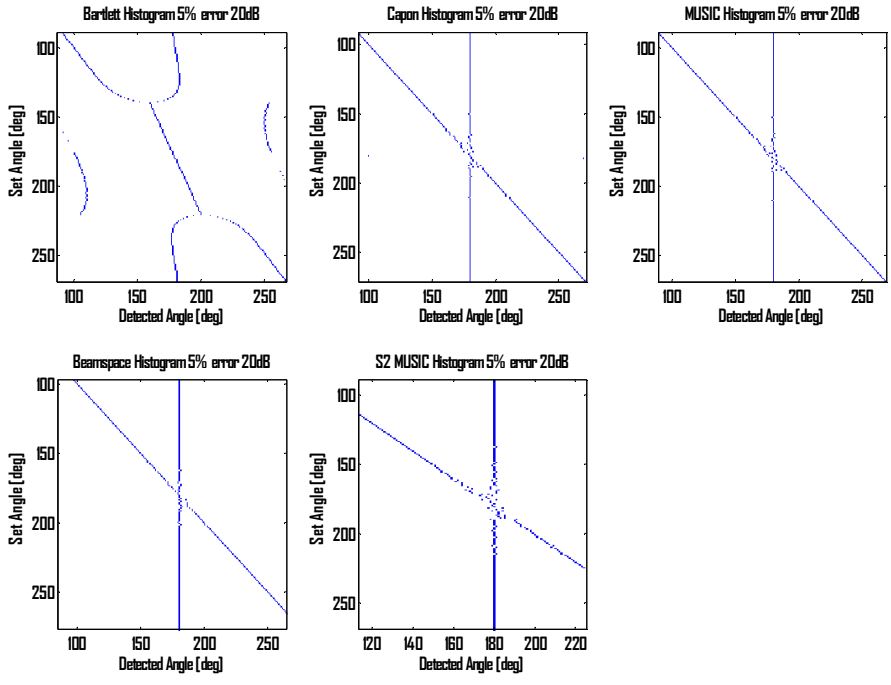

Figure 36 Histogram for various algorithms when a 5% amplitude error is induced

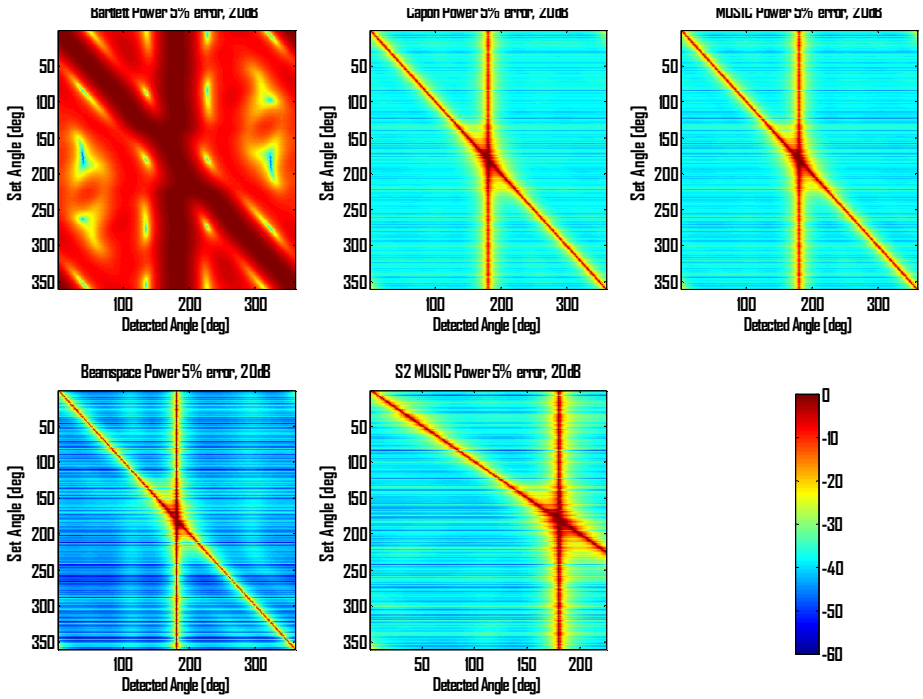

Figure 37 Spectrum power plot for various algorithms when a 5% amplitude error is induced

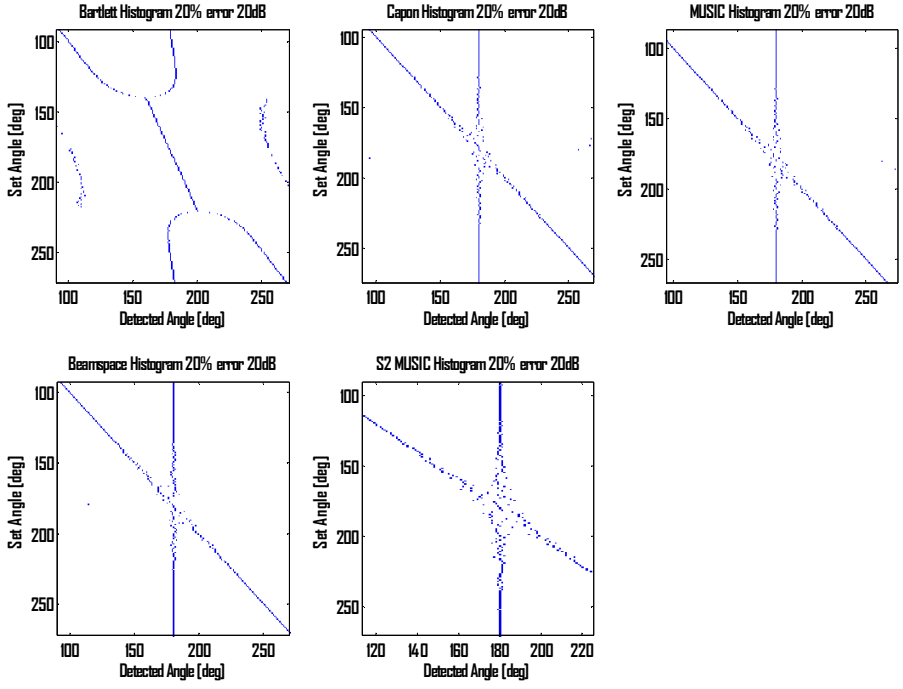

Figure 38 Histogram for various algorithms when a 20% amplitude error is induced

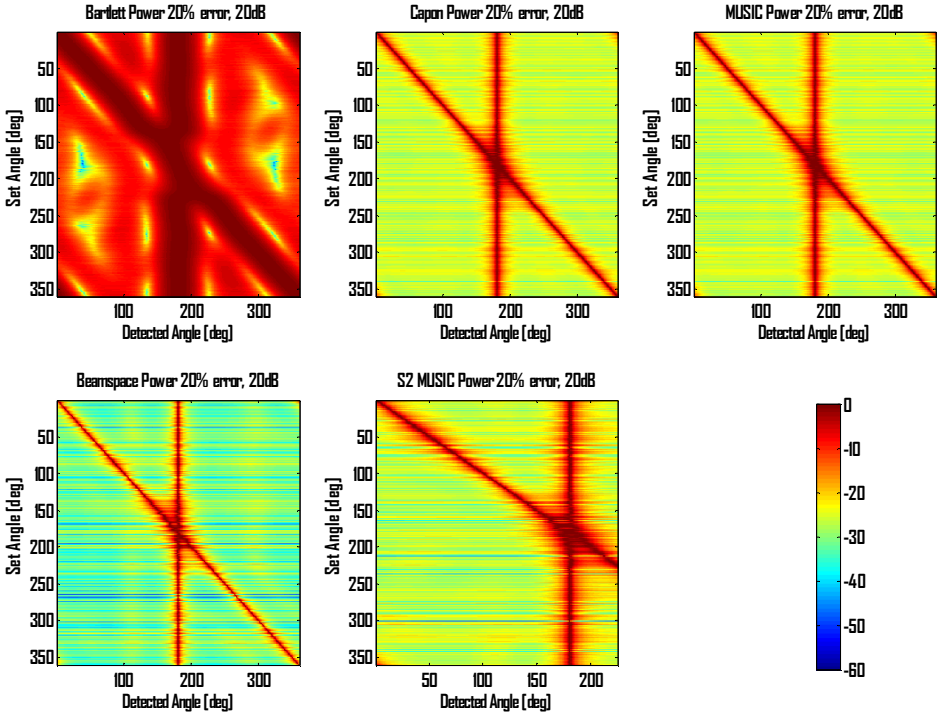

Figure 39 Spectrum power plot for various algorithms when a 20% amplitude error is induced

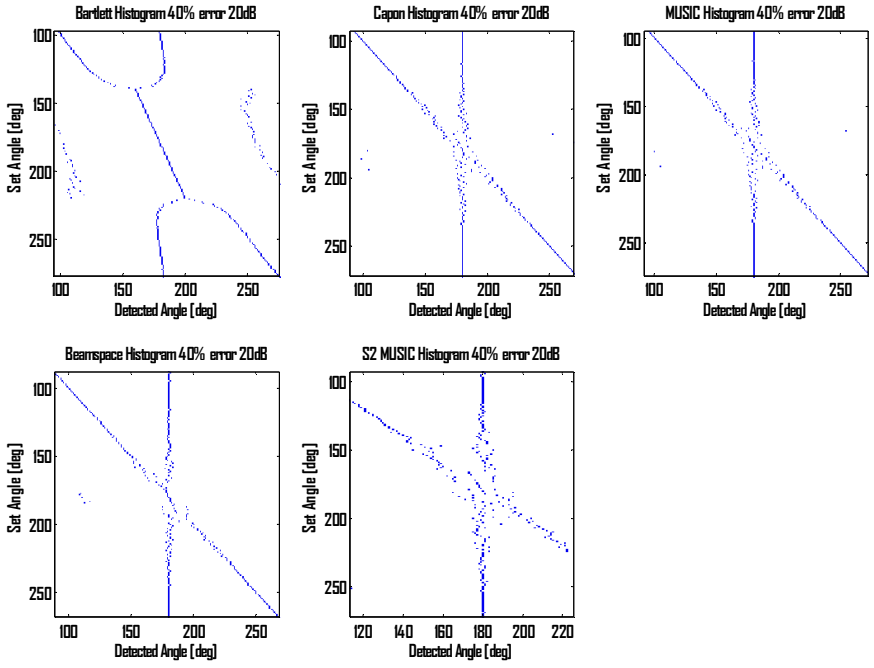

Figure 40 Histogram for various algorithms when 40% amplitude error is induced

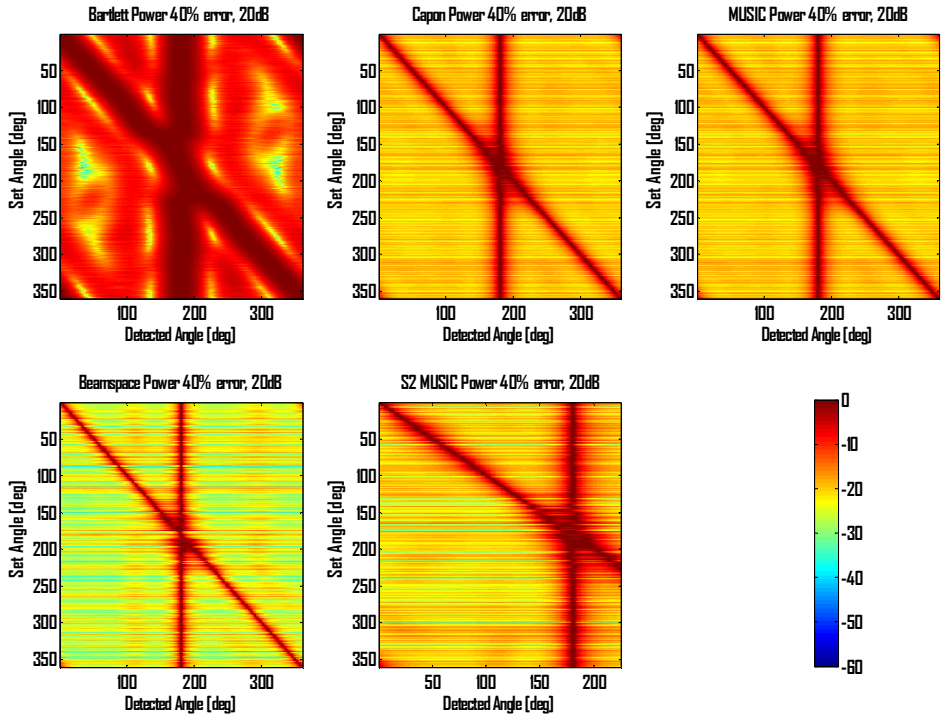

Figure 41 Spectrum Power plot for various algorithms
when 40% amplitude error is induced

Computational Complexity

In this section, the computational complexity of the algorithms is discussed. Three major computational steps are involved to obtain the bearing estimates. The first major step consists of obtaining the covariance matrix, which requires matrix multiplication. The second step involves either computing the matrix inverse (for Capon) or applying the eigenvalue decomposition on the signal covariance matrix in the subspace methods. The final step consists of computing the spectrum of the algorithm involved, which involves a double matrix multiplication.

For a received signal vector consists of M columns and P rows, computing the signal covariance matrix involves $2MP$ operations, which is done for all the algorithms

except S2 MUSIC. Since only a limited number of elements is chosen for S2 MUSIC (usually half of the elements compared to other algorithms) an obvious computational reduction is obtained when S2 MUSIC is used. Once the signal covariance matrix is obtained, the inverse or eigenvalue decomposition which is of $O(M^3)$ is computed. Reducing the number of elements in S2 MUSIC is analogous to a reduced covariance matrix size, and with $O(M^3)$ the computational reduction is significant. The final stage consists of obtaining the spatial pseudo-spectrum. The conjugate transpose of the steering vector$[S \times M]$ is multiplied by the noise covariance matrix (also reduced in the case of S2 MUSIC), and the result is then multiplied by the steering vector of size $[M \times S]$, where S is the number of sectors used to quantize the azimuth range. The required number of operations is $4SM$, in addition to the computation needed to obtain the noise covariance matrix. In this step S2 MUSIC saves computation not only in obtaining the noise covariance matrix, but also in obtaining the spectrum, since the number of sectors S is reduced significantly (at least by half).

When beamspace is used, the received signal vector is pre-multiplied by a beamformer matrix, and depending on the number of modes used, the size of the covariance matrix is reduced (when 3 modes are used corresponding to 7 beams the covariance matrix is reduced by one). Compared to beamspace MUSIC, S2 MUSIC is more computationally efficient since it does not require pre-multiplying the receiver data vector by the beamformer matrix, in addition to the fact that S2 MUSIC uses a reduced number of sectors in obtaining the spatial pseudo-spectrum, which is not the case for beamspace MUSIC.

All the above observations lead to one conclusion, S2 MUSIC is computationally more efficient than MUSIC and beamspace MUSIC because both the number of elements used and the number of sectors are reduced, which leads to less computational burden when obtaining the DOA estimates.

Simulation Results Discussion

In this chapter, the accuracy and resolution of the algorithms have been investigated for a variety of parameters. The results indicated that under low SNR the algorithm accuracy and resolution are affected dramatically, suggesting that when building the necessary hardware, The SNR needs to be high enough to mitigate its effects on the DOA estimates. Phase error affected the accuracy and resolution of the algorithms more so than amplitude error, pointing out that proper design of the hardware and accurate phase calibration will be imperative to reaching high resolution DOA estimates.

When S2 MUSIC is used, 4 elements or more are needed, since using a lower number will cause significant error in accuracy and cause degradation in resolving azimuthally close sources. Another note worth mentioning concerns the relationship between the peak-to-floor ratio and resolution capability of the algorithms. It was clear from the simulations that when the measurement floor rises, it causes a decrease in the resolution capability of the algorithms. It was evident that using a low number of samples cause errors in the estimates and resolution, so using a large number of signal samples is also important. Mutual coupling was also investigated and simulation results showed that even at very high SNR, it caused a significant error in accuracy. Finally, the

examination of computational efficiency indicates that S2 MUSIC is significantly more efficient in terms of computation when compared to the other high resolution algorithms. Though S2 MUSIC is more susceptible to low SNR and mutual coupling, its performance is comparable to the conventional MUSIC.

In the next chapter, the design and implementation of the necessary hardware to achieve high resolution DOA estimation a discussed. How to mitigate the phase errors in the system along with mutual coupling is also investigated.

CHAPTER FOUR

HARDWARE DESIGN AND IMPLEMENTATION

Many issues face engineers when designing receivers. The challenges do change with the application but some issues are to be addressed in any situation. The dual goals of making a receiver that exhibits high dynamic range while being very sensitive are indeed hard to achieve. The power of the signals of interest might vary from very high to the point of causing saturation to the input sensitive components, to very low making the signal hard to distinguish from noise. A high dynamic range receiver is necessary to avoid non-linear affects which can drive the circuits into compression, which decreases the gain, and can bias results where amplitude measurements are a consideration.

When GHz RF signals are of interest, mixing usually takes place in the receiver and causes a multitude of issues. Heterodyne mixing in particular causes intermodulation and the IF has to be carefully placed to avoid being in the vicinity of harmonics resulting from the mixing operation. In addition, LO re-radiation causes major issues. Leakage from the local oscillator seeps out to the antenna causing unwanted radiation at the antenna in the receiving mode. Proper filtering should also be considered to avoid aggregate noise build up on the RF and IF sides. In the case where direct conversion is used, going from RF to baseband without the intermediate IF stage, the lower sideband folds over and causes signal interference.

The 8-channel receiver board, designed and implemented by the author, provides the hardware piece responsible for taking the 5.8 GHz signal to baseband and delivering the information to the DAQ card. A single stage image reject (IR) mixer was considered

to achieve frequency translation to baseband. The RF signal is filtered, amplified, and filtered once again, and then mixed using a distributed local oscillator. The choice of the baseband bandwidth is solely dependent on the speed at which one can digitize the signals. The manual gain control settings are used to provide an acceptable level to the DAQ card. A simplified block diagram for one channel is shown in Figure 42.

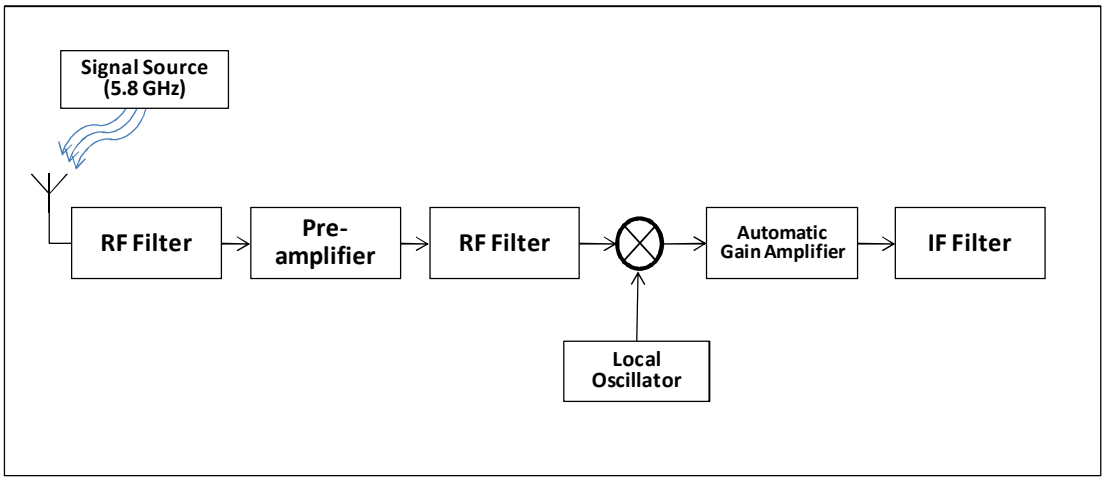

Figure 42 Simplified block diagram for one channel in the receiver board

The receiver board went through two design phases. In the first design, the implementation was done in two stages, a dual channel board was first constructed and each of the components was tested to make sure that the design parameters were met. Once the two channels were tested successfully, the full 8-channel receiver board was designed using PADS and fabricated. Troubleshooting revealed that on the RF side, the pre-amplifier input and output ports were switched in the footprint requiring some repairs which at 5.8 GHz causes major cross channel interference. In the first design, both the LO drive and the variable gain amplifiers at IF were used as evaluation boards and were

not incorporated in the layout of the receiver board. Figure 43 illustrates the first version of the receiver board.

Figure 43 Snapshot of the first revision of the receiver board

The second version was designed to include a multitude of improvements. The upgrades consisted of improving the front end design (by including the low noise pre-amp), incorporating an onboard phase locked loop (PLL) for computer controlled local oscillator generation, incorporating onboard variable gain amplifiers with independent gain control for channel gain matching, and adding switchable IF low pass anti-alias filters to optimize for low speed or high speed data acquisition. A single PLL was used for LO generation and symmetrically distributed to the eight channels. An alternate approach that was not implemented consisted of including an individual PLL for each channel controlled by a numerically controlled oscillator to individually adjust the channel phases. This would have allowed for more flexibility at the expense of hardware complexity. Thought was also given to make the receiver bidirectional by eliminating

the RF preamplifiers and including the ability to bypass the variable gain amplifier. The translator could then be used both as a digital BF or a DOA estimation receiver. It was decided that this can be considered in later revisions.

In the implementation of the receiver board, the printed circuit board (PCB) material chosen was FR4 and cost was the main driver behind the choice. The overall physical size of the board was determined by the connector spacing and shielding goals. The main goals behind designing a board enclosure were to shield each of the 5.8 GHz RF input channel from one another, and to provide mechanical rigidity to the board to assure phase stability.

A total of four layers were used for the PCB. The top and bottom layers were organized such that the RF components were on top and IF components were on bottom. The ground layer was directly under the RF layer, followed by the power distribution layer. To minimize the phase differences between channels, path symmetry was applied to the LO distribution and to the RF input paths. A coplanar waveguide was used for the 5.8GHz signals. The board manufacturer, Prototron, provided the exact board properties for calculating the correct line spacing and gap for a 50 Ohm system impedance. Symmetry was also used on the IF side of the board to insure that all the IF channels are in phase. The width of the traces on the RF side was calculated using AppCAD software as shown in Figure 44, to achieve 50 ohm impedance given the material dielectric along with the frequency of operation. The trace width along with the ground clearance was calculated for the RF trace in the receiver board. Given the properties provided by the

manufacturer, the trace width was 0.022 inches and the gap between the trace and the ground plane was 0.006 inches.

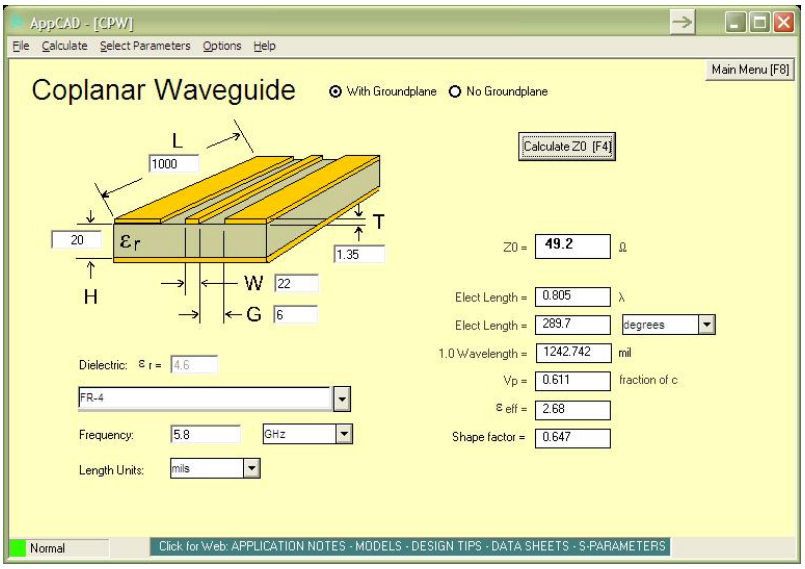

Figure 44 Example of use of AppCAD software to calculate the width and ground clearance for the RF traces in the receiver board

The wall thickness wes determined by the screws that were used to attach the top and bottom lids. The enclosure was designed (by Aaron Traxinger) such that the 5.8GHz sections of the board are shielded from each other. Each side of the box has a lid which enables easy access to the board when troubleshooting is required. The IF connectors were designed to mate directly (without the need for cables) with the high speed A/D board. The lid for the IF section was designed with a stepped lip to create some shielding from external RF interference. Electromagnetic interference (EMI) filtered power input terminals along with an EMI filtered RS232 port were used to minimize external RF interference from infiltrating the enclosure. Closely spaced screws were used to insure a tight connection to the exposed ground connection. Extra screws

were used in the RF section lid to minimize the amount of RF leakage between each RF pocket.

A snap shot of the front side of the receiver board is depicted in Figure 45, where the RF inputs are situated on left side. The RF channels were egg crated for channel-to-channel isolation. The LO distribution is situated on the right side.

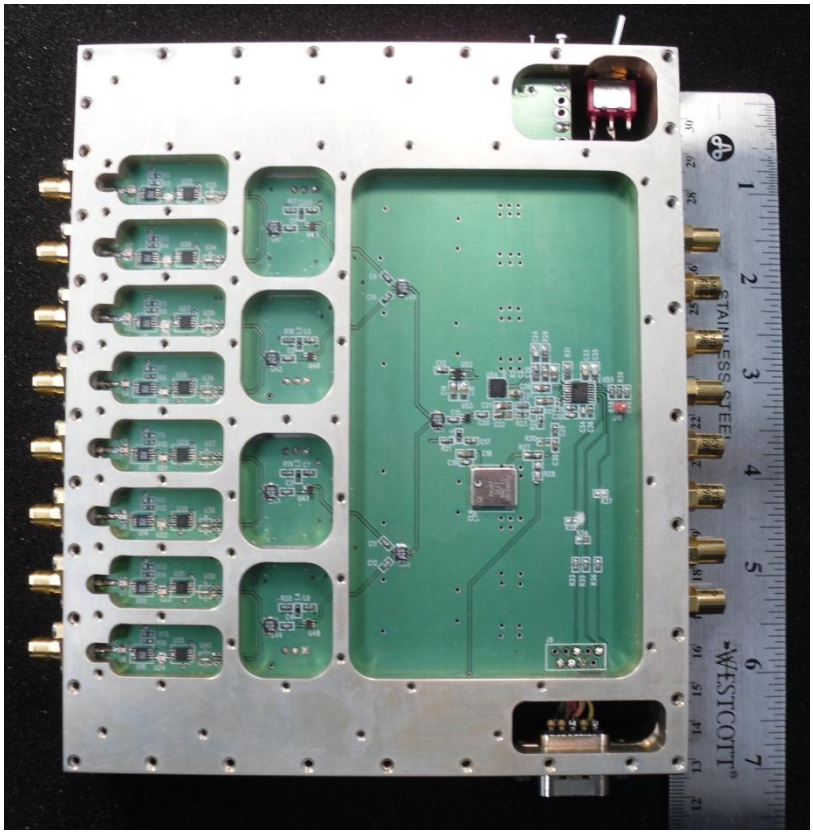

Figure 45 Snap shot of the front side of the receiver board
in the aluminum enclosure

Figure 46 depicts the back side of the receiver board which contains the IF components. Starting from the right hand side the IF signal generated by the mixer is fed to the variable gain amplifier chip and then the amplified IF signal is filtered either though the 1MHz or 10 MHz lowpass filters.

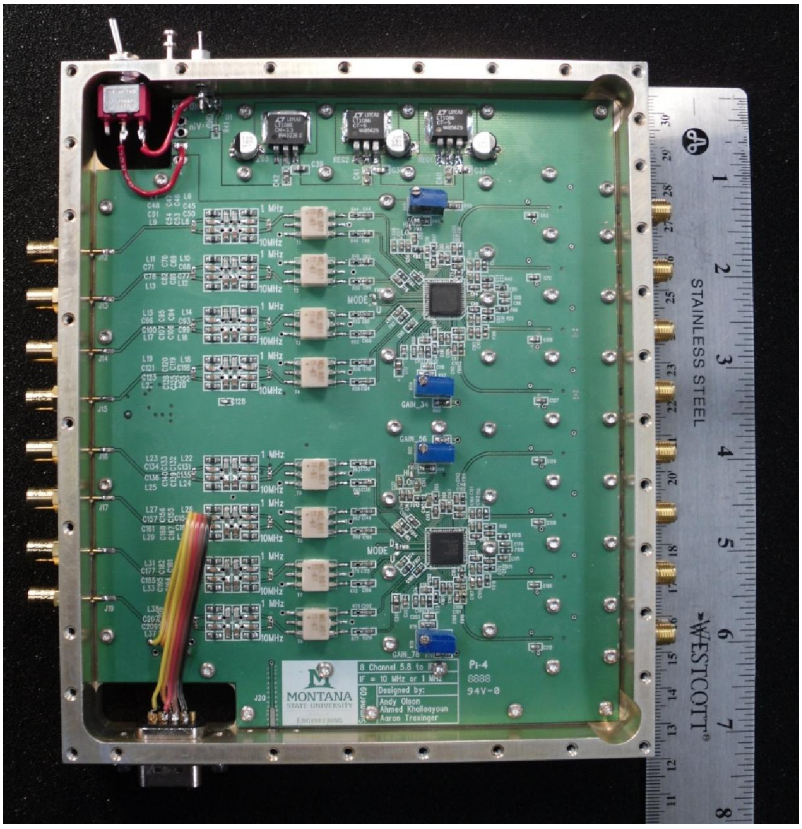

Figure 46 Snap shot of the back side of the receiver board
in the aluminum enclosure

The following sections discuss the RF side, LO distribution, and IF side. Detailed schematics of the second version receiver, along with the layout of the RF and IF layers, a bill of materials, and the enclosure drawings are provided in Appendix A.

RF Side

The RF side of the receiver board includes the RF input and the LO distribution. The 5.8 GHz signal(s) received by the array elements are fed to the receiver board via SMA female connectors and the signal is filtered using a Johanson Technology, Inc P/N

5515BP15B725 filter. The bandpass filter operates from 5.150 GHz to 5.875 GHz, introduces a maximum of 1.5 dB insertion loss and has a minimum return loss of 9.5 dB. The signal is then amplified using an HMC318 Hittite amplifier. This low noise amplifier was chosen for its low noise figure (2.5 dB) and excellent return loss performance. It provides a typical gain of 9 dB. The signal is then filtered again and fed to the RF input of the mixer. The HMC488 mixer was used, and is a double balanced mixer with an integrated LO amplifier. The LO amplifier can be driven from 0 to +6 dBm and requires a single supply of +5V.

Each of the LO inputs of the mixers are fed through the on board LO distribution. The LO signal is generated using the AD4106 PLL frequency synthesizer and the incorporated LO design was borrowed from the Analog Devices EVAL-ADF411XEB1 evaluation board. A detailed schematic of the LO drive design is shown in Appendix A. The LO signal is controlled using a PC interface provided by Analog Devices. The LO signal is then distributed to all the LO input ports of the mixers with the help of a Mini-Circuits GP2X+ power splitter/combiner. The power splitter is wideband (2.9 GHz to 6.2 GHz) and at 5.8 GHz the splitter has a typical isolation of 18.7 dB. It has an excellent amplitude unbalance (0.05 dB typical) and good phase unbalance (3 degrees typical). At each stage of the power division the Hittite HMC311 amplifier was used such that the power of the signal matches the LO drive power required by the mixer.

IF Side

The IF side contains the variable gain amplifiers and the IF filters. Analog Devices AD8334 variable gain amplifiers were used for this project. The AD8334 is a quad-channel, ultralow noise variable gain amplifier with a 100 MHz 3dB bandwidth. The datasheet specifies that this amplifier can produce up to 55.5 dB of gain, but this statement is not totally valid since with the proper output matching network only 30 dB of gain can be achieved. One can, however, increase the gain of the amplifier by reducing the resistance values of the output matching network. A detailed schematic of the variable gain amplifiers is shown in Appendix A.

Two IF filters paths were used on this board to accommodate for low and high speed data acquisition. The filters used were designed with the help of the Genesys software. The filters are a 3 pole traditional (or Butterworth) design and the schematics of the filters are given in Appendix A.

Receiver Board and Performance

The receiver board DC power is provided by two regulated voltage supplies, +5V and +3V. According to the specifications provided by the components' manufacturers, the board should draw 70 mA at 3 V and 736 mA at 5 V, and the total power consumed by the receiver board is 3.89 watts. The board's actual current draw is 889 mA, higher than expected because typical specifications were used. The RF conversion loss was measured to be -1 dB, and the IF section was also tested and showed 30.5 dB gain at each channel. If more gain is needed, the matching network at the output of the variable gain

amplifier can be modified, that will cause some mismatch but can results in a higher gain. Tests with the frequency synthesizer showed noisy behavior and inability of the PLL to lock. This problem was solved by adding the appropriate capacitance to the regulator terminals to filter out the noise leaking into the synthesizer. The RF channel-to-channel isolation was measured using the HP 8720D network analyzer, and isolation between adjacent channels was measured to be in excess of 65 dB.

The receiver board magnitude and phase behavior tests were carried out after accomplishing the basic RF, IF, and LO functionality tests. The set up consisted of the Anritsu 68369 function generator as the RF input, and the signal from the function generator was divided using the Mini-Circuit ZX10R-14-S+ splitter. Channel 1 of the receiver board was used as the reference while the unused channels were terminated. The Tektronix TDS 3054B oscilloscope was used to measure the output signals (16 point averaging was used when the data was recorded). The power at the input of the receiver was set to -40dBm. The test was carried out for both the 1 MHz channels and the 10 MHz channels and channel-to-channel phase and magnitude variations were recorded as the IF bandwidth was varied. For the 1MHz Channels, the IF frequency was varied from 100KHz to 1500 KHz in 100 KHz steps while for the 10 MHz channel the IF bandwidth was varied from 1MHz to 15 MHz in 1 MHz steps. The center frequency was set to 5.8 GHz and the synthesizer frequency was varied accordingly to provide the appropriate baseband frequency. Measurements for the 1 MHz channels are shown in Table 1, where all the phase measurements are relative to channel 1 and the magnitude variation for channel 1 is shown in Table 2. Phase variations vs. the IF frequencies are plotted in

Figure 47 (relative to channel 1). For the 10 MHz channels, the measurements are shown in Table 3 and Table 4 shows the amplitude variation for channel 1. Measurements indicate that the amplitude variation is less than 2 dB from the channel exhibiting the largest voltage to the one showing the lowest in both the 1 MHz and 10 MHz channels. The relative phase difference is very stable at about 500 KHz in the 1 MHz channels and at about 5 MHz in the 10 MHz channels. Beyond that point the relative phase difference varied dramatically. This variation is due to the IF filters not having a matching frequency response, since each filter, due to the tolerance of the parts exhibits a different ripple effect along with a different 3dB point. The difference in amplitude caused by the ripple effect in the filters translates into phase differences. For the DOA estimation algorithms, precise knowledge of the phase and amplitude is imperative for good performance. To avoid phase variations within the IF band, the filters should be designed with a 3dB bandwidth twice as big as the desired IF bandwidth to avoid the ripple effect and obtain a flat phase response within the band of interest.

Table 1 Magnitude and phase variation for all channels for different IF frequency (1 MHz), magnitudes are recorded in mV and the angles are recorded in degrees

Frequency (KHz)	Channel 2		Channel 3		Channel 4		Channel 5		Channel 6		Channel 7		Channel 8	
	Mag	Ang	Mag	Ang	Mag	Ang	Mag	Ang	Mag	Ang	Mag	Ang	Mag	Ang
100	133.7	-10.5	120	-11.9	106	-22.7	116	34	120	19.5	111.3	37.5	111.7	30
200	131.5	-10.7	118.8	-12.0	104.3	-22	114	34	118.5	20	110	37.1	107	29.1
300	136.7	-10.7	124	-11.5	108	-22	118	34.9	122.7	20	114	37.9	108	28
400	147.4	-10.7	133.2	-10.5	116.3	-22.2	127.4	35.5	131.8	20.5	124	38	111.7	26.7
500	164.8	-9.0	150.1	-9	130	-21	143	37.5	147.7	22	140	41.5	119	23.5
600	184.5	-7.0	167.5	-6.7	146	-20	160	40	167	24.5	158	43.5	131.4	19
700	194	-4.5	174.8	-3	156	-17	168	44	175.7	28	165	48.5	145.8	14.5
800	185.7	-2.5	165	-1.5	150	-15	158	45.5	167	30	155.8	50	153.5	14
900	175.4	0	154	0	139	-12	147	48.5	157	33	146	52	149.2	17
1000	183.3	+7.5	162	7	142	-6.5	154	55	165.4	40	154	59	140	22.8
1100	217.8	+36	200	36	172.8	15	189	84	199	70	189	90	138	26.5
1200	150	76	134	80	137	59	127	128	130	112	121.8	132	158	29
1300	70	41	60	44	62	30	56	90	60	75	54.6	94	175	17
1400	35	4	30	7	30	-5	28	54	29.5	38	27	57	95	18
1500	19.6	-5	16	-4.5	16.9	-15	15	42	17	27	15.3	46	42	20

Table 2 Channel 1 amplitude variation for different IF frequency (1MHz)

Channel 1 (KHz)	Mag (mV)
100	129
200	125
300	128
400	135
500	145.8
600	159
700	164
800	152.2
900	134.5
1000	121.6
1100	122.9
1200	152.8
1300	177.3
1400	85.8
1500	39.9

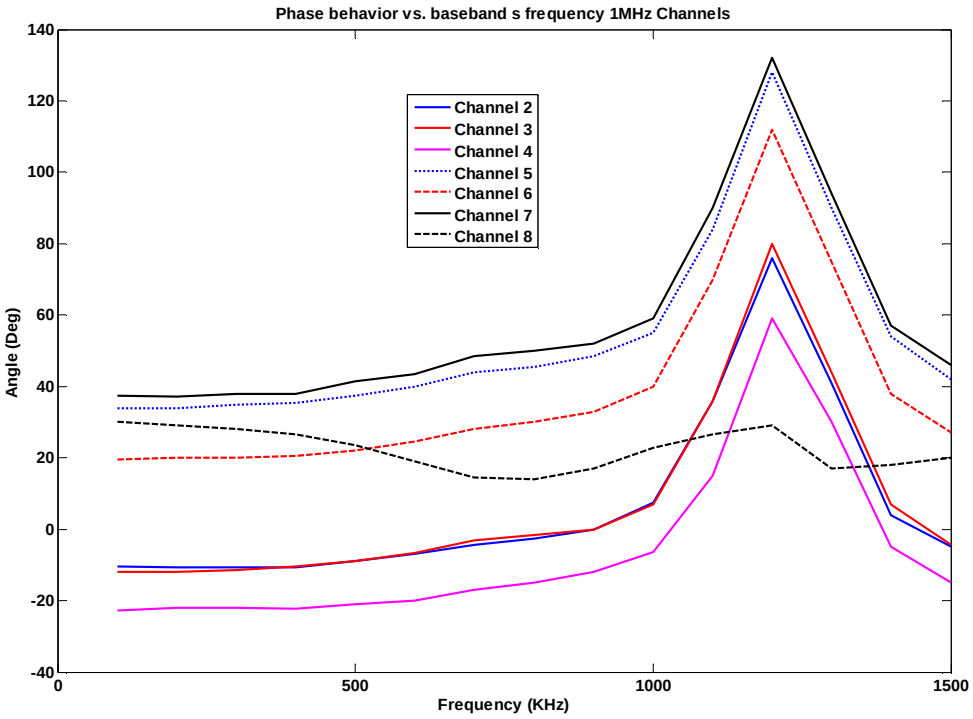

Figure 47 Plot of phase variation for all channels relative to channels for different IF frequency for the 1MHz channels

Table 3 magnitude and phase variation for all channels for different IF frequency for 10 MHz channels, magnitudes are recorded in mV and the angles are recorded in degrees

Frequency (KHz)	Channel 2		Channel 3		Channel 4		Channel 5		Channel 6		Channel 7		Channel 8	
	Mag	Ang	Mag	Ang	Mag	Ang	Mag	Ang	Mag	Ang	Mag	Ang	Mag	Ang
1000	118	-11.5	111	-12.5	97.8	-24	107	30.5	108	20.5	106	36	106	31.5
2000	106	-12.5	101	-13	90	-24	98	29.8	101	20.5	99	37	99	32.5
3000	97	-13.5	93	-13.5	82	-25	88.7	29	95	21.5	94	38	94	34
4000	92	-14	88.5	-13.5	78	-25	84.5	29	93.8	24	93	40	93.5	37
5000	92	-16	88	-15	78	-25	84.5	28	98	26	97	45	98.8	41
6000	98	-18.5	95	-16	84	-25	90	26.5	107	32	106	50	108	49
7000	110	-20.5	106	-17.5	91	-25.5	100	24.5	116	38	112	58	114	57
8000	121	-22	114	-18	95	-26.5	108	23	112	42	108	60	108	61
9000	120	21	111	-17	90	-27	104.7	23.5	104	41	100	60	101	61
10000	108	-19	101	-16	80	-29	96	25	107	44	104	63	111	68
11000	103	-19.5	98.5	-15.5	80	-31	94	25.5	128	70	128	94	113	111
12000	112	-28	111	-19	94.5	-40	108	21	70	105	60	128	46	131
13000	114	-43	96	-26	98	-41	93.7	15.5	27	65	23	85	19	82
14000	54	-28	40	-20	39	-29	40	21	13	33	11	52	9	50
15000	23	21	19	-17	17	-28	18	23	na	na	6	46	Na	Na

Table 4 Channel 1 amplitude variation for different ID frequency (10MHz)

Channel 1 (KHz)	Mag. (mV)
500	117
1000	113
1500	110
2000	103
3000	94
4000	90
5000	91
6000	97
7000	107
8000	113
9000	107
10000	98
11000	99
12000	120
13000	91
14000	36
15000	16

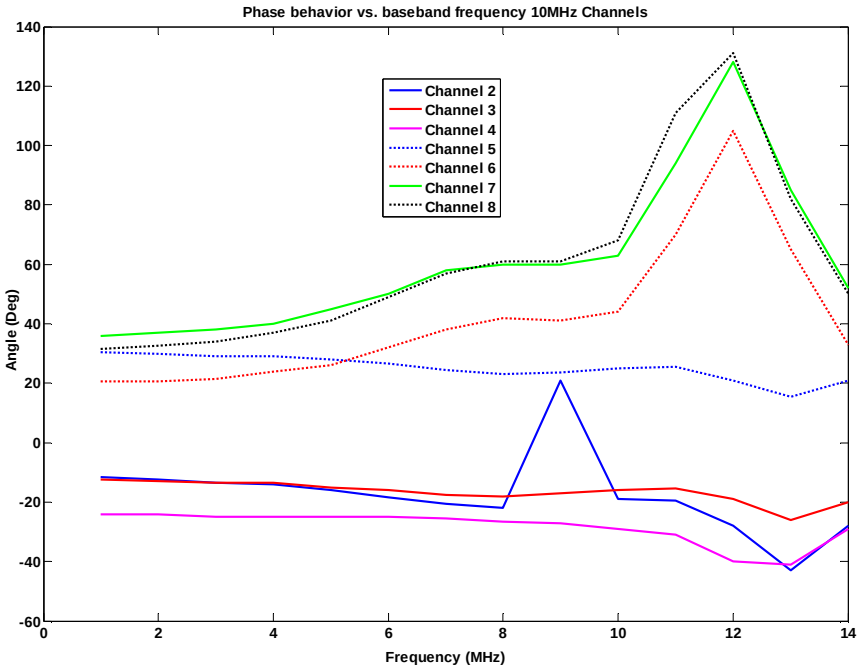

Figure 48 Plot of phase variation for all channels relative to channels for different IF frequency for the 10 MHz channels

The measurements shown above were repeated and have shown minimal phase drift over time. One should note that changing the center frequency does affect phase,

calibration should be applied for the frequencies of interest. For example, changing the carrier frequency from 5.80 to 5.82 GHz resulted in different phase readings.

Hardware Calibration

DOA estimation algorithms were designed with the assumption that the signals are acquired with no magnitude or phase differences between the antenna elements and that no mutual coupling occurs within the antenna array. These assumptions are never met in real world situations and are the main factors in degrading the performance of high resolution DOA estimation algorithms. Here we present two calibration methods, a conventional one based on current injection and an advanced method that relies on the EVD of the obtained covariance matrix to construct a correction matrix to mitigate all the unwanted effects.

Current Injection Using a Center Element

The current injection method adopted accounts for the magnitude and phase differences in all channels from the antenna head to the input of the DAQ card (the overall system, not only the receiver board). This is achieved by adding a center element to the UCA. The center element is fed with a 5.8 GHz signal reaching each of the antenna elements at the same time. Using the first antenna element as a reference, the relative phase difference between all the channels is easily calculated. Using a -10dBm signal from the function generator, the phases relative to channel 1 were measured with the scope using the 16 point averaging. The measured phases for the 1MHz channels and the 10 MHz channels are recorded in Table 5 and Table 6, respectively.

Table 5 Phase measured relative to channel 1 for the 1 MHz channel for a varying IF frequency (phase was recorded in degrees)

Frequency(KHz)	Chan2	Chan3	Chan4	Chan5	Chan6	Chan7	Chan8
100	-11	-8	0	66.6	43	56.8	40
200	-11	-8.5	1.5	65.5	43	60	40
300	-11	-5	3	67	43	61	39
400	-11	-7	2	67	43	61	37
500	-10	-6	0	68	44	61	34
600	-8	-3.5	-1	71	45	58	30
700	-5.5	0	-5	75	47	56	24.5
800	-3.5	1.5	6.5	78	50	56	23
900	-1	3	-2	80	52	58	27
1000	5	9	4.4	86	60	66	32
1100	30	34	23	112	86	93	37
1200	78	82	66	153	133	137	40
1300	44	50	43	129	104	106	28
1400	4.6	10	2.8	84	60	55	28
1500	-5	-1.5	-9	72	50	43	33

Table 6 Phase measured relative to channel 1 for the 10 MHz channel for a varying IF frequency (phase was recorded in degrees)

Frequency (KHz)	Chan2	Chan3	Chan4	Chan5	Chan6	Chan7	Chan8
500	-15	-14	-7	40.5	32	31	48.5
1000	-15.5	-15	-9	41	32	31.5	48.5
1500	-16.5	-16	-9	40	31	31.5	49
2000	-16.5	-16	-9.5	40	31	32	49
3000	-17.5	-17.5	-10.5	38	32	33.5	50.5
4000	-19	-19	-12	37	33	35	53.5
5000	-20	-20	-13	36	35	38	57.5
6000	-22	-22	-14	34	39	43	64.5
7000	-26	-24	-15.5	32	45	50	73
8000	-28	-26	-18.5	30	47	53	77
9000	-28	-25.5	-19.5	29	46	52	76.5
10000	-25	-25	-20.5	30	48	54	82
11000	-25	-25	-24	30	70	83	124
12000	-32	-28	-31	25	106	120	146
13000	-46	-37	-38	16	70	78	100
14000	Low sig	Low sig	Low sig	Low sig	Low sig	Low sig	Low sig
15000	Low sig	Low sig	Low sig	Low sig	Low sig	Low sig	Low sig

Compared to the measurements in Table 1 and Table 3, the addition of the antenna head and the cables did change the relative phases and beyond 500 KHz (for the 1MHz channel) and 5 MHz (for the 10 MHz channels) the relative phases are not constant.

To account for the phase differences in the system, the receiver data vector

$$V_{phase} = [1, e^{\Delta\varphi_{21}}, e^{\Delta\varphi_{31}}, \dots, e^{\Delta\varphi_{m1}}]$$

is simply pre-multiplied by the vector V_{phase} containing the measured phase difference. The channel-to-channel magnitude variation is accounted for by normalizing the signals acquired by the antenna array elements to the same level. If $x_m(t)$ represents the signal acquired at the mth element, the normalization takes the form

$$x_{m-norm}(t) = \frac{\left(x_m(t) - \overline{x_m}(t)\right)}{std(x_m(t))}, \qquad m = 1, \dots, M$$

where, $\overline{x_m}(t)$ represents the vector mean, and std(.) represents the data standard deviation.

Blind Offline Calibration Method

The method presented here is a modified approach to the method presented in [45]. Contrary to that method, the approach presented here assumes no knowledge of the bearings from which the data sets are collected. In addition, though the EVD is used on the signal covariance matrix, the way the measured and estimated steering vectors are extracted and normalized is different.

To mitigate the magnitude, phase, and mutual coupling effects, a correction matrix $\vec{C}^{new}$ is extracted such that $\vec{C}^{new} = \vec{C}^{-1}$ where, *C* represents the coupling matrix containing the magnitude and phase difference from one channel to another, and mutual coupling effects. The receiver data vector with the unwanted effect is then written as,

$$\vec{X}^{meas} = \vec{C}\vec{A}\vec{S} + \vec{N}$$

and the constructed correction matrix is applied to mitigate those effects as,

$$\vec{X}^{new} = \vec{C}^{new}\vec{C}\vec{A}\vec{S} + \vec{N} = \vec{A}\vec{S} + \vec{N}$$

Since we do not have knowledge of the exact bearings, we need to use an iterative process to converge to those estimates. The latter is achieved by pre-multiplying the received data vector by an estimated correction matrix using the algorithm of choice (MUSIC in our case) to estimate the bearings which are used to construct the estimated steering vector. The estimated steering vector is used to construct an improved correction matrix and the process is repeated until the rate of change in the phase between the former and the new correction matrix is minimized to a preset threshold. A detailed pseudo algorithm is shown below, where

- Q is the number of independent data sets collected, $Q > M$
- $\boldsymbol{x}_q(t)$ is the received signal vector for an incoming signal from ϕ_q, where q = 1,.., Q
- T is number of samples
- $\boldsymbol{X}_q$ the received signal matrix of size $[M \times T]$ for an incoming signal from ϕ_q
- $\hat{\boldsymbol{R}}_q = \frac{1}{T}\boldsymbol{X}_q \boldsymbol{X}_q^H$ is the signal covariance matrix
- $\boldsymbol{V}_q$ is the eigenvector corresponding the largest eigenvalue
- $\boldsymbol{a}_{mea,q}$ is the normalized measured steering vector
- $\boldsymbol{A}_{mea}$ is the measured steering matrix of size $M \times Q$
- $\boldsymbol{C}_p$ is the distortion matrix
- P is number of iterations

- $\boldsymbol{a}_{e,q}$ is the estimated steering vector with known array geometry for an incoming signal from ϕ_q
- $\boldsymbol{A}_e$ is the estimated steering matrix of size $M \times Q$

---------- Start of algorithm ----------

For $q = 1,...,Q$

- Collect $[M \times T]$ data matrix $\boldsymbol{X}_q$
- Compute the signal covariance $\hat{\boldsymbol{R}}_q$
- apply the EVD to $\hat{\boldsymbol{R}}_q$ and take the eigenvector $\boldsymbol{V}_q$ that correspond to the largest eigenvalue
- Obtain measured steering vector
- For $m = 1,\ldots, M$, the m-th entry in vector $\boldsymbol{a}$
- $a_{mea,q}(m) = V_{mea,q}(m) / V_{mea,q}(1)$
- End
- Construct the measured steering matrix
- $\boldsymbol{A}_{mea} = [\boldsymbol{a}_{mea,1} \ldots \boldsymbol{a}_{mea,Q}]$,

end

The next loop represents the iterative process that converges to the actual bearing from which the sources have been emitting. P is the number of iterations and it can be bounded by a threshold governed by the rate at which the phase is changing between the former and the new correction matrix.

- Initializes the correction matrix, $\boldsymbol{C}_p = \boldsymbol{I}$

- Use iterations to converge to actual sources bearings

  For $p = 1,\ldots, P$

  For $q = 1,\ldots, Q$

$$\boldsymbol{X}_{\boldsymbol{new},\boldsymbol{q}} = \boldsymbol{C}_{\boldsymbol{p}}^{-1}\boldsymbol{X}_{\boldsymbol{q}}$$

- Calculate covariance matrix

$$\hat{\boldsymbol{R}}_{new,q} = \frac{1}{T}\boldsymbol{X}_{new,q}\boldsymbol{X}_{new,q}^{H}$$

- Use MUSIC DOA estimation algorithm to estimate ϕ_q
- Compute steering vector with known array geometry $\boldsymbol{a}_{e,q}$
- Construct the estimated steering matrix

$$\boldsymbol{A}_e = [\boldsymbol{a}_{e,1}\ldots\boldsymbol{a}_{e,Q}],$$

End

- Compute the correction matrix

$$\boldsymbol{C}_{p+1} = \boldsymbol{A}_{mea}\boldsymbol{A}_e^H\left(\boldsymbol{A}_e\boldsymbol{A}_e^H\right)^{-1}$$

- Compute phase difference between the ideal setting and the actual

  If

$$\sum_{i,j}\left|angle\left[\boldsymbol{C}_{p+1}(i,j) - \boldsymbol{C}_p(i,j)\right]\right| < threshold$$

  Break loop

  End

---------- end of algorithm ----------

The algorithms shown above generated a correction matrix that accounted for the phase and mutual coupling errors in the system. The resulting mutual coupling coefficients generated by the correction matrix were comparable to adjacent element mutual coupling measurements. The phase difference between channels generated by the correction matrix are also comparable to the measurements recorded by the center element injection current method. The latter comparison was done to validate the correction matrix.

The calibration algorithm above was tested and compared to the conventional injection current method and showed significant improvement on high resolution DOA estimation algorithms (results are shown in the following chapter). The calibration method shown here is an offline method, yet, if one requirement (having access to data from different bearings) is satisfied it can be used as an online calibration method and can be run periodically as a self-calibration method to account for any changes in the system. As mention before, knowing the bearing of sources is not a requirement. The only requirement consists of having access to sets of signals from different bearings where the number of sets is larger than or equal to the number of elements in the antenna array.

CHAPTER FIVE

EXPERIMENTAL RESULTS AND DISCUSSIONS

In this chapter, the experimental procedure and DOA estimation test results are presented. A Single CW source and dual CW sources were used to test the algorithms discussed in Chapter 3 along with a wideband radio source. Both the 1MHz and 10 MHz channels in the receiver board were utilized. The full bandwidth of the 10 MHz channel was partially used due to the sampling limitation posed by the data acquisition system. A new A/D board will be available shortly and will allow full bandwidth utilization. The performance of the algorithms was measured in terms of the peak deviation from the true angle, 3dB peak-width, and the ratio of the known DOA estimates to the highest one (spatial spur free dynamic range). The system SNR was approximated using the periodogram function in Matlab. The results shown in this chapter underscore that mutual coupling compensation is imperative in reaching high resolution performance.

Experimental Setup

All the experiments were conducted in the anechoic chamber at the communication lab at Montana State University. One of the CW sources was generated from the Anritsu 68369 function generator; the other was generated from the ADF4106 frequency synthesizer evaluation board. The wideband signal was generated using the Harris radios. Two types of antennas (besides the UCA which is naturally used as the receiver antenna) were used in the set up, a horn antenna and a counterpose dipole antenna. The UCA was mounted on a turn table in order to be able to capture data from

signals emanating from different bearings. The reader should note that the bearings were compared to the results obtained by Bartlett after mutual compensation since the turn table does not yield accurate bearings and cannot be used as a reference.

In estimating the steering vector, we used 360 sectors to divide the field of view, which yields an inherent uncertainty of +/- 0.5 degrees in the presented measurements. In addition, since the turn table setup used for acquiring data does not yield accurate bearings, we relied on the estimates of Bartlett after mutual coupling compensation, the uncertainty of the estimate provided using the latter as the reference is traced back to the threshold set for the acceptable phase error between the former calibration matrix and the newly generated one.

Experimental Results

Single CW Source Test Results

A -10dBm signal generated by the function generator at 5.8 GHz was sent to the horn antenna, and the receiver board LO was set to 5.7993 GHz, producing an IF signal at 700 KHz using the 10 MHz channel. The signal was sampled at 2.5 MSPS per channel and 1000 samples were recorded. 24 sets of data corresponding to different bearings were acquired. The receiver board was covered with absorption foam (same material used in the anechoic chamber) because of the reflective nature of the metal used for the receiver enclosure. The receiver signal input was -50 dBm.

The system SNR was estimated by using the periodogram function in Matlab, and the estimated SNR for this particular test was 34.2dB, Figure 49 shows the periodogram

of the acquired signal at the 1st element of the antenna array. Results for before and after calibration along with results after mutual coupling compensation for one of the bearing are depicted in Figure 50 for Bartlett, Capon, MUSIC, beamspace MUSIC, and S2 MUSIC. It is clear that both the peak-width and the main peak-to-floor ratio are improved after phase calibration, but after mutual coupling compensation, the improvement is even more pronounced.

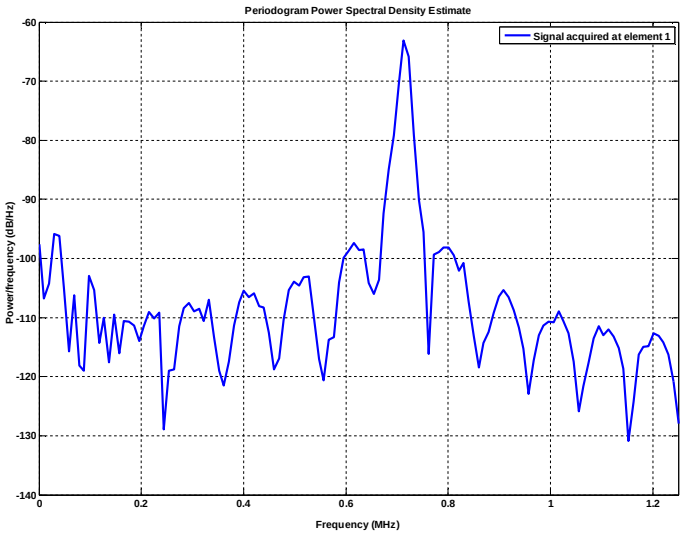

Figure 49 Periodogram of the received signal at element 1 of the UCA

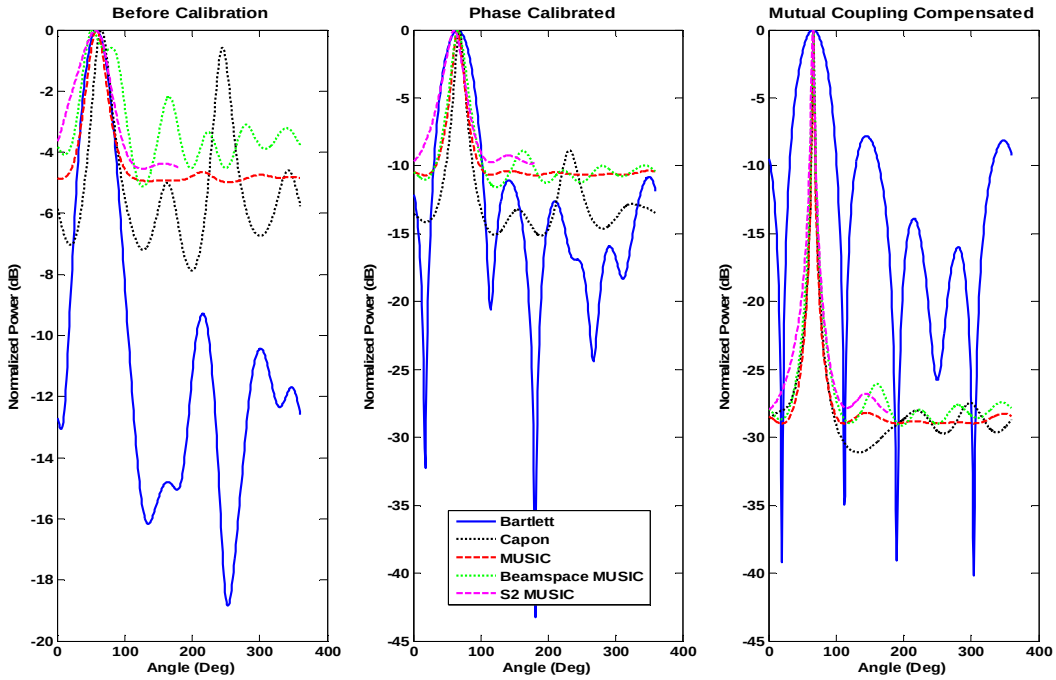

Figure 50 Estimated spectrum for the conventional and high resolution spectral algorithms. before calibration (left), after (middle) calibration, and after mutual coupling compensation

The results are quantified in Table 7 for the cases where the data vector was uncalibrated, phase calibrated, and mutual coupling compensated. The 3dB peak-width, main peak to the next highest peak ratio, and the deviation from the actual bearing are averaged over all 24 data sets. It is apparent that mutual coupling compensation provides noticeable improvement for all algorithms. The 3dB peak-width improved significantly from 44.7 degrees to 4.2 degrees for MUSIC for instance. After mutual coupling compensation, the main peak to the second highest peak ratio also showed a significant improvement, Capon went from having a false peak that is only 0.5 dB lower than the main peak to an average ratio in excess of 21 dB. The deviation from the true bearing improved significantly, rendering the algorithms very accurate after mutual coupling compensation.

Table 7 Algorithms performance averaged over the acquired data set (24 bearings)

	3dB peak-width (degrees)			Main peak to the second highest ratio (mean of the highest second peak) (dB)			Deviation from true peak (degrees)		
	Before cal	After center cal	Mutual coupling com	Before cal	After center cal	Mutual coupling com	Before cal	After center cal	Mutual coupling com
Bartlett	44.78	43.91	43.56	6.18	9.57	7.80	11.75	0.04	0
Capon	46.09	13.04	4.26	0.43	9.50	21.36	14.00	0.04	0.04
MUSIC	44.70	19.56	4.26	4.13	9.64	23.94	11.70	0.04	0
Beamspace MUSIC	51.22	19.04	4.52	3.06	8.89	23.20	7.50	0.79	0
S2-MUSIC	43.08	14.75	6.78	N2P	N2P	N2P	2.42	0.04	0.08

To demonstrate the consistency of the data depicted for a single source, 60 sets of data were acquired to quantify how the DOA estimation varies when the same estimate is of interest. The root mean square error (RMSE) results showed that except with Capon, all the other algorithms showed an excellent stability in the estimate. Capon exhibited a 0.84 degree variance over the 60 runs after mutual coupling compensation (1.38 degrees without calibration and 0.89 degrees with phase calibration).

A series of figures showing the estimated spectrum for all the algorithms of concern at all the measured bearings for two data sets including the one used to obtain the above results are given in Appendix B (single sources set 1). A second set of data was processed to further verify the results and they were comparable to the one shown in this section, the estimated spectrum for the algorithm for the second set of data is shown in Appendix B (single sources set 2).

Two CW Sources Results

Two sources, one generating from the function generator (5.8 GHz) and the other from the analog frequency synthesizer (5.7998 GHz), were used in this test (receiver board LO was set to 5.7993 GHz). The 1st and 2nd source were at 500 KHz and 700 KHz IF, respectively. The estimated true peaks were at bearings 10 degrees and 86 degrees. Results for before and after calibration along with results after mutual coupling compensation for one of the bearings are depicted in Figure 51 for Bartlett, Capon, MUSIC, beamspace MUSIC, and S2 MUSIC. Results for the 3dB beamwidth, 3rd highest peak, and bearing error are summarized in Table 8 when mutual coupling compensation was applied. The results indicate that the subspace method performed well, with a maximum 3dB beamwidth of 9 degrees (for beamspace MUSIC). The bearing error was within one degree of error and the third highest peak was in excess of 20 dB lower than the peaks of interest. Compared to the case where only one source was used, the 1st peak which resulted in a lower power compared to the 2nd peak had a wider 3dB beamwidth; besides the latter the bearing error and the ratio of the peak(s) to floor were comparable. The next section investigates how the difference in power between the 1st and 2nd sources affect the DOA estimates.

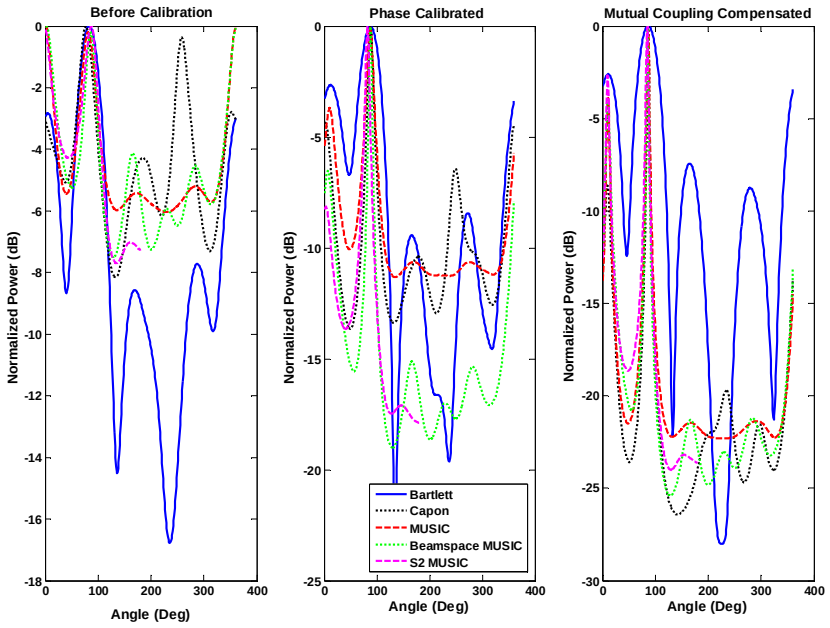

Figure 51 Estimated spectrum for the conventional and high resolution spectral algorithms. before calibration (left), after (middle) calibration, and after mutual coupling compensation

Table 8 Algorithm performance when two CW sources were used

	3 dB Beamwidth (degrees)		3rd highest peak (dBm)	Bearing error (dB)	
	1st	2nd		1st	2nd
Batlett	41	42	-7.5	0	0
Capon	12	5	-18.5	2	1
MUSIC	8	4	-21.5	1	0
Beamspace MUSIC	9	8	-21.5	0	0
S2 MUSIC	6	4	-23.5	0	1

Two CW Sources with Different Powers Test Results

Two sources, one generated from the function generator (5.8 GHz) and the other from the analog frequency synthesizer (5.7998 GHz), were used in this test (receiver board LO was set to 5.7993 GHz). The 1st and 2nd source were at 500 KHz and 700 KHz IF, respectively. The estimated true peaks were at bearings 2 degrees and 89 degrees. This test also investigated how the algorithms performance is affected as the power

difference between the two sources is varied. The power in the second signal was fixed and the first signal's power was varied such that difference in power between the two signals went from -10 dB to -35 dB in a 5 dB increments. Note that compared to the previous section, the power levels used for this set up were lower. The estimated spectrums for all varying power difference between the two signals for Bartlett, Capon, MUSIC, beamspace MUSIC, and S2 MUSIC are depicted in Figure 52, Figure 53, Figure 54, Figure 55, and Figure 56, respectively.

The first observation applies to Bartlett. It is clear from Figure 52 that once the power difference between the signals is lower than the sidelobe levels, the second source cannot be detected and is considered a sidelobe. This behavior is anticipated since Bartlett estimates are based on received power spectrum. Compared to all the remaining algorithms Capon did poorly when the power difference was increased.

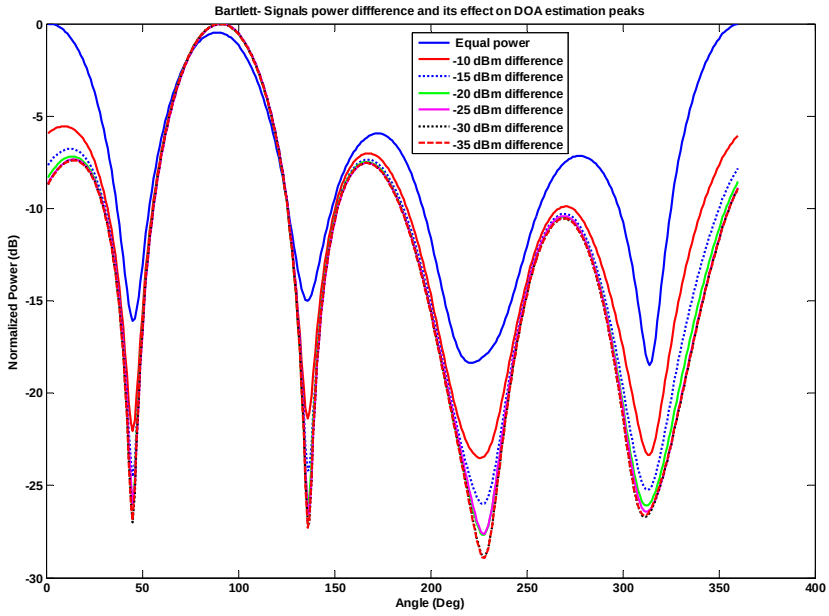

Figure 52 Estimated Spectrum for Bartlett for a varying power difference between the impinging sources

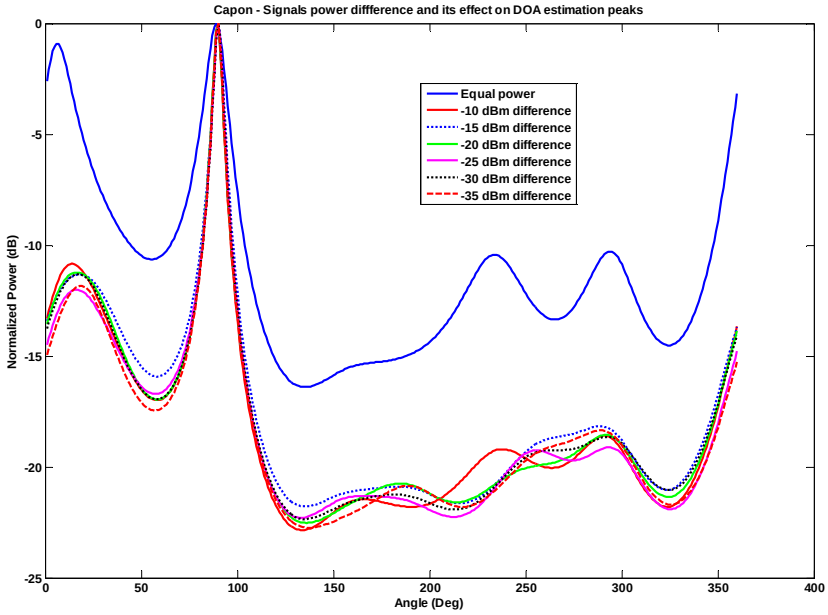

Figure 53 Estimated Spectrum for Capon for a varying power difference between the impinging sources

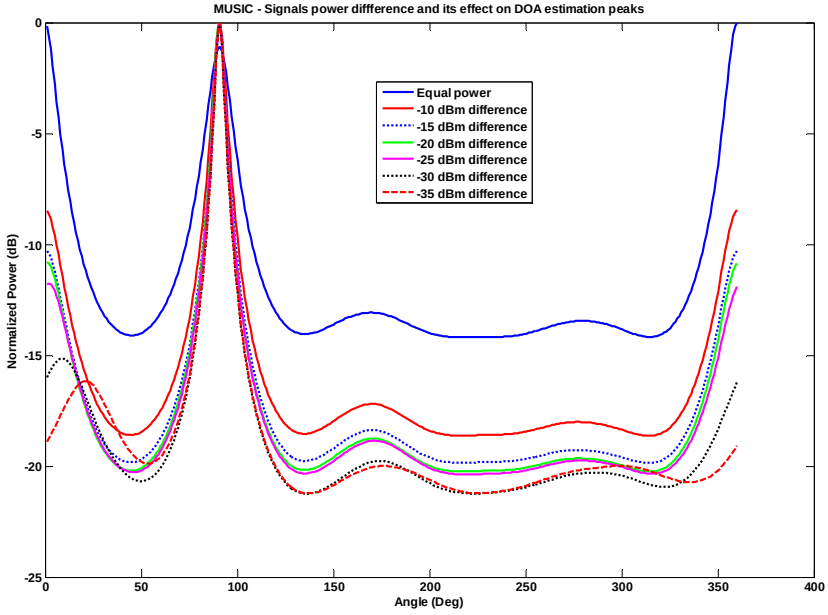

Figure 54 Estimated Spectrum for MUSIC for a varying power difference between the impinging sources

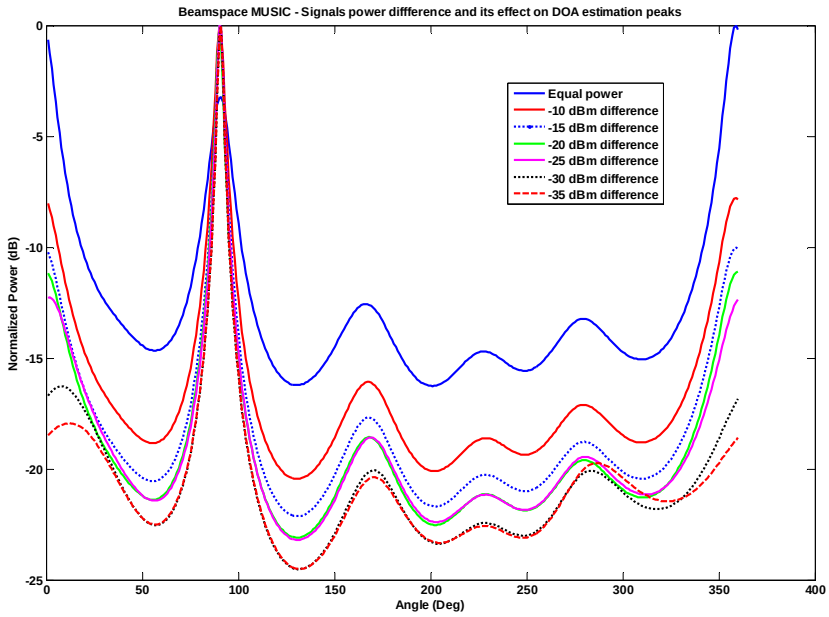

Figure 55 Estimated Spectrum for beamspace MUSIC for a varying power difference between the impinging sources

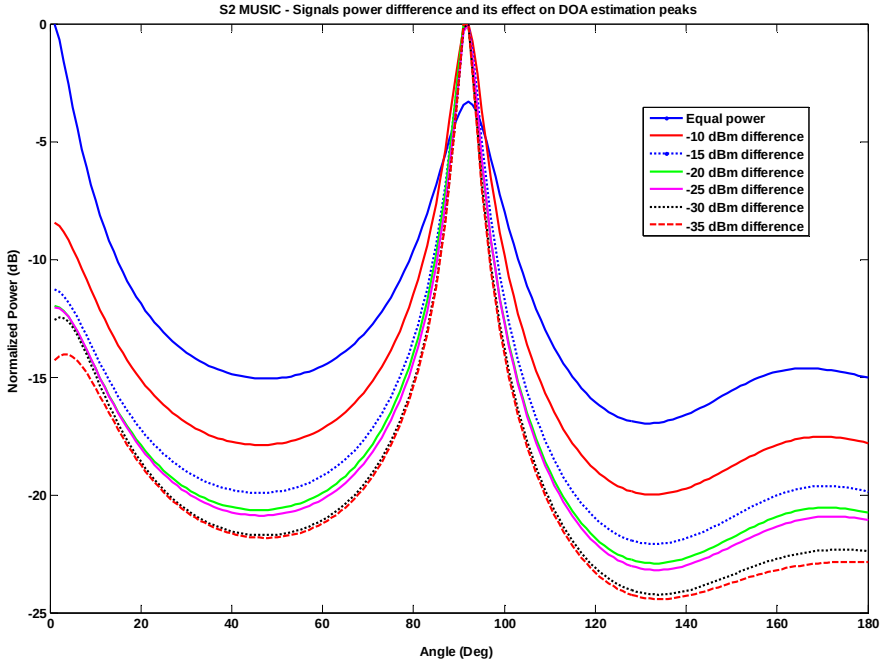

Figure 56 Estimated Spectrum for S2 MUSIC for a varying power difference between the impinging sources

Results are summarized in Table 9 for all the algorithms after mutual coupling compensation. The reader should note that the measurements shown are based on one set of measurements. To verify the consistency of the estimates, 10 sets of data for the same bearing were acquired and processed in the case were the two signals exhibited the same power. No notable changes were noted in the spectrum of all the algorithms, except for Capon, which showed a variation in the bearing estimate of the 1st peak of about 3 degrees along with a variation on the peak power of about 2dB. All the other algorithms showed no sign of variation over all data sets.

The parameters of interest are the 3 dB peak-width, the resulting power of the 1st and 2nd peaks, the 3rd highest peak and the bearing error. It is apparent that Bartlett and Capon perform poorly when the power difference between the two sources is 10 dB or higher. MUSIC, beamspace MUSIC and S2 MUSIC showed superb performance of bearing error. The beam corresponding to the peak with the lower power setting showed a significant widening. The 3rd highest peak compared to the second peak stayed about constant after the 10 dB difference mark for all algorithms except Bartlett, where the second peak became a mere sidelobe. Overall it was noticed that the 3dB peak-width increased slightly when two source measurements are conducted compared to a single source.

Table 9 Summary for data for all algorithms after mutual coupling compensation for two sources with varying power difference

Bartlett Sig. power difference (dB)	3 dB peak-width (degrees)		Power (dBm)		3rd highest peak (dBm)	Bearing error (degrees)	
	1st	2nd	1st	2nd		1st	2nd
0	46	44	0	-0.74	-5.9	0	0
-10	38	42	-5.5	0	-5.5	9	2
-15	34	42	-6.7	0	-6.7	12	2
-20	34	42	-7.2	0	-7.2	13	2
-25	34	42	-7.4	0	-7.4	13	2
-30	34	42	-7.4	0	-7.4	13	2
-35	34	42	-7.4	0	-7.4	13	2
Capon Sig. power difference	3 dB peak-width		Power		3rd highest peak	Bearing error	
	1st	2nd	1st	2nd		1st	2nd
0	14	8	-0.9	0	-10	5	0
-10	42	6	-10.8	0	-19	13	1
-15	42	6	-10.9	0	-18	13	1
-20	40	6	-11.3	0	-19	16	1
-25	45	6	-11.4	0	-18.5	16	1
-30	43	6	-11.8	0	-18.4	18	1
-35	58	6	-12	0	-18.2	16	1
MUSIC Sig. power difference	3 dB peak-width		Power		3rd highest peak	Bearing error	
	1st	2nd	1st	2nd		1st	2nd
0	10	8.5	0	-1.1	-13	1	2
-10	20	8	-8.5	0	-17	1	2
-15	20	7	-10.3	0	-18.4	1	2
-20	20	5.5	-10.6	0	-18.9	1	2
-25	20	4.5	-11.9	0	-18.9	1	2
-30	60	4.4	-15.2	0	-19.8	1	2
-35	90	5.5	-16.2	0	-20	1	2
Beamspace MUSIC Sig. power difference	3 dB peak-width		Power		3rd highest peak	Bearing error	
	1st	2nd	1st	2nd		1st	2nd
0	12	10	-0.9	0	-10	2	0
-10	18	3.5	-10.8	0	-19	1	1
-15	20	3.5	-10.9	0	-18	1	1
-20	22	2.5	-11.3	0	-19	1	1
-25	28	2.5	-11.4	0	-18.6	1	1
-30	24	2.5	-11.8	0	-18.4	1	1
-35	24	2.5	-12	0	-18.2	2	1
S2 MUSIC Sig. power difference	3 dB Beamwidth		Power		3rd highest peak	Bearing error	
	1st	2nd	1st	2nd		1st	2nd
0	9	12.5	0	-3.3	-14.6	0	3
-10	18	5	-8.4	0	-17.5	0	1
-15	20	8	-11.3	0	-19.6	0	1
-20	21	7.4	-16.1	0	-20.5	0	1
-25	21	7.5	-12.1	0	-20.6	0	1
-30	22	6.6	-12.5	0	-22.3	1.5	1
-35	29	6.6	-14	0	-22.8	3	1

The MUSIC algorithm is given as an example in Figure 57 to show how the algorithm behaves when phase calibration and mutual coupling compensation are applied

to the data vector for the varying power difference between the two sources. The spectra for the rest of the algorithms can be found in Appendix B (Two CW signals with varying power difference).

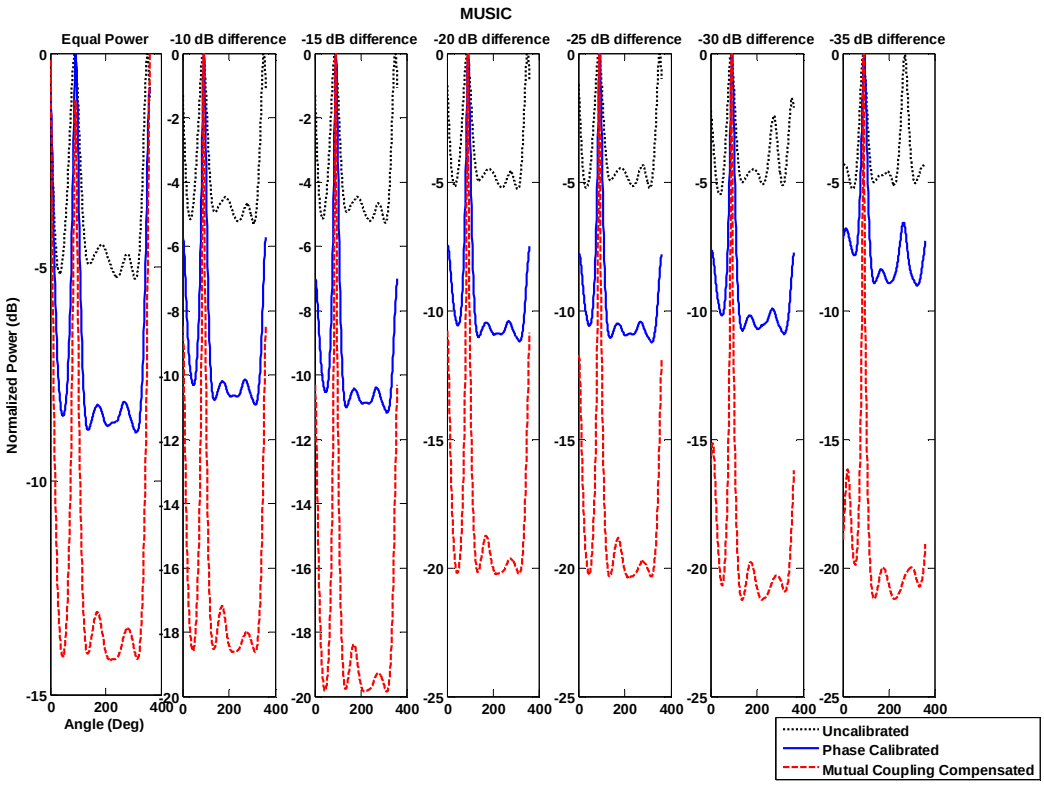

Figure 57 MUSIC algorithm estimated spectrum for different varying power difference in the uncalibrated, phase calibrated and mutual coupling compensated case

Harris SeaLancet RT1944/U Radio Signal

The Harris SeaLancet RT1944/U Radios were used to test the capability of the system to detect signals emitting from radios utilizing a wideband signal. Two units were used where one was set to be the master and the other to be the slave. The SNR was set to 25 dB and the transmit signal strength used was -10 dBm. A 50 dB attenuation was used between the two units. The transmission speed used was 10 MBPS and the

occupied bandwidth of the modulated signal was 20 MHz. The estimated spatial spectrum for all algorithms of interest are shown in Figure 58 while the 3dB beamwidth along with the main peak to the second highest peak and deviation peak are summarized in Table 10.

Results indicate that the accuracy of bearing estimates is very good overall showing a maximum deviation in MUSIC with 2 degrees of error. Compared to the results shown in Table 7, the accuracy in detecting a wideband signal source after mutual coupling compensation is within a dB of the true peak except for MUSIC where the error was 2 degrees. In addition, the ratio of the main peak to the second highest peaks is higher compared to CW results, along with a noticeable widening of the 3dB beamwidth. The first factor leading to the latter is attributable to behavior of the high resolution algorithms, which assume a narrow band signal while the signal used here is not. In addition, the SNR used in this case was 25dB compared to 34 dB in the CW case. Another important factor is related to the fact that only a portion of the WiMAX signal (5% of the overall signal is passed) is used since the maximum sampling rate allowed by the data acquisition system is 2.5 MSPS.

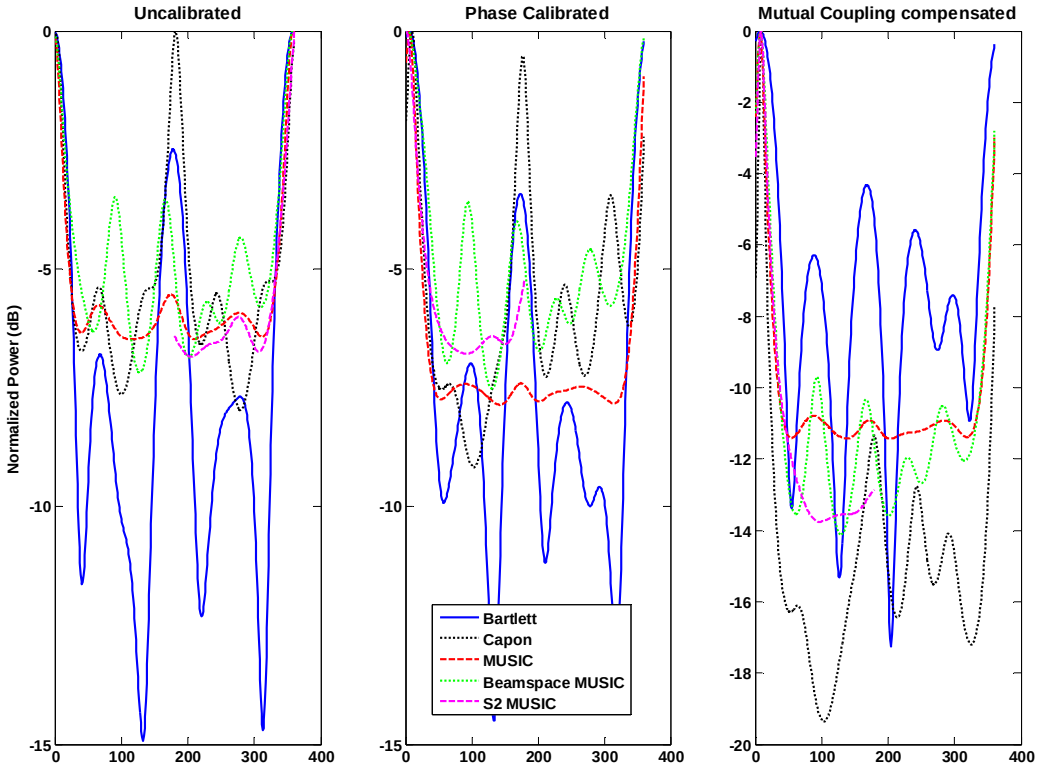

Figure 58 Estimated Spatial spectrum for DOA estimation algorithms when a WiMAX signal is used. Uncalibrated (Left), Phase Calibrated (center), and Mutual coupling Compensated (right)

Table 10 Algorithms performance when a WiMAX signal is used

	3dB peak-width (Degrees)			Main peak to the second highest ratio (dB) (mean of the highest second peak)			Deviation from true peak. (Degrees)		
	Before cal	After center cal	Mutual coupling com	Before cal	After center cal	Mutual coupling com	Before cal	After center cal	Mutual coupling com
Bartlett	44	45	44	2.5	3.4	4.3	9	6	0
Capon	24	23.5	9.2	0	0.5	11.2	6	2	1
MUSIC	34.5	24	16	5.5	7.4	11	10	6	2
Beamspace MUSIC	42	54	18.7	3.5	3.5	9.5	10	4	0
S2-MUSIC	31	23.5	14	6	6.5	13.5	8	7	1

Effect of Signal Frequency on the DOA Estimate

As mentioned in Chapter five, the frequency response of the filters in the 8-channel receiver board varies from one channel to the other and above 500 KHz the phase is not consistent. The goal in this section is to quantify how this variation of phase over the IF band affects the estimated DOA. For the same bearing, the LO drive frequency was varied to produce an output of 100 KHz to 1.2 MHz in 100 KHz increments. Only the data that was mutual coupling compensated is shown in this section and is depicted in Figure 59. Relying on phase calibration alone beyond the point of phase consistency causes a significant deviation from the true peak, but based on the results from mutual coupling compensated data the estimates are still accurate to within 4 degrees when the IF frequency is below the 3dB point of the filter response. At 1.2 MHz we see that all the algorithms fail to yield accurate results and that is not only due to the filter but also one should note that at the highest frequency, the sampling is at the Nyquist threshold. One way to minimize the accuracy error in this case is to build a filter that extends beyond the desired IF pass frequency but just high enough to exhibit stable phase within the desired IF band.

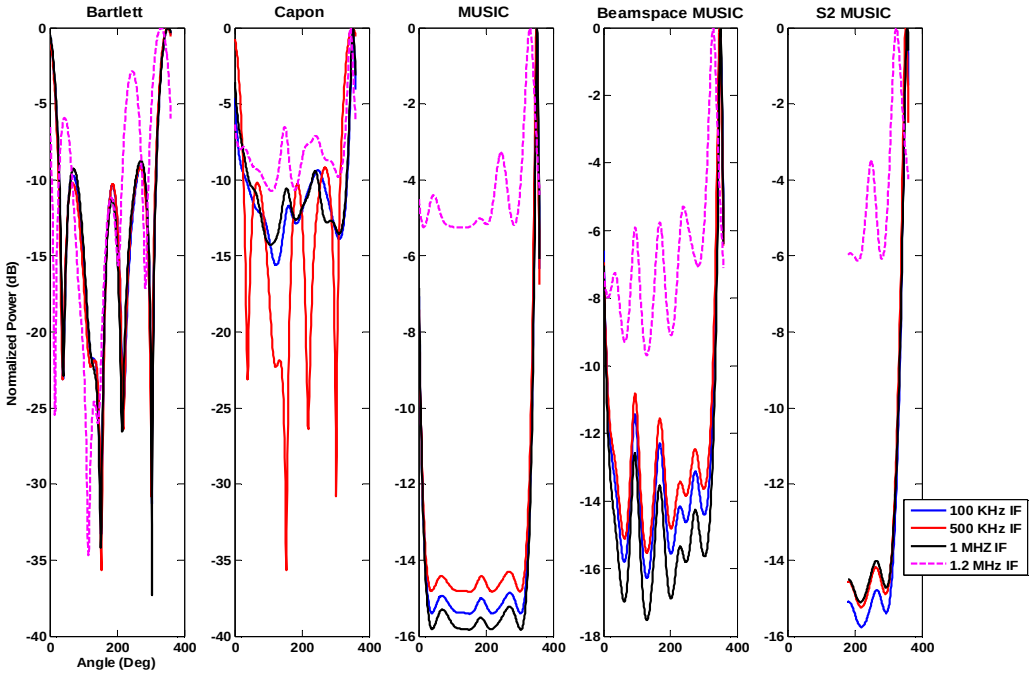

Figure 59 Effect of IF frequency on DOA estimates

Table 11 Deviation (degrees) from actual bearing for a varying IF frequency

	500 KHz	600 KHz	700 KHz	800 KHz	900 KHz	1000 KHz	1100 KHz	1200 KHz
Bartlett	1	2	4	5	1	1	4	20
Capon	1	2	4	5	1	1	4	20
MUSIC	1	1	4	1	1	1	1	4
Beamspace MUSIC	3	4	8	1	0	0	6	23
S2 MUSIC	1	2	10	3	5	5	3	27

Close Frequency vs. Number of Samples

Since the algorithms used assume non-coherent signals, finding how spectrally close signals affect the DOA estimates is crucial. Two CW sources were used and were set to be 2 KHz apart. The number of samples used was also varied from 50, 100, to 1000 samples a fixed bearing. The calibrated, uncalibrated and mutual coupling

compensated estimated spectrum for Bartlett, Capon, MUSIC, beamspace MUSIC, and S2 MUSIC for different number of samples are depicted in Figure 60, Figure 61, Figure 62, Figure 63, and Figure 64, respectively. From close inspections of the figures, it is quite clear that when a small number of samples is used the spatial spectrum estimate is distorted even when mutual coupling compensation is used, especially for S2 MUSIC. Compared to spectrally spaced sources, the results shown in this section which are summarized in Table 12 indicate an increase in bearing error, especially for S2 MUSIC. The data shown in Table 12 was averaged over 20 runs. It is concluded here, that for spectrally close sources a larger number of sample is required to achieve high resolution DOA estimates.

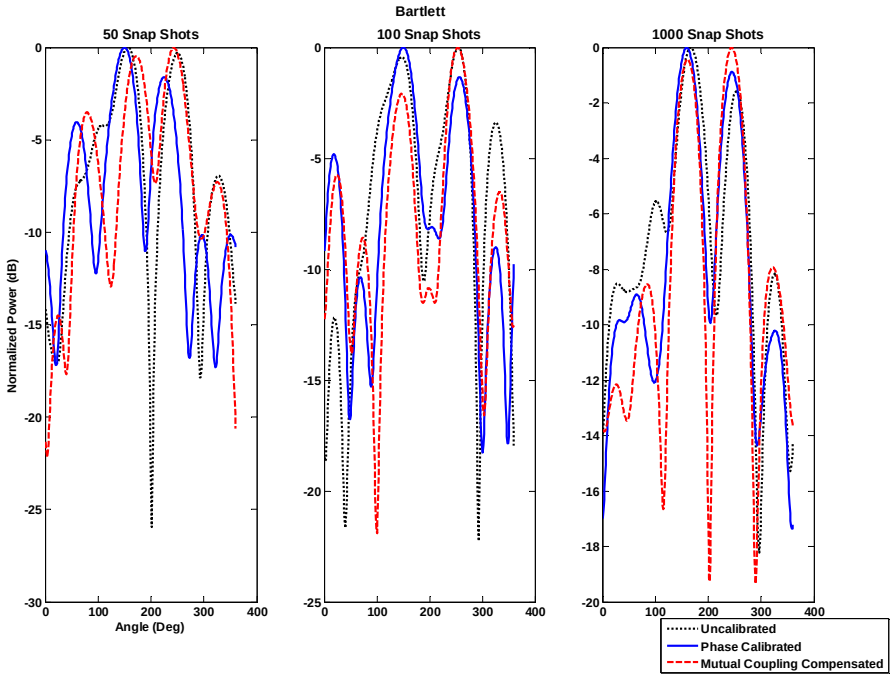

Figure 60 Effect of spectrally close sources and limited number of samples on Bartlett DOA estimates

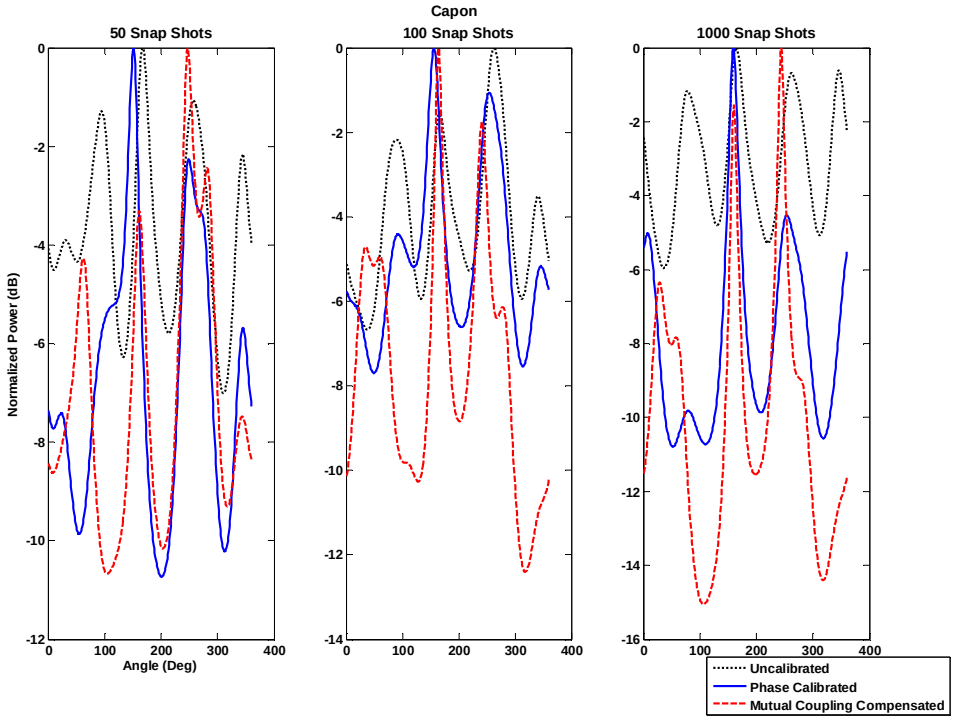

Figure 61 Effect of spectrally close sources and limited number of samples on Capon DOA estimates

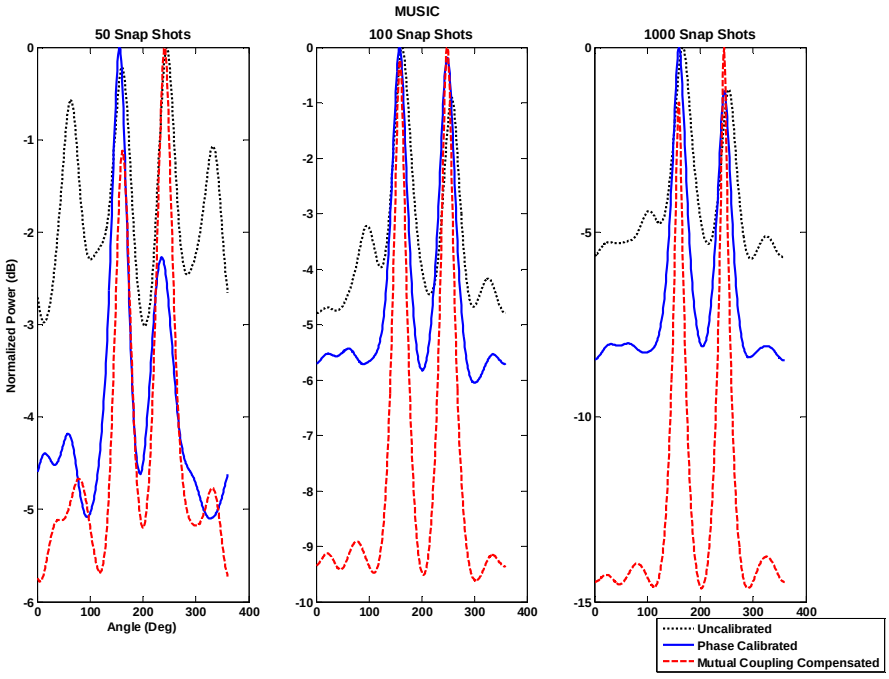

Figure 62 Effect of spectrally close sources and limited number of samples on MUSIC DOA estimates

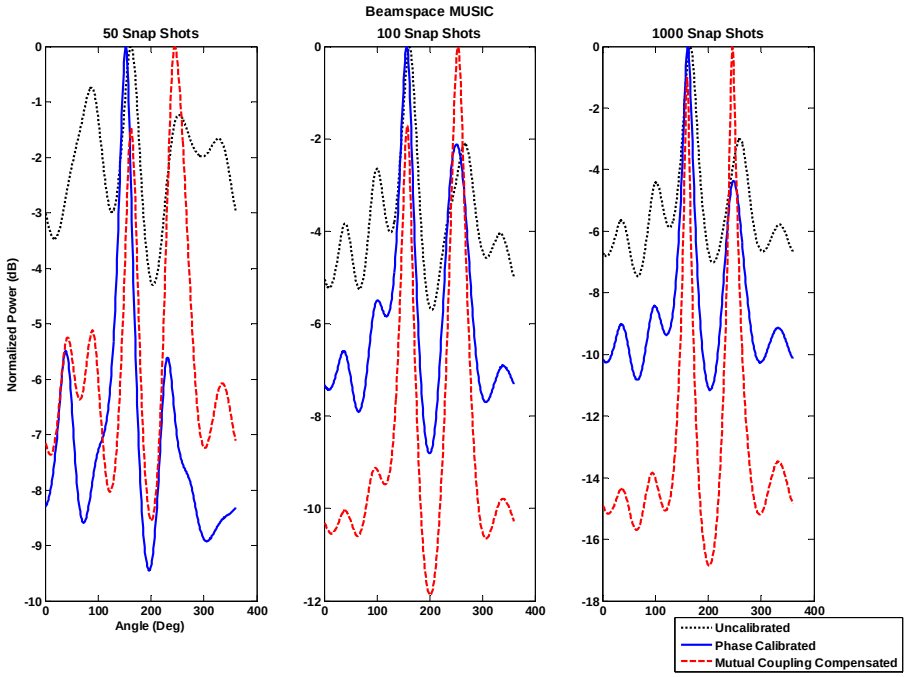

Figure 63 Effect of spectrally close sources and limited number of samples on beamspace MUSIC DOA estimates

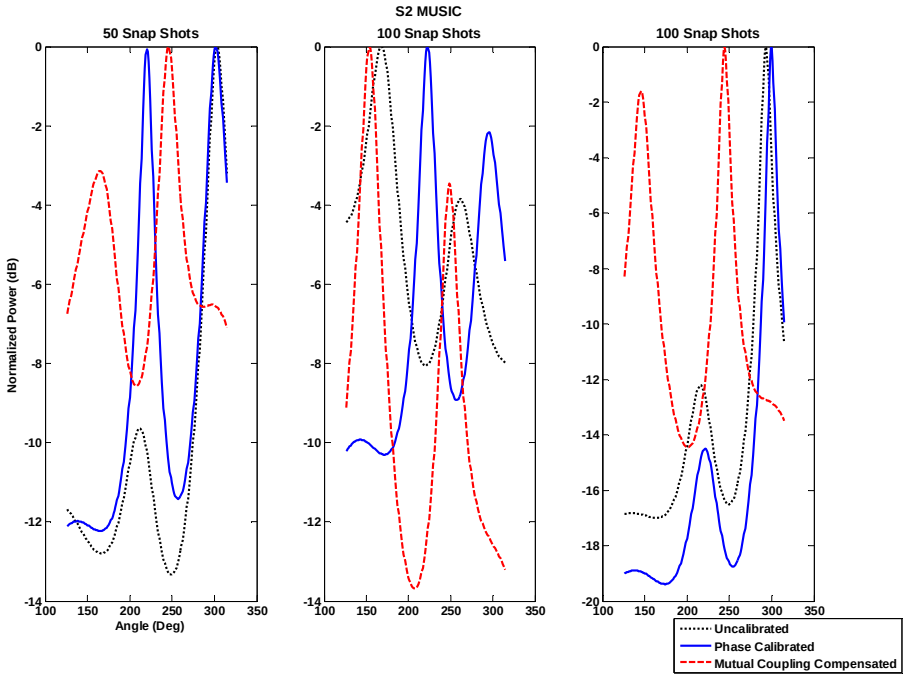

Figure 64 Effect of spectrally close sources and limited number of samples on S2 MUSIC DOA estimates

Table 12 1st and 2nd peak deviation from the true bearing for a varying number of samples used

	1st Peak mean deviation (degrees)			2nd Peak mean deviation (degrees)		
	50	100	1000	50	100	1000
Bartlett (no Cal)	30.2381	20.5714	7.5714	30.6667	21.1429	9.7143
Bartlett (phase Cal)	20	13.6190	4.3810	35.4286	15.7619	5.1905
Bartlett (MC comp)	62.3810	57.0476	0.9524	62.4762	56.3810	0
Capon(no Cal)	43.8095	86.5238	38.0952	45.9048	84.1429	79.0952
Capon(phase Cal)	10.9524	15.1905	0.4762	119.0476	133.5714	134.4286
Capon(MC comp)	43.8095	49.1429	0.3333	45.9048	56.9048	0.7143
MUSIC(no Cal)	63.7619	28.0476	7.1429	64	41.8095	9.9524
MUSIC(phase Cal)	16.5714	11.6190	4.1429	30.6190	10.5714	6.5238
MUSIC(MC comp)	64	47.6667	1	63.7619	47.7143	0.1905
Beamspace MUSIC(no Cal)	8.1429	92.9048	6.5714	139.5714	6.1905	24.9048
Beamspace MUSIC(phase Cal)	4.9048	5.0952	2	51	25.0952	3.8571
Beamspace MUSIC	56.1905	64.0476	0.5714	57.2381	61.7143	2.0476
S2 MUSIC(no Cal)	44.1429	140.9048	1.3333	134.9524	32.5238	161.7143
S2 MUSIC(phase Cal)	33.1429	139.3333	11.6667	140.5238	31.1429	151.8095
S2 MUSIC(MC comp)	No peak	No peak	6	86.6190	86.7619	16

Summary of Results

In this Chapter the results for a variety of experiments that were carried out was shown. Both a single and dual CW sources were tested along with a WiMAX signal. The results show that mitigating the mutual coupling effects is imperative to achieving high resolution performance. Compared to a single source case, when multiple sources are used, a beam widening along with a slightly higher error in accuracy was recorded when the two sources exhibit the same power. When the power difference is significant, Bartlett and Capon performed poorly while the high resolution algorithms yielded superb performance in estimating the angles of arrival.

When the Harris radios were used to test with a WiMAX signal, though the accuracy of estimating the bearings for all the algorithms was excellent, the 3dB beamwidth and the ratio of the main peak to the second highest peak were poorer than when a CW signal was used. The reasons for the observed degradation are that in the

experiment a lower SNR was used compared to the CW case, in addition to the fact that the signal used is not narrow band. Finally, only a portion of the available channel bandwidth was used which means that only a fraction of the signal power is captured, this will affects the performance of DOA estimation algorithms.

When the 1MHz channel was utilized, the IF frequency was varied to verify the performance of the algorithms under varying IF frequency. It was concluded that with mutual coupling compensation the algorithms performed well beyond the 3dB point of the filters and failed to perform only when the sampling rate was at the threshold of the Nyquist criterion. Signal coherence effects were examined by using two sources that were set to be 2 KHz apart. It was concluded using a lower number of sample degrades the performance of the algorithms significantly when the sources are spectrally close (2KHz).

The above results show how well the spectral algorithms perform in a lab setting. With the current lab setting, resolution could not be tested properly since the chamber is not big enough to have a small angular source separation without having the two antennas interfere with one another. Future lab equipment will allow more accurate testing without having to approximate the angle of arrival based on a blind algorithms. Having knowledge of the exact angle when conducting a test not only helps to provide a more accurate metric on the algorithms performance but will enable improvement in the calibration method.

CHAPTER SIX

CONCLUSION AND FUTURE WORK

The goal to equip the smart antenna system at Montana State University with a high resolution and computationally efficient DOA estimation algorithm was met. The challenges in implementing high resolution DOA estimation algorithms in a real system at 5.8 GHz have been addressed in this research. Conventional and subspace based spectral DOA estimation algorithms have been analyzed and a novel computationally efficient alternative was presented. Though more susceptible than MUSIC to certain parameter variations (SNR, mutual coupling…), the error in S2 MUSIC is not significant enough to result in major accuracy or resolution degradation according to simulation results. The major drawback of S2 MUSIC is that it can detect fewer sources then conventional MUSIC since S2 MUSIC relies on reducing the size of the covariance matrix.

Lab tests showed that S2 MUSIC has remarkable performance compared to MUSIC. In addition, S2 MUSIC, due to its reduced search space, is not subject to sidelobes which is the case for other algorithms. A significant amount of time and effort was necessary to implement the hardware needed to achieve our goal. Phase stability was a major concern and the hardware designed showed good phase stability thanks to the mechanical rigidity provided by the designed enclosure. Test results showed that the receiver board is able to successfully estimate bearings of sources that are as low as -90 dBm. When the receiver board was subject to strong signals, the front end saturation did not affect the DOA estimates. When multiple sources were tested, the

high resolution spectral algorithms showed a remarkable ability to estimate sources even if the power difference between them is in excess of 35 dB and the maximum deviation of 3 degrees from the actual bearing was measured when S2 MUSIC was used (power difference between the two sources was 35dB). Over all, the accuracy of the high resolution spectral subspace based DOA estimation algorithms was within 2 degrees of the actual bearing.

Good hardware design was necessary but not sufficient to reach theoretical performance; mitigating unwanted effects inherent in the hardware was necessary as well. Calibrating for magnitude and phase errors in the system by means of current injection improved the DOA estimates compared to the case where no calibration was applied. The accuracy of estimation was improved significantly. Without calibration the estimates were up to 14 degrees from the actual bearing (in the case of MUSIC). After the current injection calibration was applied the deviation from the true peak was within a fraction of a degree. In addition, the 3dB peak-width improved from 46 degrees to about 20 degree after applying the current injection calibration. Mitigating the effect of mutual coupling proved to be the key step in approaching theoretical performance. The results showed that the 3dB peak-width went from about 45 degree to about 4 degree after applying the new calibration method.

The offline calibration method showed very encouraging results. The method corrects not only for mutual coupling, but also for phase differences, which eliminates the need to perform current injection. Knowledge of the exact bearings of the sources used

for calibration is not required for this method, though having that information saves on the computation burden.

To the knowledge of the author, this is the first time such performance for high resolution DOA estimation algorithms was achieved in a real world scenario with such promising results. Most of the work done, especially at 5.8GHz, relied on simulation predictions and many experts in the field agreed that though theoretically subspace based methods are superior, their predicted performance is extremely hard to achieve since they are prone to the errors inherent in the system.

Though a significant amount of work was done to test the performance of the system, more work remains and the following summarizes some of the key future tasks:

- Test the system with a lab set up able to provide accurate bearings (this set up is currently considered for purchase by our group). This will further validate the results presented.
- Test the system in an outdoor environment to investigate how the system will perform outside the lab; the outdoor test will also allow for further testing of multi-sources.
- Incorporate the DOA block in the adaptive smart antenna system (this is currently being pursued and will be achieved shortly).
- Investigate alternative calibration methods or modify the current offline method to provide the system with the ability to self-calibrate.
- Future designs should consider a single board implementation for both DOA estimation and beamforming.

- Tracking was not considered in this work and investigating tracking algorithms is highly desirable.

REFERENCES CITED

[1] Dr. Yikun Huang (PI), Dr. Richard S. Wolff (CO-PI) “Smart Adaptive Antennas for Wireless Communications in Rural and Sparsely Populated Areas” proposed and accepted by MBRCT

[2] B. Allen, M. Ghavami “Adaptive antenna systems: fundamentals and applications” 2005, Wiley

[3] Godara, L.C. “Applications of antenna arrays to mobile communications. I. Performance improvement, feasibility, and system considerations” Proceedings of the IEEE, Vol 85 Issue 7

[4] T. S. Rappaport, “Wireless personal communications: Trends and challenges,” IEEE Antennas Propagat. Mag., vol. 33, pp. 19-29, Oct. 1991

[5] Khallaayoun, A., and Huang, Y., “Spatial Selective MUSIC for Direction of Arrival Estimation with Uniform Circular Array”, IEEE Antennas and Propagation Society Annual Symposium, July 2007.

[6] P. Stoica and A. Nehorai, “MUSIC, Maximum Likelihood, and Cramer-Rao bound”. IEEE Trans. Acoust. Speech Signal Processing **37** (1989), pp. 720–741.

[7] M. D. Panique “Design and evaluation of test bed software for a smart antenna system supporting wireless communication in rural areas”, Master’s Thesis, Montana State University, May, 2005

[8] B. D. V. Veen, K. M. Buckley, “Beamforming: A Versatile Approach to Spatial filtering”, IEEE ASSP Magazine, April 1988

[9] Y. Huang R.Wolff, “A Compact Smart Antenna for WiMAX Radio”, IEEE mobile WiMAX, July 2009, Napa California

[10] Raymond J. Weber, “Development of a Cognitive Array System” , Master’s Thesis, Montana State University, May, 2010

[11] Huang, Y., and Panique, M., “Performance analysis of a nullsteering algorithm,” IEEE APS International Symposium, June, 2007.

[12] C. GODARA, “Applications of Antenna Arrays to Mobile Communications, Part I: Performance Improvement, Feasibility, and System Considerations” PROCEEDINGS OF THE IEEE, VOL. 85, NO. 7, JULY 1997

[13] Constantine A.Balanis (1997), “Antenna theory”, Wiley, third edition

[14] P. Ioannides, C.A. Balanis, “Uniform circular arrays for smart antennas” Antennas and Propagation Magazine, IEEE Aug 2005, vol 47 Issue 4

[15] Louis L. Schart “Statistical signal processing: detection, estimation, and time series analysis”.Addision-Wesley Publishing company, 1991

[16] A. L. Swindlehurst and T. Kailath, “A performance analysis of subspace-based methods in the presence of model errors. Part I: The MUSIC algorithm,” IEEE Trans. Signal Process., vol. 40, no. 7, pp. 1758–1774, July 1992

[17] Bellini, E. and Tosi, A. “A directive system of wireless telegraphy”, 1906, Elect. Eng. 2 (11), pp. 771-775.

[18] Marconi, G. “On Methods Whereby the Radiation of Electric Waves May be Mainly Confined to Certain Directions, and Whereby the Receptivity of a Receiver May be Restricted to Electric Waves Emanating from Certain Directions”, Proceedings of the Royal Society of London. Series A, Containing Papers of a Mathematical and Physical Character, April 30, 1906, Vol. 77, No. 518, pp. 413-421.

[19] Adcock, F. British Patent Specification No.130490 1919.

[20] 3. Keen, R. Wireless detection finding. s.l. : Iliffe & Sons, Dorset House.

[21] Bartlett, M. S, “Periodogram Analysis and Continuous Spectra," Biometrika 37 (1950), 1-16

[22] H. Krim, M. Viberg. Two decades of array signal processing research: the parametric approach . s.l. : Signal Processing Magazine, IEEE , Vol 13, Issue 4., Jul 1996.

[23] Burg, J.P. , “Maximum entropy spectral analysis”, 1967, Proc. 37th annual meeting of the society of exploration geophysicists.

[24] J. Capon “High-Resolution Frequency-Wavenumber Spectrum Analysis” PROCEEDINGS OF THE IEEE, VOL. 57, NO. 8, AUGUST 1969

[25] Borgiotti, G.V. and Kaplan, L.J. , “Superresolution of uncorrelated interference sources by using adaptive array techniques” 1979, trans. Antennas Propag. AP-27, p. 842.

[26] Gabriel, W. , “Spectral alalysis and adaptive array superresolution thecniques”, 1980, Proc. IEEE 68, p. 654.

[27] Paulraj, A ,“Subspace methods for direction of arrival”, et al. 1993, Amsterdam: North-Holland, 1993, Vol 10 Chap 16 , pp. 693-739.

[28] Pisarenko, V.F. “The retrieval of harmonics from a covariance function” 1973, Geophys.J.Roy. Astronom. Soc. 33 , pp. 347-366.

[29] Ralph O. Schmidt, “Multiple Emitter Location and Signal Parameter Estimation” IEEE transactions on antennas and propagation, vol. AP-34, NO.3, march 1986.

[30] Schmidt, R.O. “A signal subspace approach to multiple emitter location of spectral estimation”, PhD Thesis, Stanford University, 1981.

[31] Bienvenu, G. and Kopp, L. , “Principe de la goniometrie passive adaptative” 1979, 7° Colloque sur le traitement du signal et des images, FRA, pp. 1-10.

[32] Tufts, D.W. and Kumaresan, R. ,“Estimation of frequencies if multiple sinusoids: making linear prediction perfrom like maximum likelihood”, September 1982, Proc. of IEEE 70, 9, pp. 975-989.

[33] Kumaresan, R. and Tufts, D.W. Estimating the angle of arrival of multiple plane waves. Jan 1983, IEEE tran. on Aerospace and Elec. Sys.AES-19 , pp. 134-139

[34] Owsley, N. L. “Signal Subspace based minimum variances spatial array processing”, November 1985, 19th Asilomar Conf., pp. 94-97.

[35] Xu, X. L. and Buckley, k. M. “A comparison of element and beamspace spatial-spectrum estimation for multiple source clusters”, April 1990, Proc. ICASSP-90 , pp. 2643-2646.

[36] Paulraj, A. and Roy, R.H. , “Estimation of signal parameters via rotational invariance techniques-ESPRIT”, November 1985, In Proceedings of the 19tj Asilomar Conference on circuits systems and Computers, pp. 83-89.

[37] Roy, R.H. “ESPRIT--Estimation of signal parameters via rotational invariance techniques”, 1987, Ph.D dissertation, Stanford University.

[38] Kung, S. Y., Arun, K. S. and Bhashkar Roa, D.V. “New state space and singular value decomposition based approximation methods for harmonic retreival”, 1983, Journal of the optical society of America 73, pp. 1799-1811.

[39] Ouibrahim, H., Weiner, D. D. and Sarkar, T. K. “Matrix pencil approach to angle of arrival estimation”,November 1986, In Proceedings of the 20th Asilomar Conf. on Circuits systems and Computers, pp. 203-206.

[40] C. P. Mathews and M. D. Zoltowski, “Eigenstructure techniques for 2-d angle estimation with uniform circular arrays,” IEEE Trans. on Signal Processing, vol. 42, pp. 2395-2407, Sept. 1994

[41] A.H. Tewfik, W. Hong, “ On the application of uniform linear array bearing estimation techniques to uniform circular arrays”, IEEE Trans. Signal Processing, Vol 40, pp. 1008-1011, Apr. 1992

[42] B. Friedlander, A. J. Weiss, “Direction finding using spatial smoothing with interpolated arrays”, IEEE Trans. Aerosp. Electron. Syst., Vol 28, pp. 574-587, Apr. 1992

[43] Barabell, A. J. “Performance comparison of superresolution array processing algorithms”. s.l. : Lincon Labratory, MIT, Tech. Rep. TST-72 1984.

[44] A. J. Barabell, “Improving the resolution performance of eigenstructure-based direction finding algorithms ” IEEE ICASSP, 1983, Boston

[45] A. N. Lemma, E. F. Deprettere, A.-J van der Veen “Experimental Analysis of Antenna Coupling for High-Resolution DOA Estimation Algorithms” IEEE 1999

APPENDICES

APPENDIX A

HARDWARE SCHEMATICS, LAYOUT, AND BOM

Beamformer Board diagram

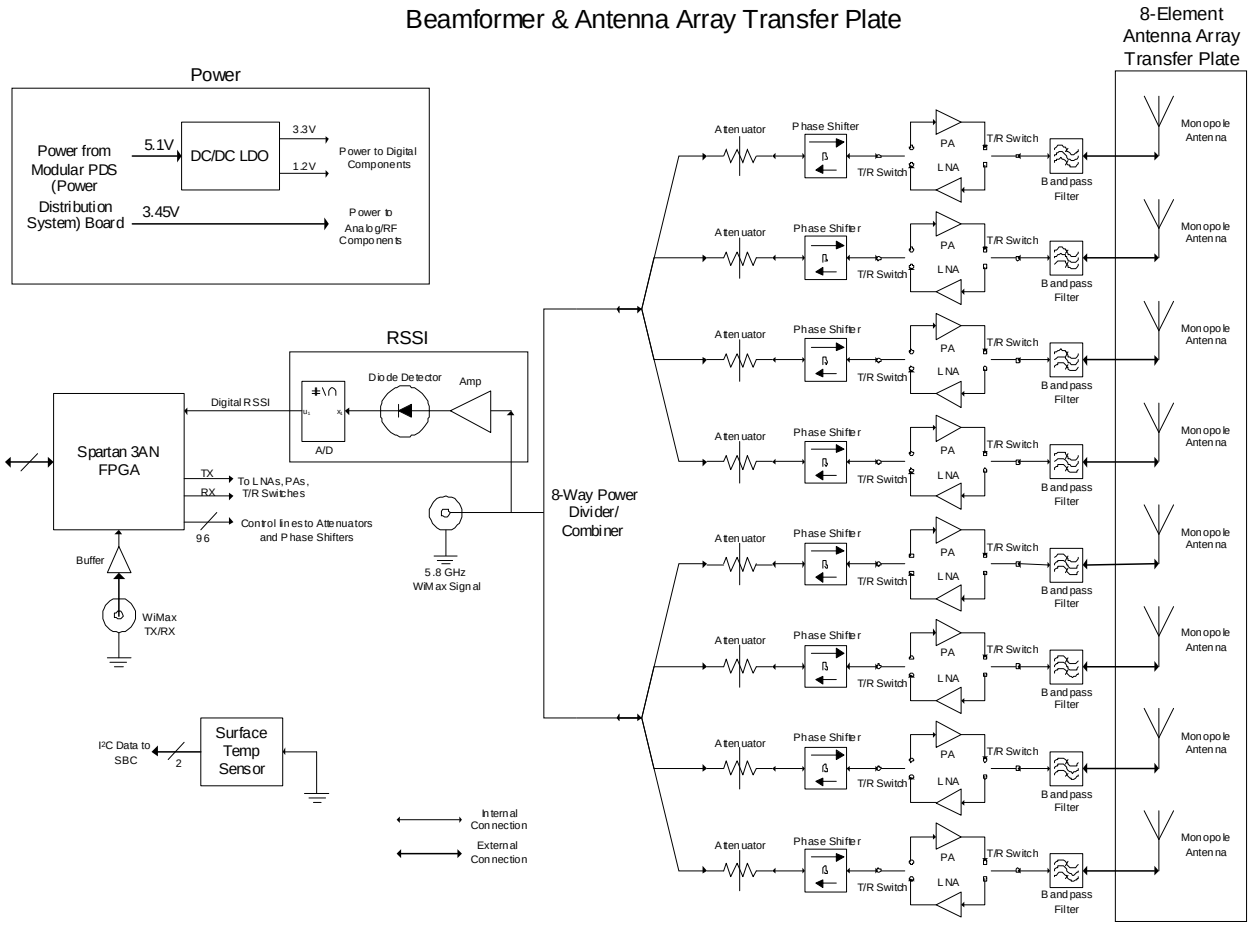

RF Front end -1

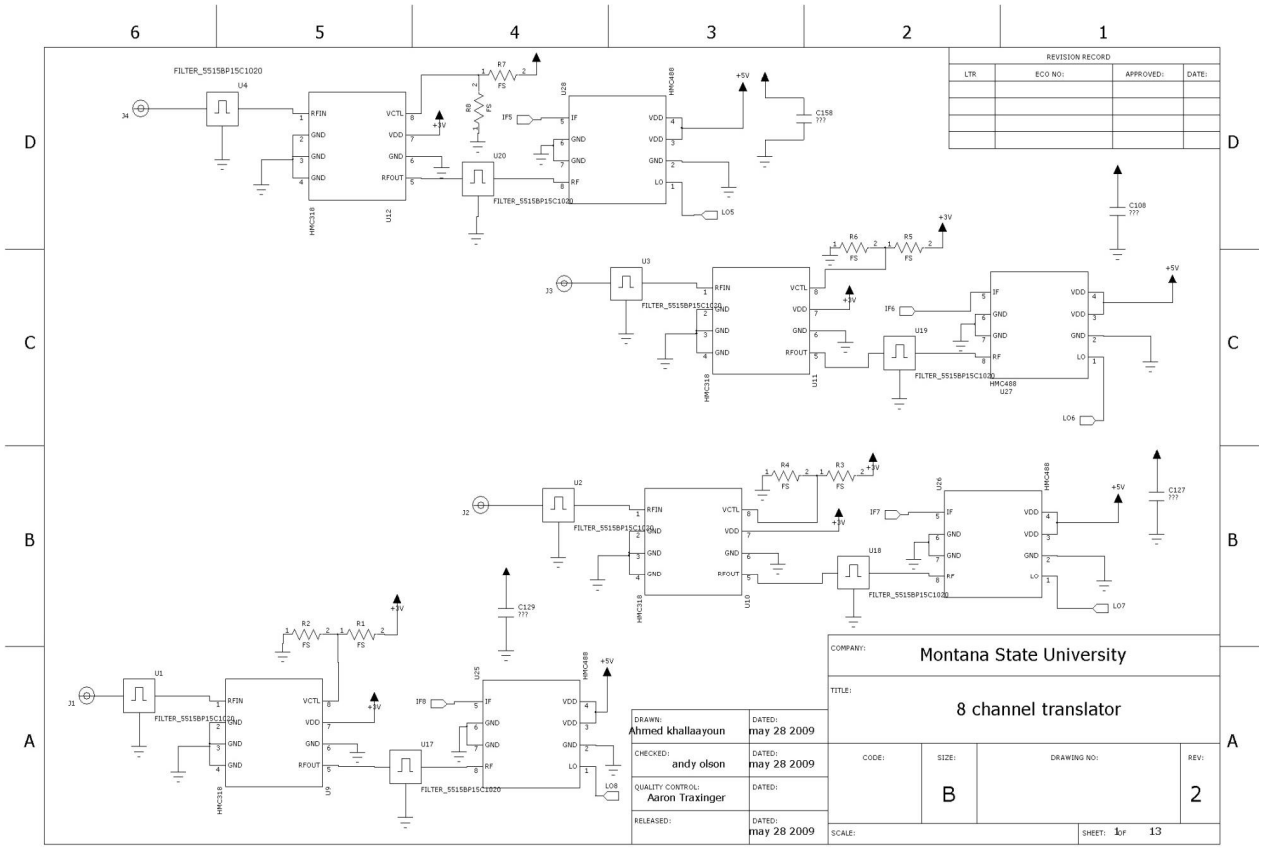

RF Front end -2

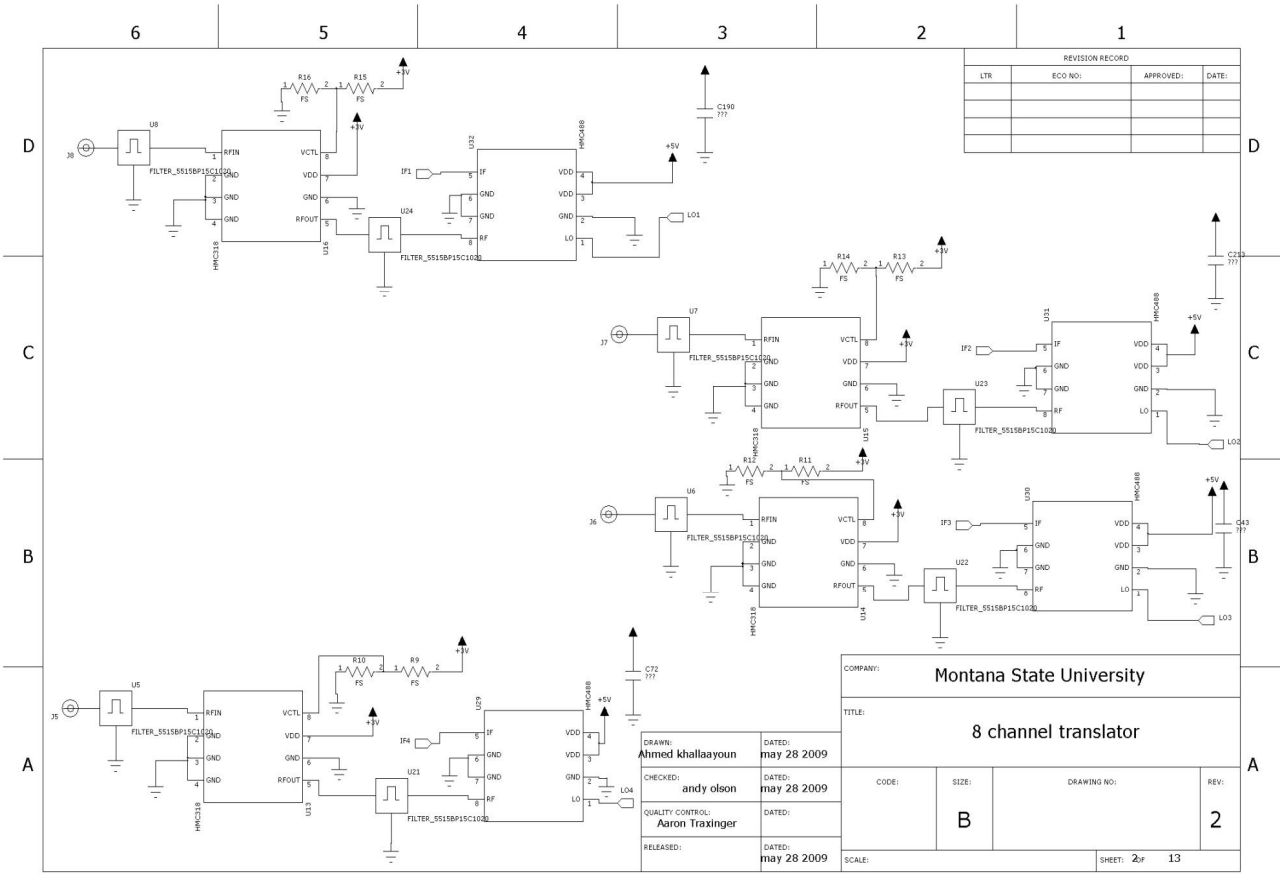

LO drive distribution-1

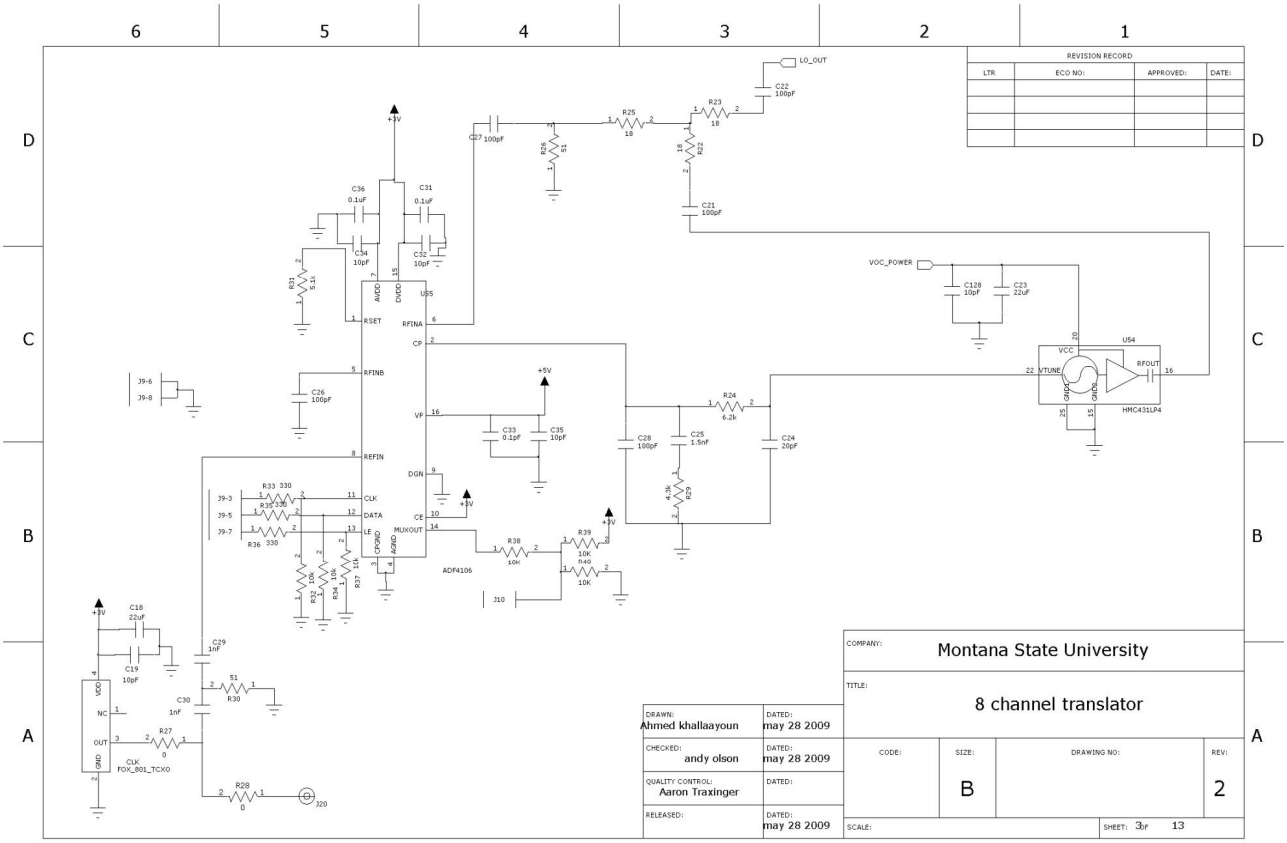

LO drive distribution-2

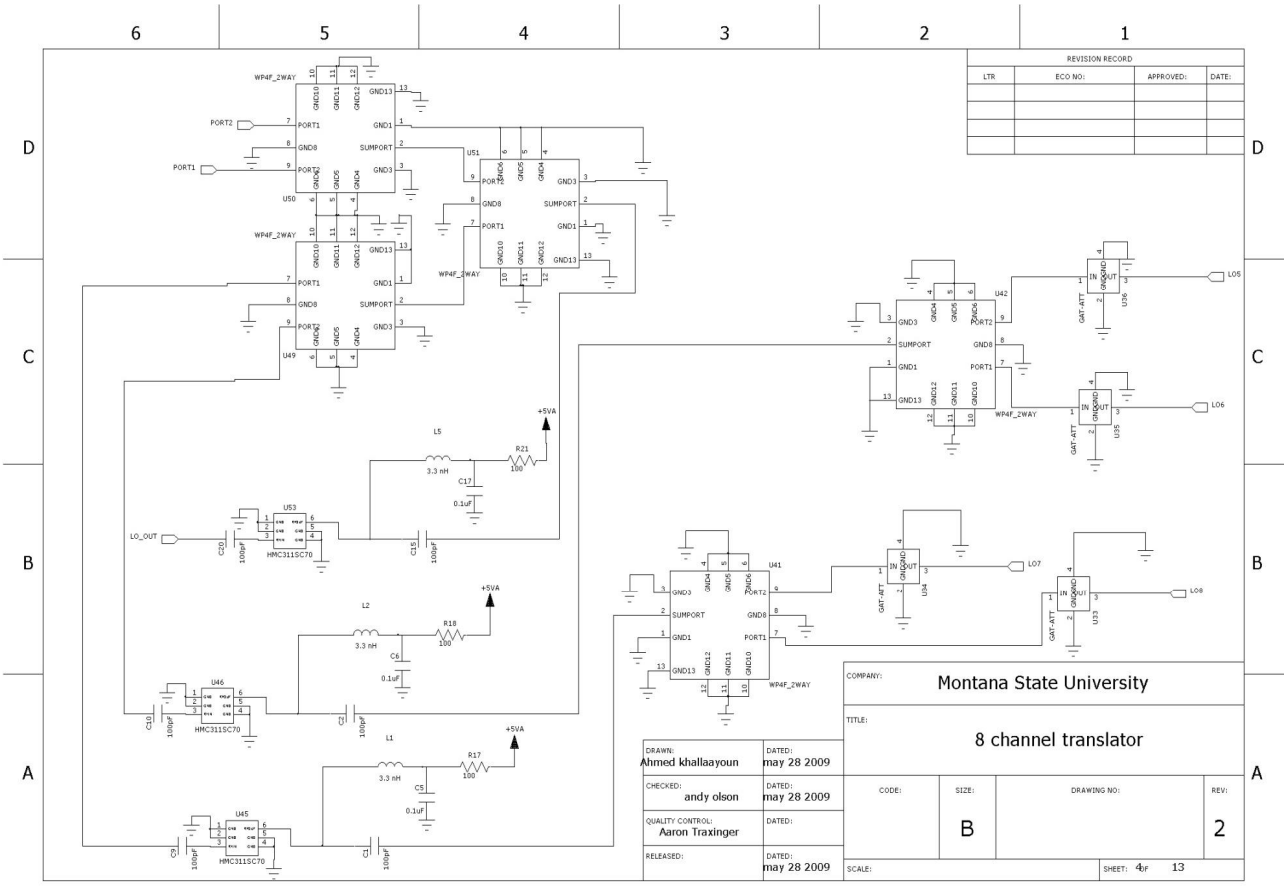

LO drive distribution-3

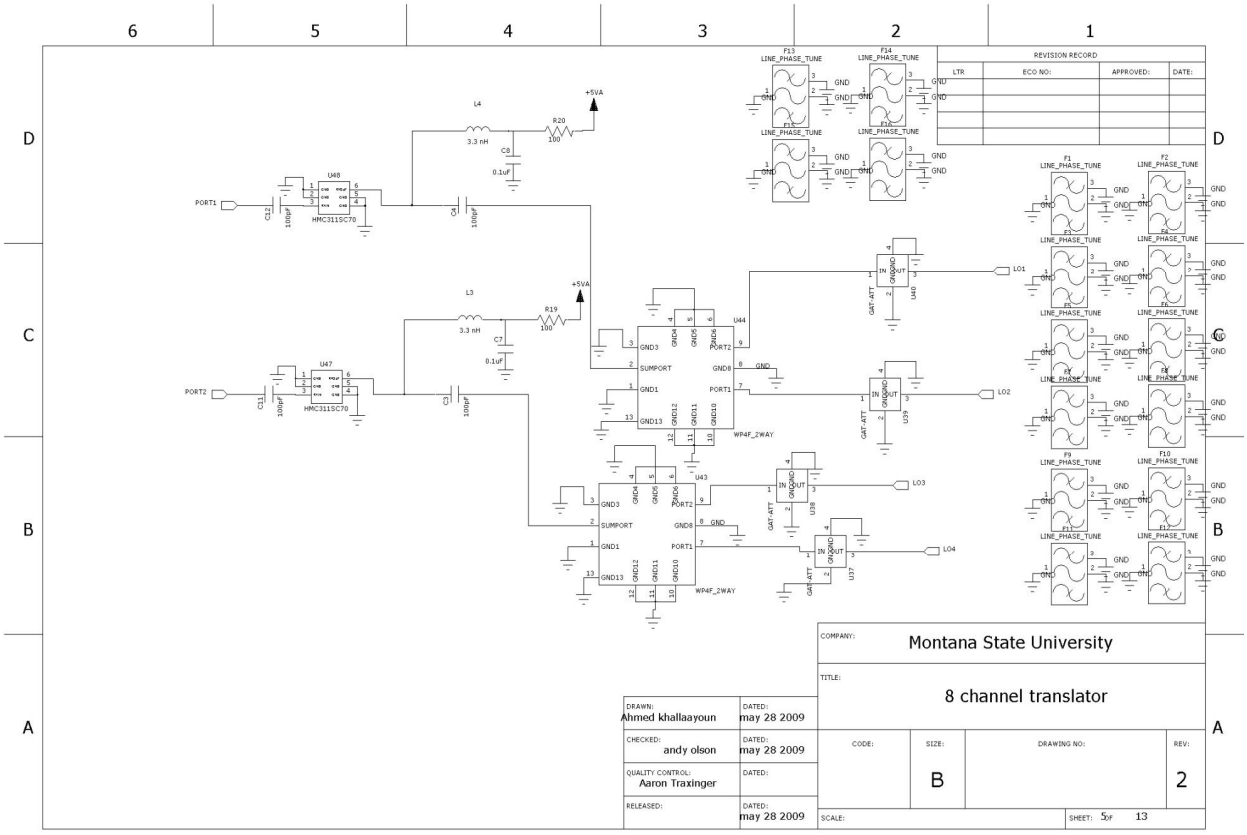

Power Supply

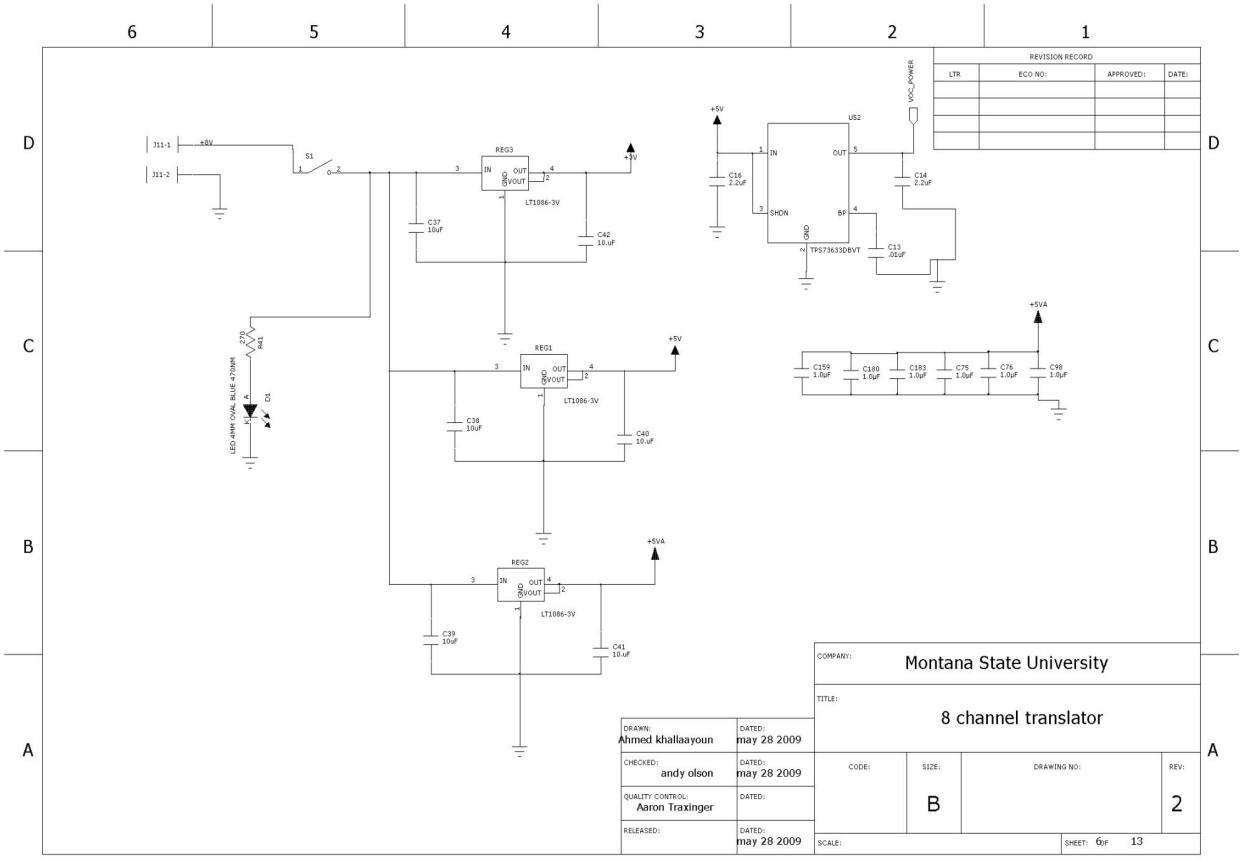

Variable Gain amplifier-1

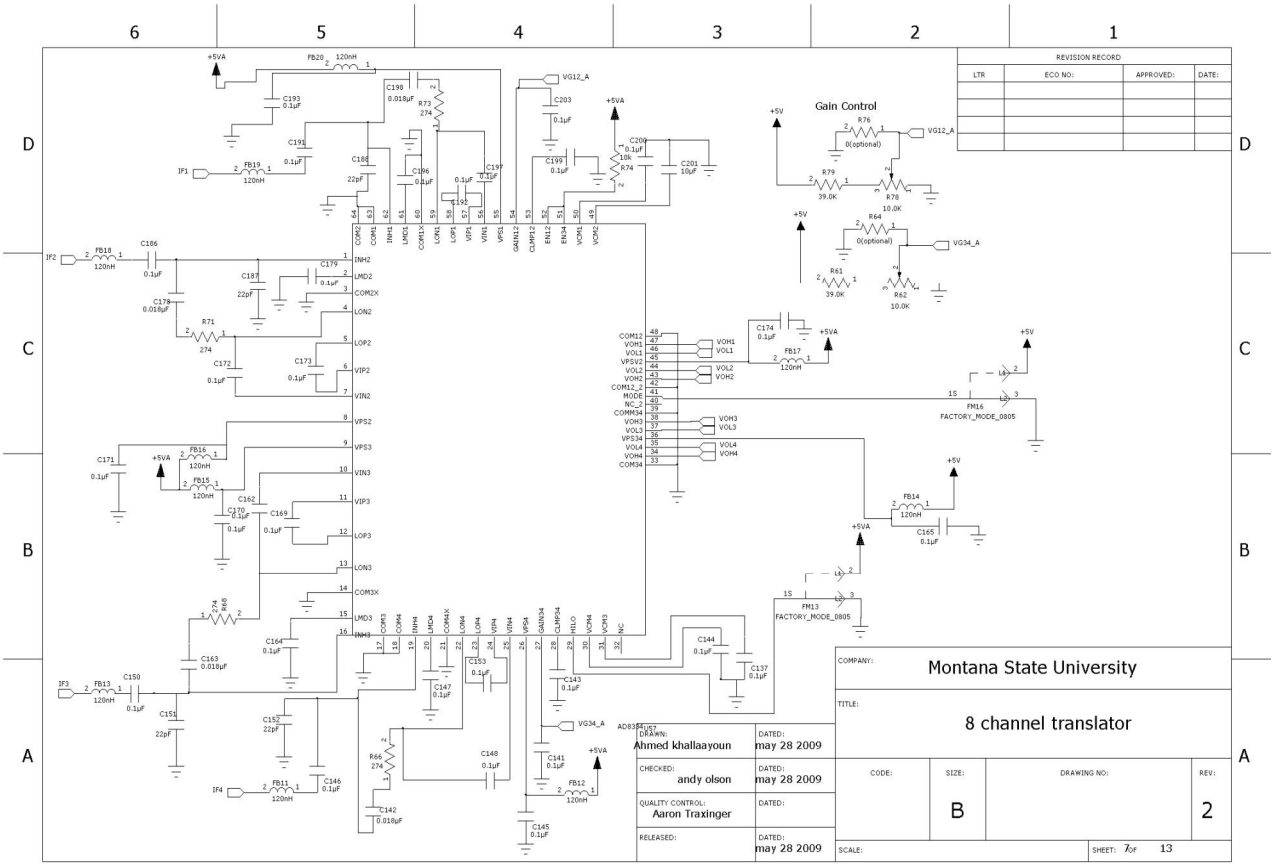

Variable Gain amplifier-2

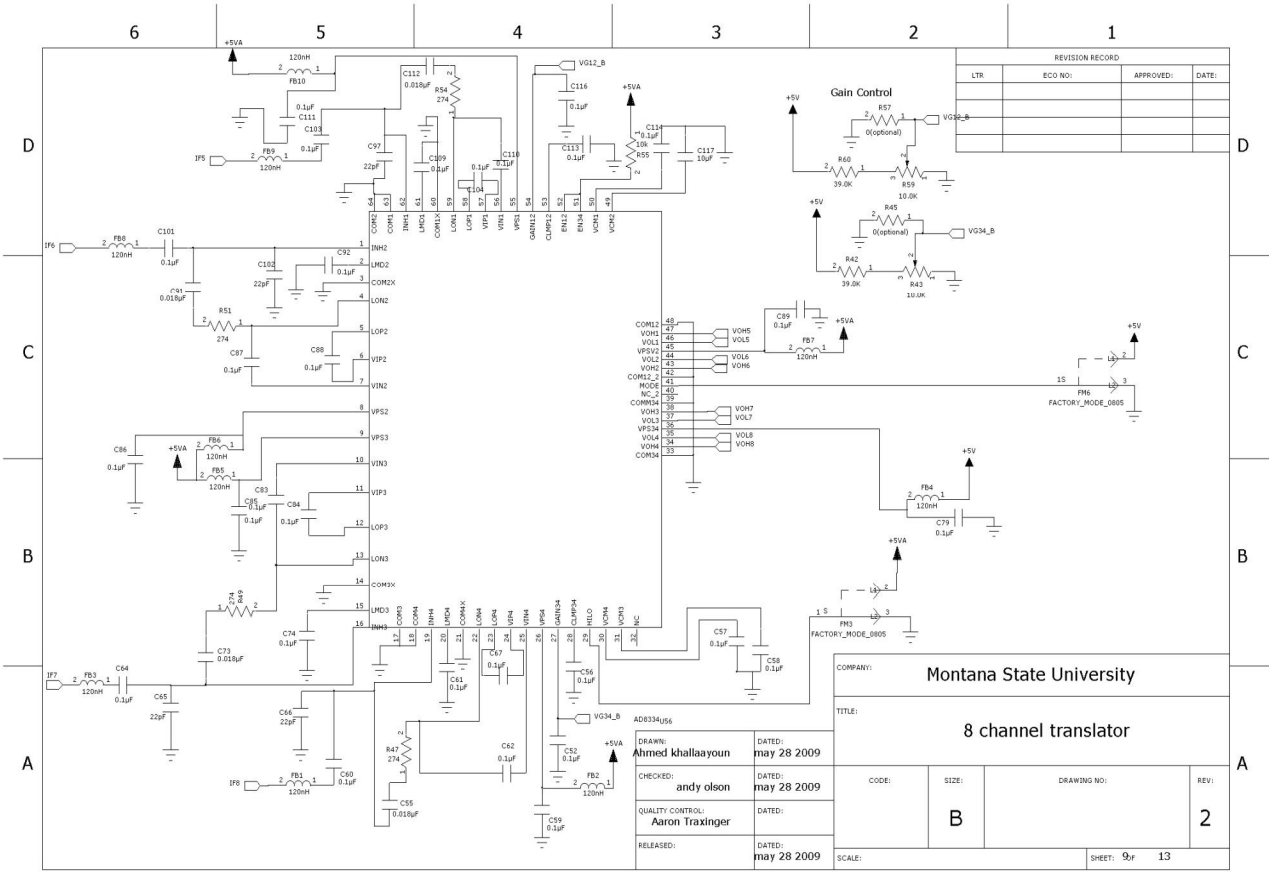

Variable Gain amplifier output -1

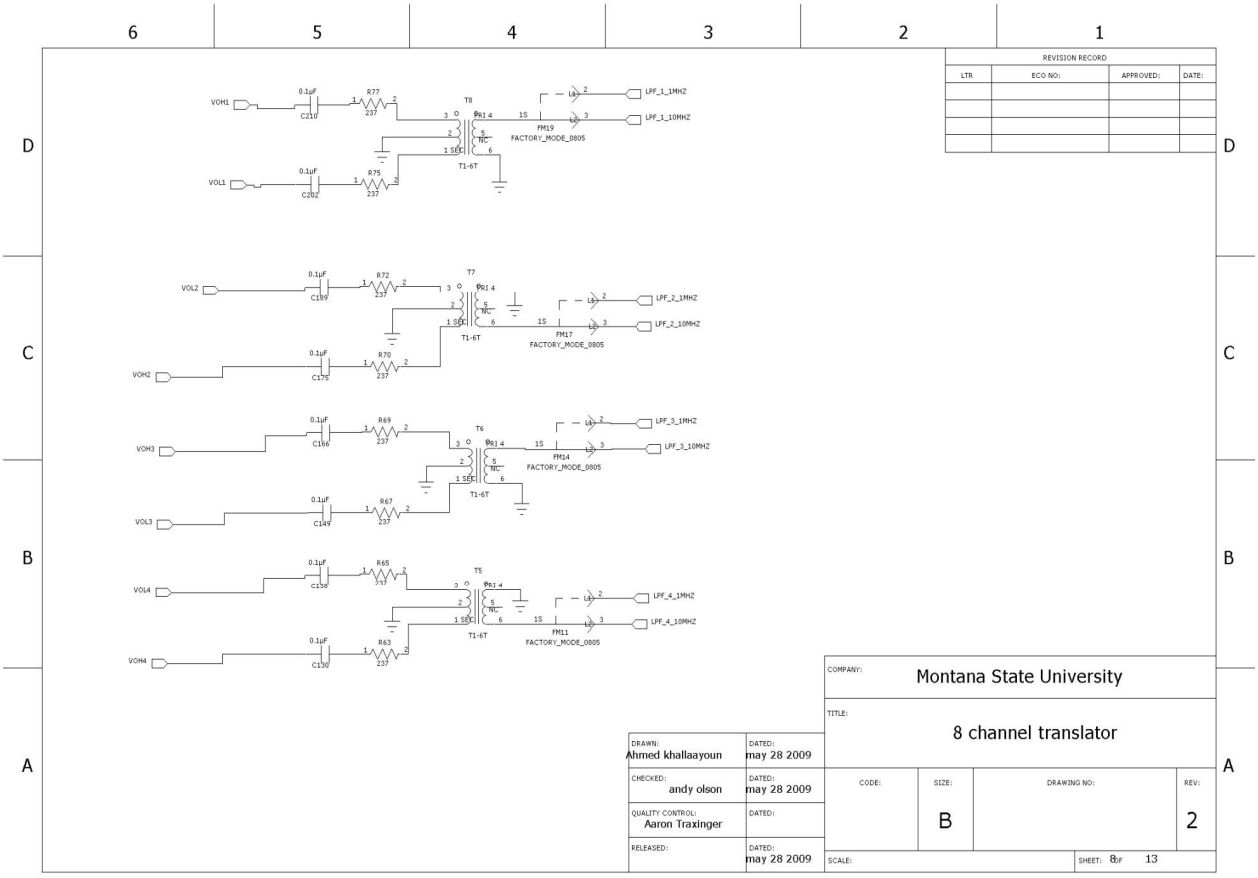

Variable Gain amplifier output -2

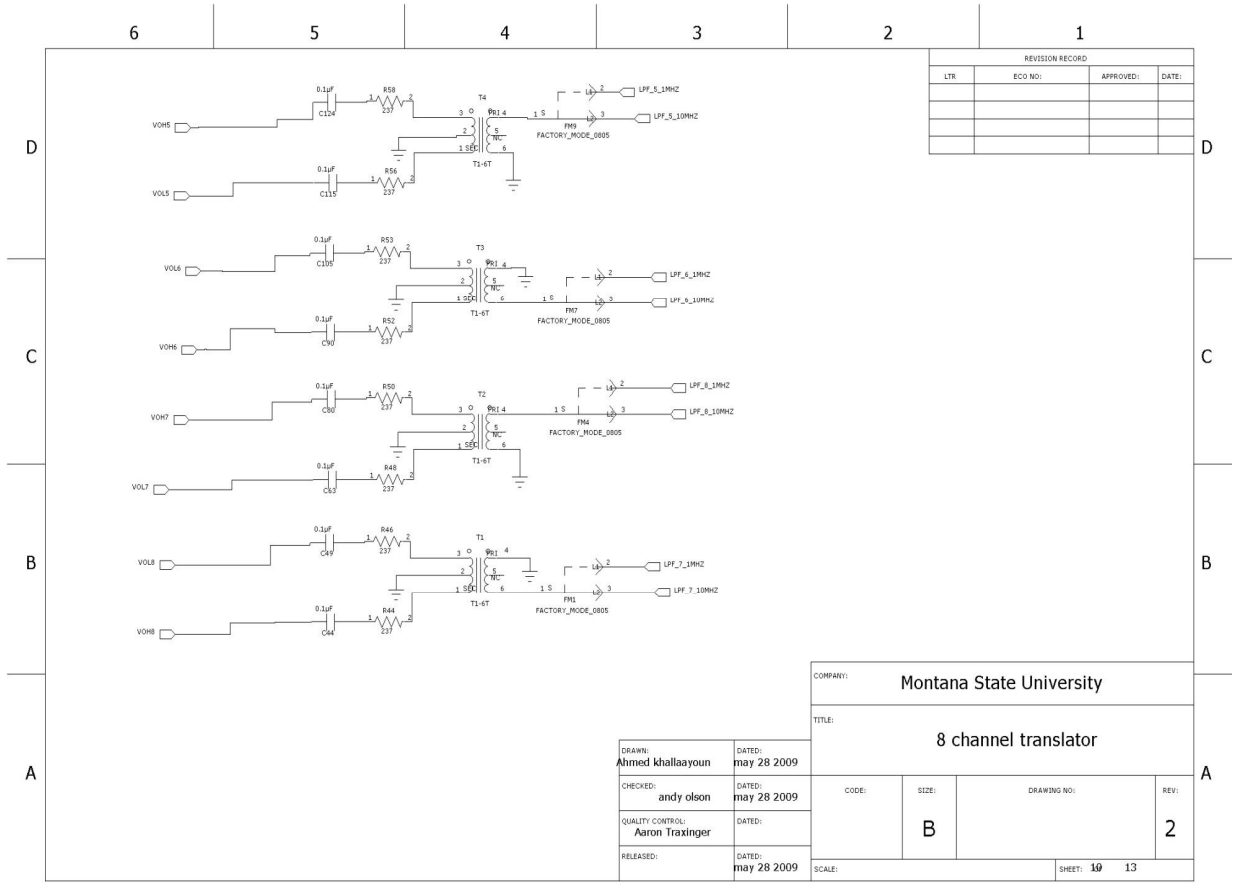

IF filters-1

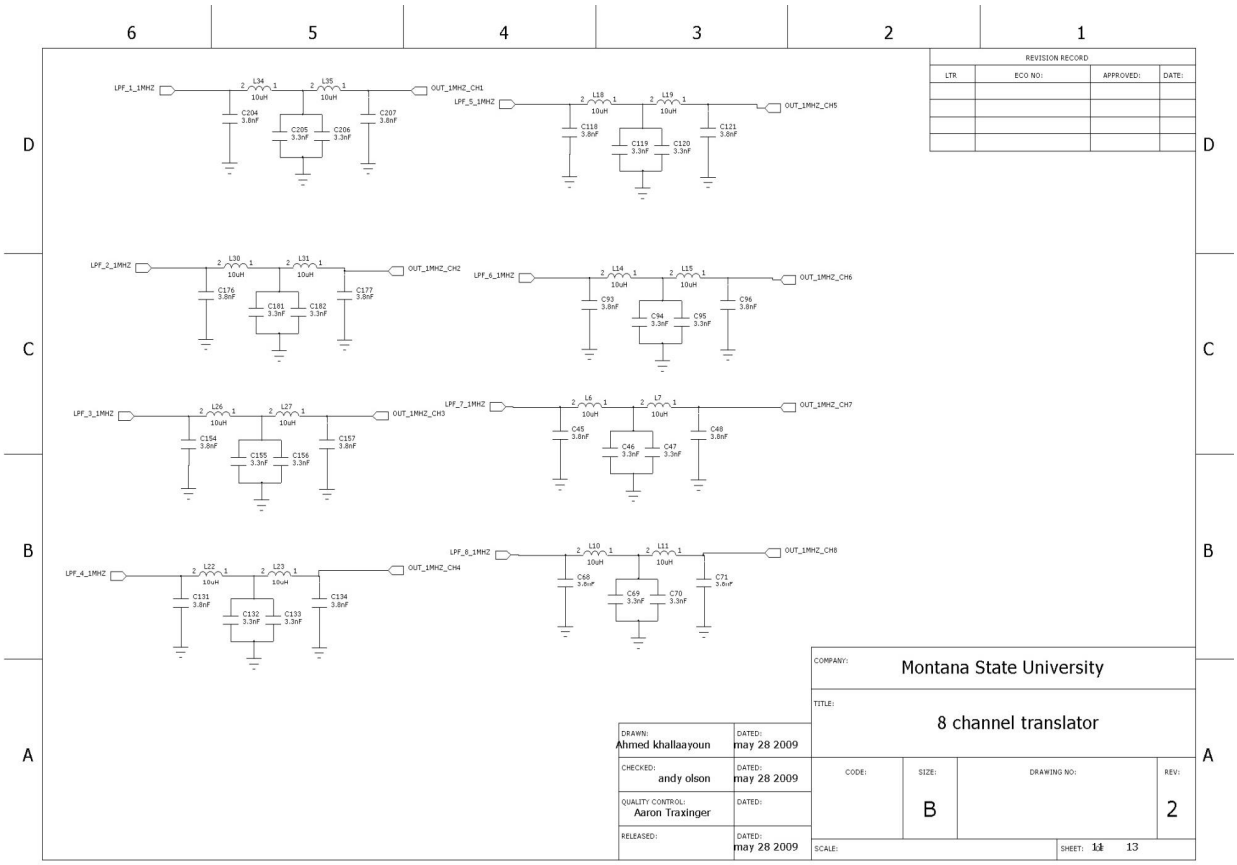
6
5
4
3
2
1
D
C
B
A
REVISION RECORD
LTR
ECO NO:
APPROVED:
DATE:
LPF_1_1MHZ
L34
10uH
L35
10uH
C204
3.8nF
C205
3.3nF
C206
3.3nF
C207
3.8nF
OUT_1MHZ_CH1
LPF_5_1MHZ
L18
10uH
L19
10uH
C118
3.8nF
C119
3.3nF
C120
3.3nF
C121
3.8nF
OUT_1MHZ_CH5
LPF_2_1MHZ
L30
10uH
L31
10uH
C176
3.8nF
C181
3.3nF
C182
3.3nF
C177
3.8nF
OUT_1MHZ_CH2
LPF_6_1MHZ
L14
10uH
L15
10uH
C93
3.8nF
C94
3.3nF
C95
3.3nF
C96
3.8nF
OUT_1MHZ_CH6
LPF_3_1MHZ
L26
10uH
L27
10uH
C154
3.8nF
C155
3.3nF
C156
3.3nF
C157
3.8nF
OUT_1MHZ_CH3
LPF_7_1MHZ
L6
10uH
L7
10uH
C45
3.8nF
C46
3.3nF
C47
3.3nF
C48
3.8nF
OUT_1MHZ_CH7
LPF_4_1MHZ
L22
10uH
L23
10uH
C131
3.8nF
C132
3.3nF
C133
3.3nF
C134
3.8nF
OUT_1MHZ_CH4
LPF_8_1MHZ
L10
10uH
L11
10uH
C68
3.8nF
C69
3.3nF
C70
3.3nF
C71
3.8nF
OUT_1MHZ_CH8
COMPANY:
Montana State University
TITLE:
8 channel translator
DRAWN:
Ahmed khallaayoun
DATED:
may 28 2009
CHECKED:
andy olson
DATED:
may 28 2009
QUALITY CONTROL:
Aaron Traxinger
DATED:
RELEASED:
DATED:
may 28 2009
CODE:
SIZE:
B
DRAWING NO:
REV:
2
SCALE:
SHEET: 13

IF filters-2

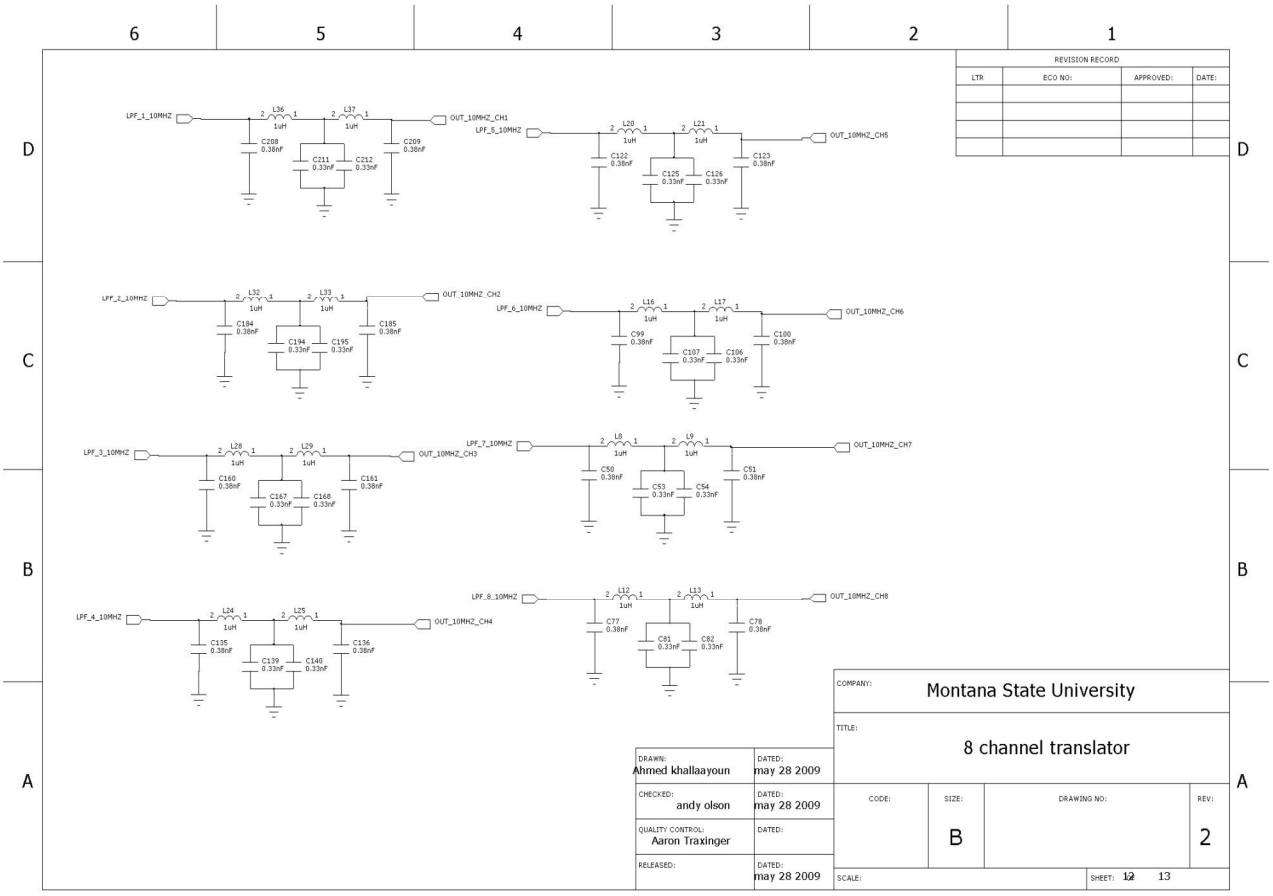
REVISION RECORD
LTR
ECO NO:
APPROVED:
DATE:
LPF_1_10MHZ
OUT_10MHZ_CH1
LPF_5_10MHZ
OUT_10MHZ_CH5
LPF_2_10MHZ
OUT_10MHZ_CH2
LPF_6_10MHZ
OUT_10MHZ_CH6
LPF_3_10MHZ
OUT_10MHZ_CH3
LPF_7_10MHZ
OUT_10MHZ_CH7
LPF_4_10MHZ
OUT_10MHZ_CH4
LPF_8_10MHZ
OUT_10MHZ_CH8
COMPANY: Montana State University
TITLE: 8 channel translator
DRAWN: Ahmed khallaayoun
DATED: may 28 2009
CHECKED: andy olson
DATED: may 28 2009
QUALITY CONTROL: Aaron Traxinger
DATED:
RELEASED:
DATED: may 28 2009
CODE:
SIZE: B
DRAWING NO:
REV: 2
SCALE:
SHEET: 12 13

Top Layer layout snapshot (RF layer)

C:\Ahmed_files\art001.pho (Board layer 1) Scale=1.43 Tue Mar 16 16:08:19 2010

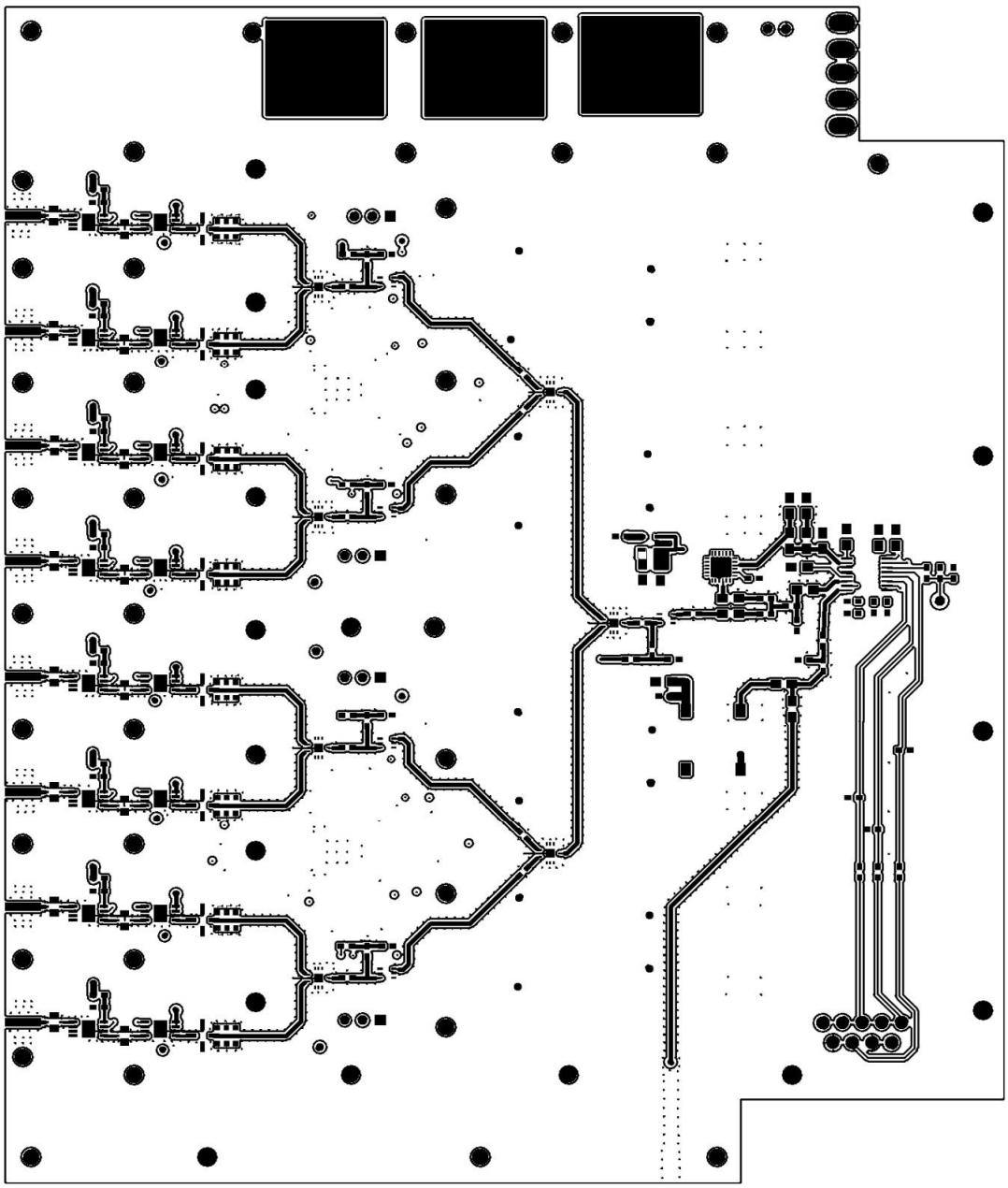

Bottom Layer layout snapshot (IF layer)

art004.pho (Board layer 1) Scale=1.43 Tue Mar 16 16:10:55 2010

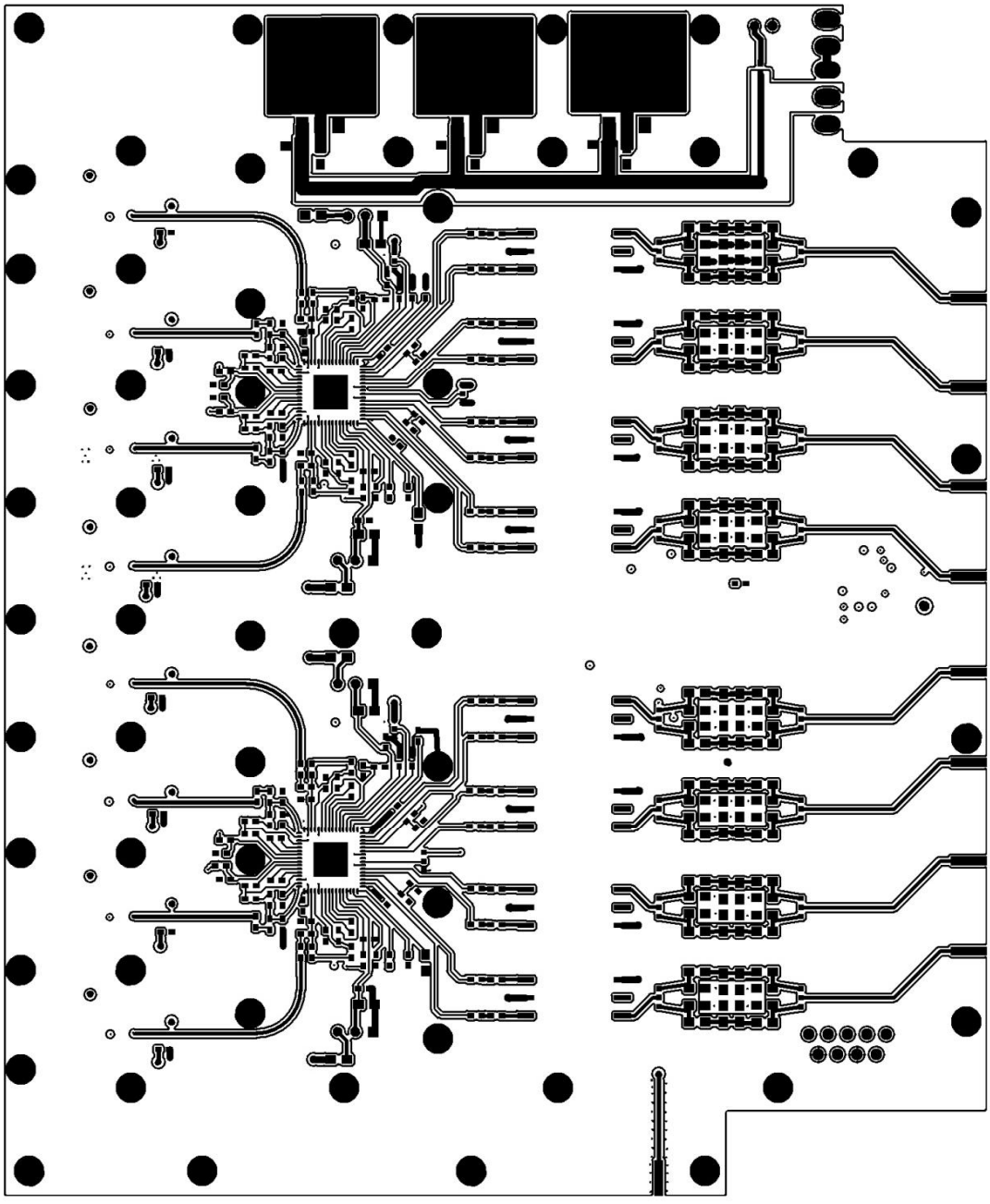

Assembly Top Layer

assembly_t.pho (Board layer 1) Scale=1.43 Tue Mar 16 16:12:10 2010

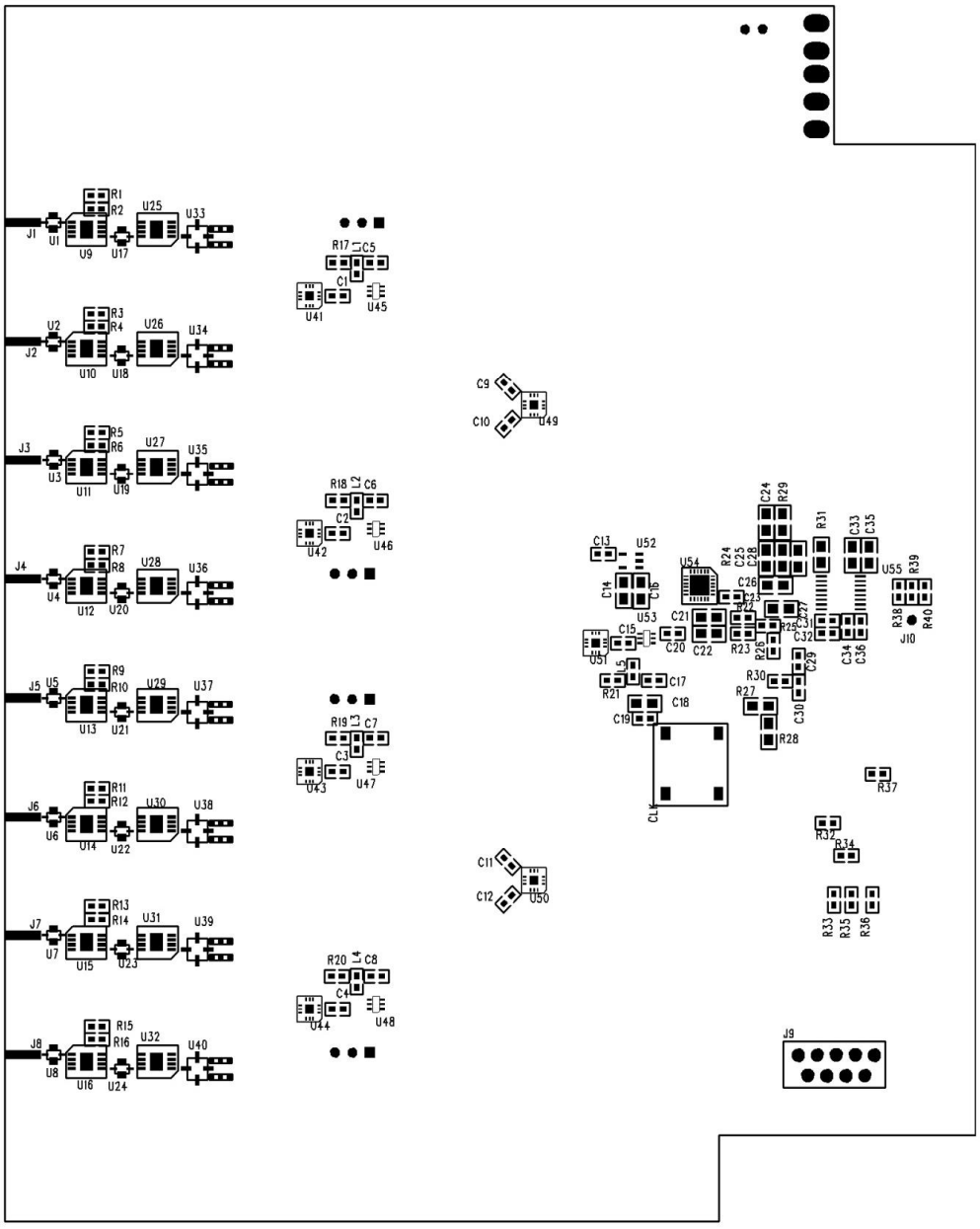

Assembly Bottom Layer

assembly_b.pho (Board layer 1) Scale=1.43 Tue Mar 16 16:44:57 2010

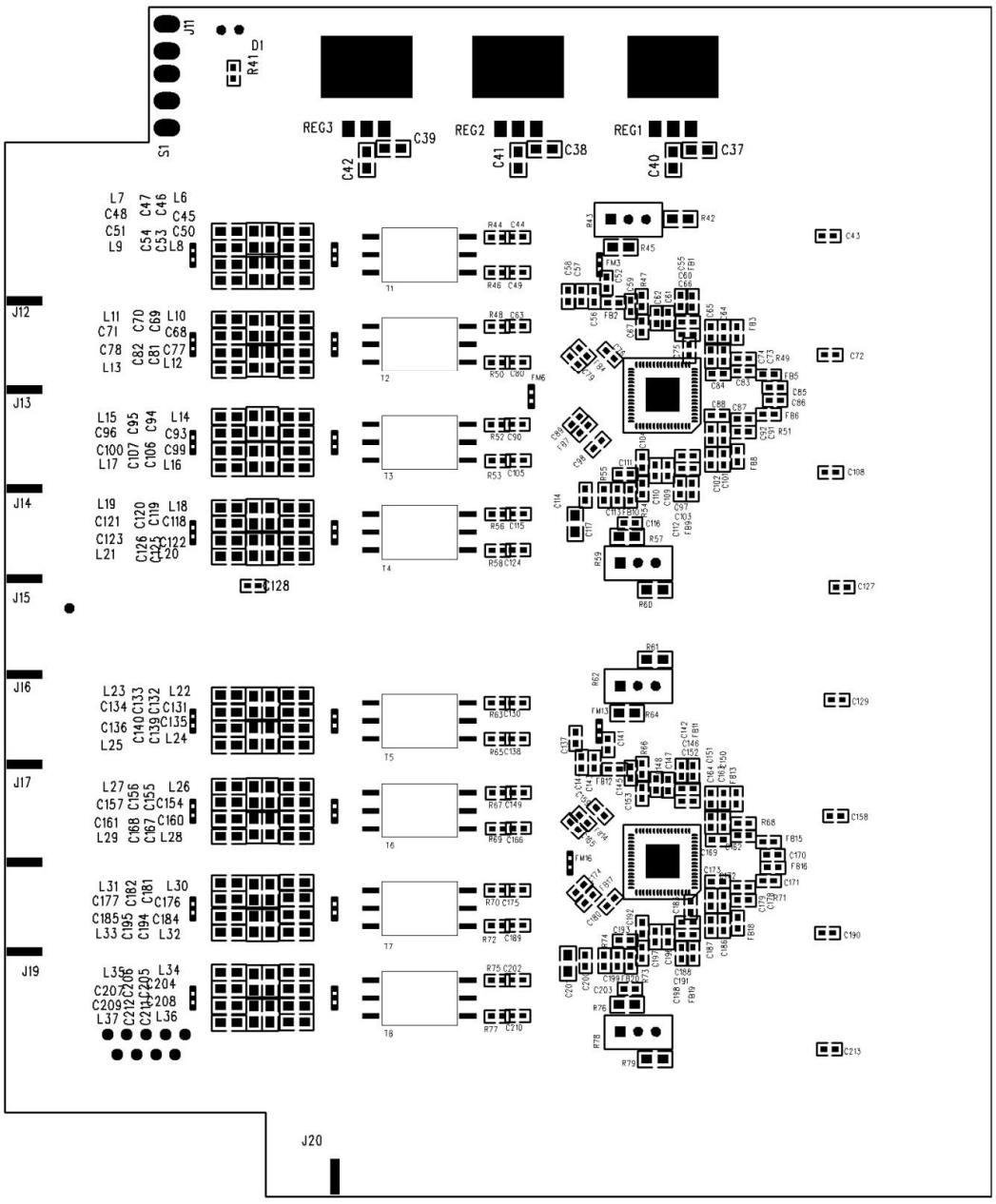

Bill of material

Item #	Quantity	Part reference in schematic	Part number	Manifacturer	Part name	Part value	Footprint reference
1	2	U56-57	AD8334	Analog Devices Inc	IC VGA QUAD W/PREAMP 64-LFCSP		LFCSP_VQ64
2	1	U55	ADF4106	analog devices	frequency synthesizer		TSSOP-16
3	73	C44 C49 C52 C56-64 C67 C74 C79-80 C83-90 C92 C101 C103-104 C109-111 C113-116 C124 C130 C137-138 C141 C143-150 C153 C162 C164-166 C169-175 C179 C186 C189 C191-193 C196-197 C199-200 C202-203 C210	CAP0402	Murata Electronics North America	CAP CER .1UF 10V 10% X5R 0402	0.1µF	603
4	8	C178 C112 C142 C163 C55 C198 C91 C73	CAP0402	Panasonic - ECG	CAP 18000PF 16V CERAMIC X7R 0402	0.018µF	603
5	8	C66 C188 C187 C65 C102 C97 C151-152	CAP0402	Murata Electronics North America	CAP CER 22PF 50V 5% C0G 0402	22pF	603
6	1	C105	CAP0402	Murata Electronics North America	CAP CER .1UF 10V 10% X5R 0402	0.1µF	402
7	1	C13	CAP0603	IPC SM-782 STD.	SURFACE MOUNT CAPACITOR 0.031 X 0.061 INCHES	.01uF	603
8	8	C43 C72 C108 C127 C129 C158 C190 C213	CAP0603	IPC SM-782 STD.	SURFACE MOUNT CAPACITOR 0.031 X 0.061 INCHES	???	603
9	6	C75 C159 C180 C183 C76 C98	CAP0603	Panasonic - ECG	CAP 1UF 6.3V CERAMIC X5R 0603	1.0µF	603
10	2	C117 C201	CAP0805	Murata Electronics North America	CAP CER 10UF 6.3V X5R 0805	10µF	805
11	10	C1-4 C9-12 C15 C20	CAP-CK13	KEMET	AXIAL CERAMIC CAPACITOR, MIL-SPEC SIZE CK13	100pF	603
12	7	C7-8 C5 C17 C6 C31 C36	CAP-CK13	KEMET	AXIAL CERAMIC CAPACITOR, MIL-SPEC SIZE CK13	0.1uF	603
13	4	C19 C32 C34 C128	CAP-CK13	KEMET	AXIAL CERAMIC CAPACITOR, MIL-SPEC SIZE CK13	10pF	603
14	1	C23	CAP-CK13	KEMET	AXIAL CERAMIC CAPACITOR, MIL-SPEC SIZE CK13	22uF	603
15	1	C24	CAP-CK13	KEMET	AXIAL CERAMIC CAPACITOR, MIL-SPEC SIZE CK13	20pF	805
16	1	C25	CAP-CK13	KEMET	AXIAL CERAMIC CAPACITOR, MIL-SPEC SIZE CK13	1.5nF	805
17	5	C26-28 C21-22	CAP-CK13	KEMET	AXIAL CERAMIC CAPACITOR, MIL-SPEC SIZE CK13	100pF	805
18	2	C14 C16	CAP-CK13			2.2uF	805
19	1	C33	CAP-CK13	KEMET	AXIAL CERAMIC CAPACITOR, MIL-SPEC SIZE CK13	0.1pF	805
20	2	C29-30	CAP-CK13	KEMET	AXIAL CERAMIC CAPACITOR, MIL-SPEC SIZE CK13	1nF	603
21	1	C18	CAP-CK13	KEMET	AXIAL CERAMIC CAPACITOR, MIL-SPEC SIZE CK13	22uF	805
22	3	C37-39	CAP-CK13	KEMET	AXIAL CERAMIC CAPACITOR, MIL-SPEC SIZE CK13	10uF	805
23	3	C40-42	CAP-CK13	KEMET	AXIAL CERAMIC CAPACITOR, MIL-SPEC SIZE CK13	10.uF	805
24	16	C45 C48 C68 C71 C93 C96 C118 C121 C131 C134 C154 C157 C176-177 C204 C207	CAP-CK13	KEMET	AXIAL CERAMIC CAPACITOR, MIL-SPEC SIZE CK13	3.8nF	805
25	16	C50-51 C99-100 C122-123 C135-136 C160-161 C77-78 C184-185 C208-209	CAP-CK13	KEMET	AXIAL CERAMIC CAPACITOR, MIL-SPEC SIZE CK13	0.38nF	805
26	1	C35	CAP-CK13	KEMET	AXIAL CERAMIC CAPACITOR, MIL-SPEC SIZE CK13	10pF	805
27	16	C47 C132-133 C69-70 C155-156 C46 C119-120 C181-182 C95 C94 C205-206	CAP-CK13	KEMET	AXIAL CERAMIC CAPACITOR, MIL-SPEC SIZE CK13	3.3nF	805
28	16	C107 C54 C139-140 C53 C106 C194-195 C81 C167-168 C82 C125-126 C211-212	CAP-CK13	KEMET	AXIAL CERAMIC CAPACITOR, MIL-SPEC SIZE CK13	0.33nF	805
29	4	R43 R59 R62 R78	CT-94W	Copal Electronics Inc	POT 10K OHM SQ CERMET TOP	10.0K	CT-94EW
30	1	J9	DB9-WIRE	TYCO ELECTRONICS	STRAIGHT DB9 CONNECTOR		DB9-STRAIGHT_WIRE_M

31	20	FM1-20	FACTORY_MODE_0805				0805_FM
32	20	FB1-20	FERRITE_BEAD_0603	Murata	FERRITE CHIP 75 OHM 300MA 0603	120nH	603
33	16	L6-7 L10-11 L14-15 L18-19 L22-23 L26-27 L30-31 L34-35	FERRITE_BEAD_0603	Murata	FERRITE CHIP 75 OHM 300MA 0603	10uH	805
34	16	L8-9 L24-25 L16-17 L28-29 L12-13 L32-33 L20-21 L36-37	FERRITE_BEAD_0603	Murata	FERRITE CHIP 75 OHM 300MA 0603	1uH	805
35	16	U1-8 U17-24	FILTER_5515BP15C1020	panasonic	bandpass filter		0805_FILTER
36	1	CLK	FOX_801_TCXO		10 MHz ref clock		FOX801
37	8	U33-40	GAT-ATT				PL-126-ATTN
38	8	U9-16	HMC318	hittite	pre amp		MSOP8-G
39	8	U25-32	HMC488	hittite	mixer		MSOP8-G
40	5	U45-48 U53	HMC311SC70				SC70-6
41	1	U54	HMC431LP4				QFN24_GND
42	5	L1-5	IND-MOLDED		MOLDED INDUCTOR, 0.5" PIN SPACING	3.3 nH	603
43	1	D1	LED_SMT_0603	Cree Inc	LED 4MM OVAL BLUE 470NM		LED
44	16	F1-16	LINE_PHASE_TUNE	LITTELFUSE 345-101	FUSE HOLDER, PCB MOUNT, 1.25 X .25" FUSES	???	0805_FM
45	3	REG1-3	LT1086-3V	NATIONAL SEMICONDUCTOR	5 VOLT, VOLTAGE REGULATOR		DDPAK3_LINEAR
46	1	J11	POWER_FEED_TH		GENERIC 2 PIN SIP HEADER .100 CENTERS		POWER_IN_22GUAGE
47	16	R44 R46 R48 R50 R52-53 R56 R58 R63 R65 R67 R69-70 R72 R75 R77	RES0402	Vishay/Dale	RES 187 OHM 1/16W 1% 0402 SMD	237	603
48	2	R55 R74	RES0402	Vishay/Dale	RES 10K OHM 1/16W 5% 0402 SMD	10k	603
49	8	R51 R49 R71 R47 R73 R68 R54 R66	RES0402	Vishay/Dale	RES 274 OHM 1/16W 1% 0402 SMD	274	603
50	2	R27-28	RES0805	Yageo	RES 39K OHM 1/16W 5% 0402 SMD	0	805
51	4	R42 R60-61 R79	RES0805	Yageo	RES 39K OHM 1/16W 5% 0402 SMD	39.0K	805
52	4	R57 R64 R76 R45	RES0805	Yageo	RES 39K OHM 1/16W 5% 0402 SMD	0(optional)	805
53	16	R1-16	RES-WR1	IPC SM-782 STD.	WIRE WOUND RESISTOR 3.4 X 7.05 MM	FS	603
54	5	R17-21	RES-WR1	IPC SM-782 STD.	WIRE WOUND RESISTOR 3.4 X 7.05 MM	100	603
55	3	R22-23 R25	RES-WR1	IPC SM-782 STD.	WIRE WOUND RESISTOR 3.4 X 7.05 MM	18	603
56	1	R24	RES-WR1	IPC SM-782 STD.	WIRE WOUND RESISTOR 3.4 X 7.05 MM	6.2k	805
57	2	R26 R30	RES-WR1	IPC SM-782 STD.	WIRE WOUND RESISTOR 3.4 X 7.05 MM	51	603
58	1	R29	RES-WR1	IPC SM-782 STD.	WIRE WOUND RESISTOR 3.4 X 7.05 MM	4.3k	805
59	1	R31	RES-WR1	IPC SM-782 STD.	WIRE WOUND RESISTOR 3.4 X 7.05 MM	5.1k	805
60	3	R32 R34 R37	RES-WR1	IPC SM-782 STD.	WIRE WOUND RESISTOR 3.4 X 7.05 MM	10k	603
61	3	R35-36 R33	RES-WR1	IPC SM-782 STD.	WIRE WOUND RESISTOR 3.4 X 7.05 MM	330	603
62	3	R38-40	RES-WR1	IPC SM-782 STD.	WIRE WOUND RESISTOR 3.4 X 7.05 MM	10K	603
63	1	R41	RES-WR1	IPC SM-782 STD.	WIRE WOUND RESISTOR 3.4 X 7.05 MM	270	603
64	16	J1-8 J12-18 J20	SMA_CM	Amphenol Connex	CONN SMA FEMALE PANEL MT 2 HOLE		SMA_CM
65	1	J19	SMA_CM	Pomona	SMB Connectors SMB JACK PANEL RECEPTACLE		SMA_CM
66	1	S1	SW-SPST-NO	C&K Components	SWITCH TOGGLE SPST SOLDER LUG	???	SPDT-CASEMT
67	8	T1-8	T1-6T	DALE TA-10-08	600 - 600 OHM TELEPHONE COUPLING AUDIO TRANSFORMER		W38_MINI_C_RF_TRANSF
68	1	J10	TEST_POINT		Through Hole PC Test Point		TEST_POINT
69	1	U52	TPS73633DBVT				SOT23-5
70	7	U41-44 U49-51	WP4F_2WAY		2way power splitter		DQ1255_1

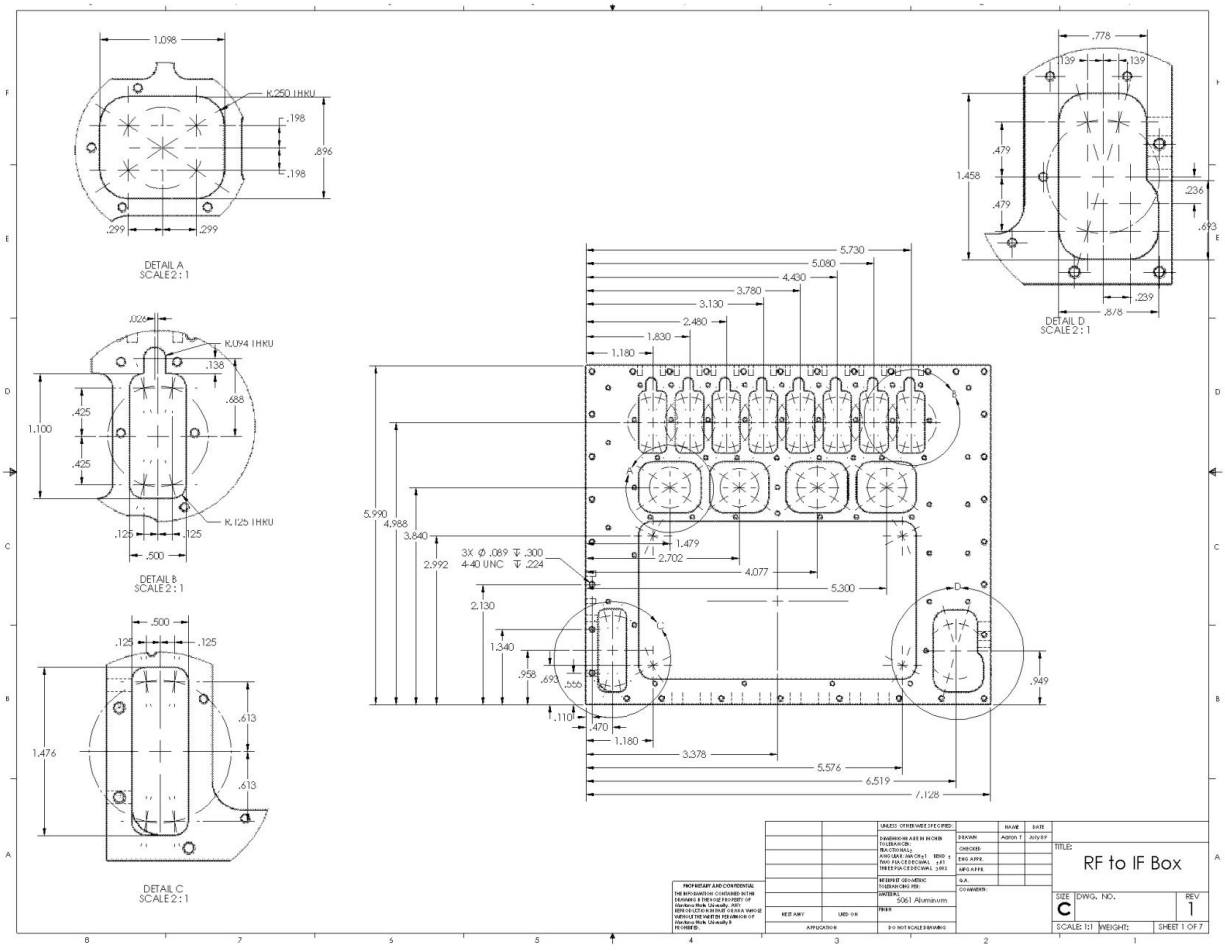
DETAIL A
SCALE 2 : 1
DETAIL B
SCALE 2 : 1
DETAIL C
SCALE 2 : 1
DETAIL D
SCALE 2 : 1
RF to IF Box
5061 Aluminum
SIZE C
DWG. NO.
REV 1
SCALE: 1:1
SHEET 1 OF 7

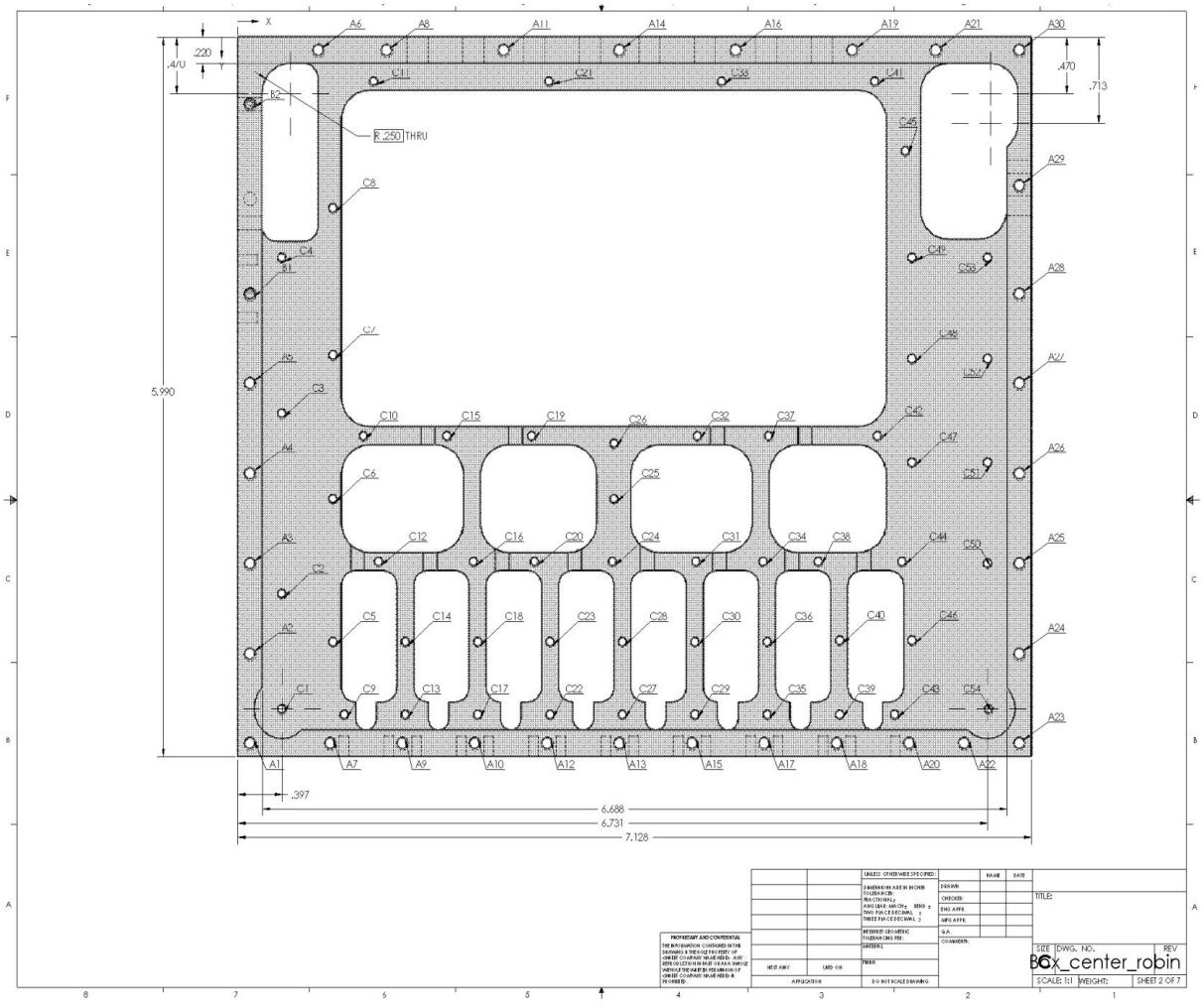
.220
.470
.713
5.990
R .250 THRU
.397
6.688
6.731
7.128
Box_center_robin

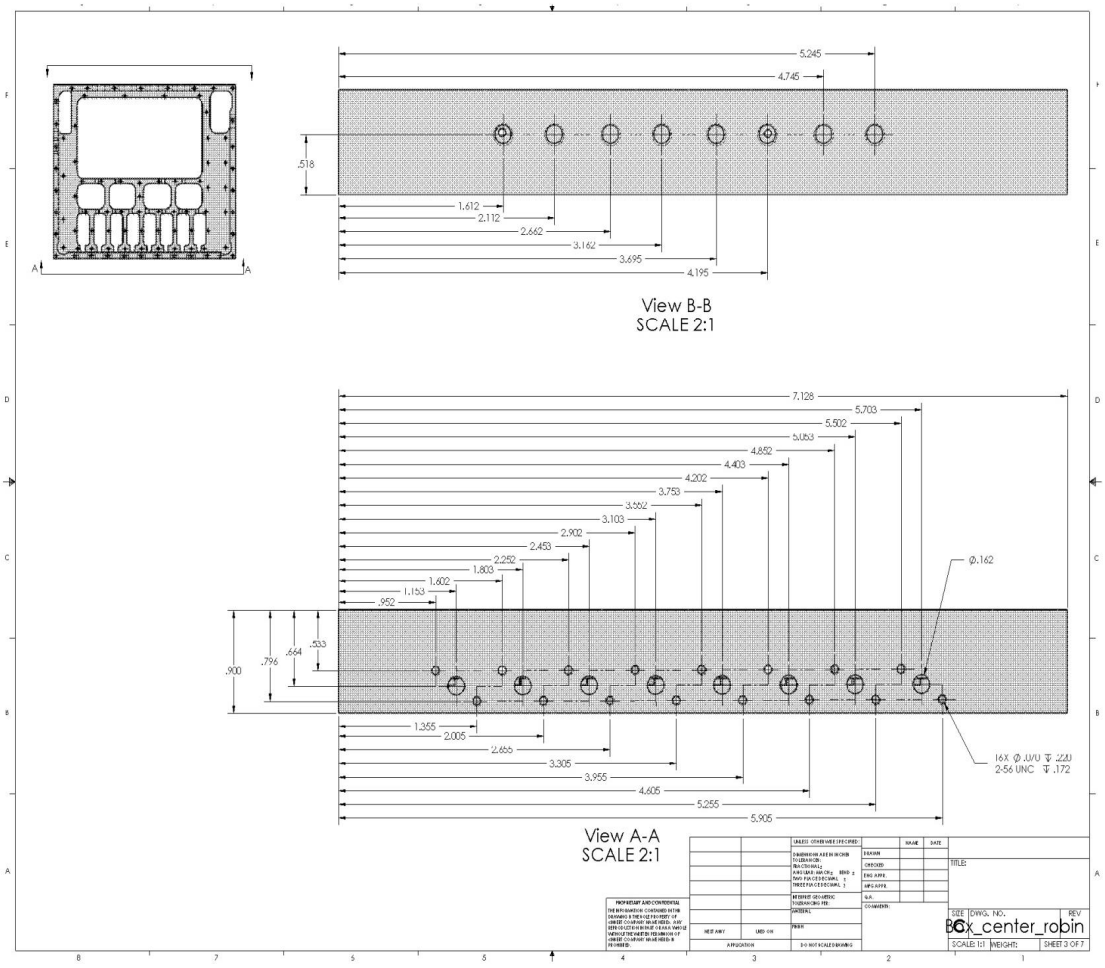
5.245
4.745
.518
1.612
2.112
2.662
3.162
3.695
4.195
A
A
View B-B
SCALE 2:1
7.128
5.703
5.502
5.053
4.852
4.403
4.202
3.753
3.552
3.103
2.902
2.453
2.252
1.803
1.602
1.153
.952
Ø.162
.900
.796
.664
.533
1.355
2.005
2.655
3.305
3.955
4.605
5.255
5.905
16X Ø.UU Ŧ .22U
2-56 UNC Ŧ .172
View A-A
SCALE 2:1
UNLESS OTHERWISE SPECIFIED:
NAME
DATE
TITLE:
SIZE
DWG. NO.
REV
Box_center_robin
SCALE: 1:1
WEIGHT:
SHEET 3 OF 7

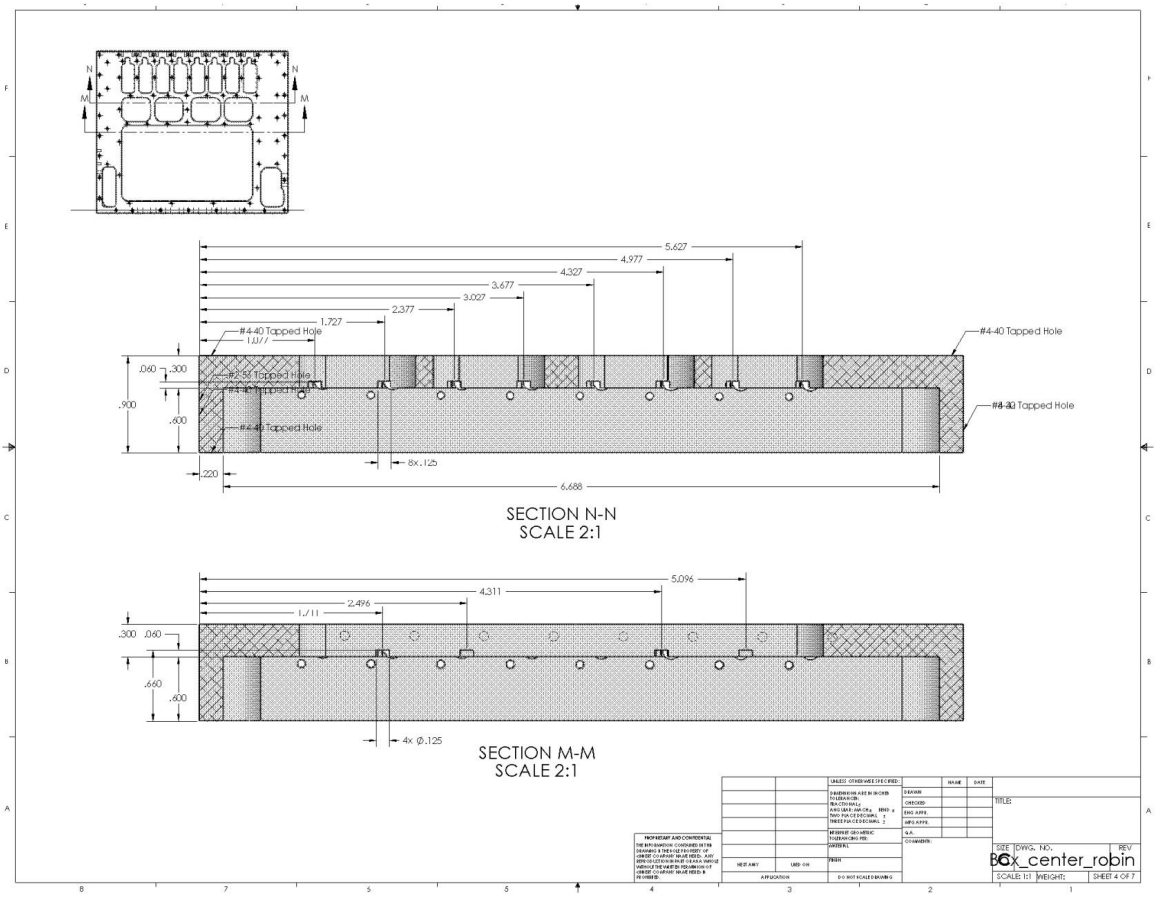
N
M
5.627
4.977
4.327
3.677
3.027
2.377
1.727
#4-40 Tapped Hole
#4-40 Tapped Hole
.060
.300
.900
.600
#4-40 Tapped Hole
8x .125
.220
6.688
SECTION N-N
SCALE 2:1
5.096
4.311
2.496
.300
.060
.660
.600
4x Ø.125
SECTION M-M
SCALE 2:1
UNLESS OTHERWISE SPECIFIED:
DRAWN
CHECKED
ENG APPR.
MFG APPR.
Q.A.
COMMENTS:
NAME
DATE
TITLE:
SIZE
DWG. NO.
REV
Box_center_robin
SCALE: 1:1
WEIGHT:
SHEET 4 OF 7

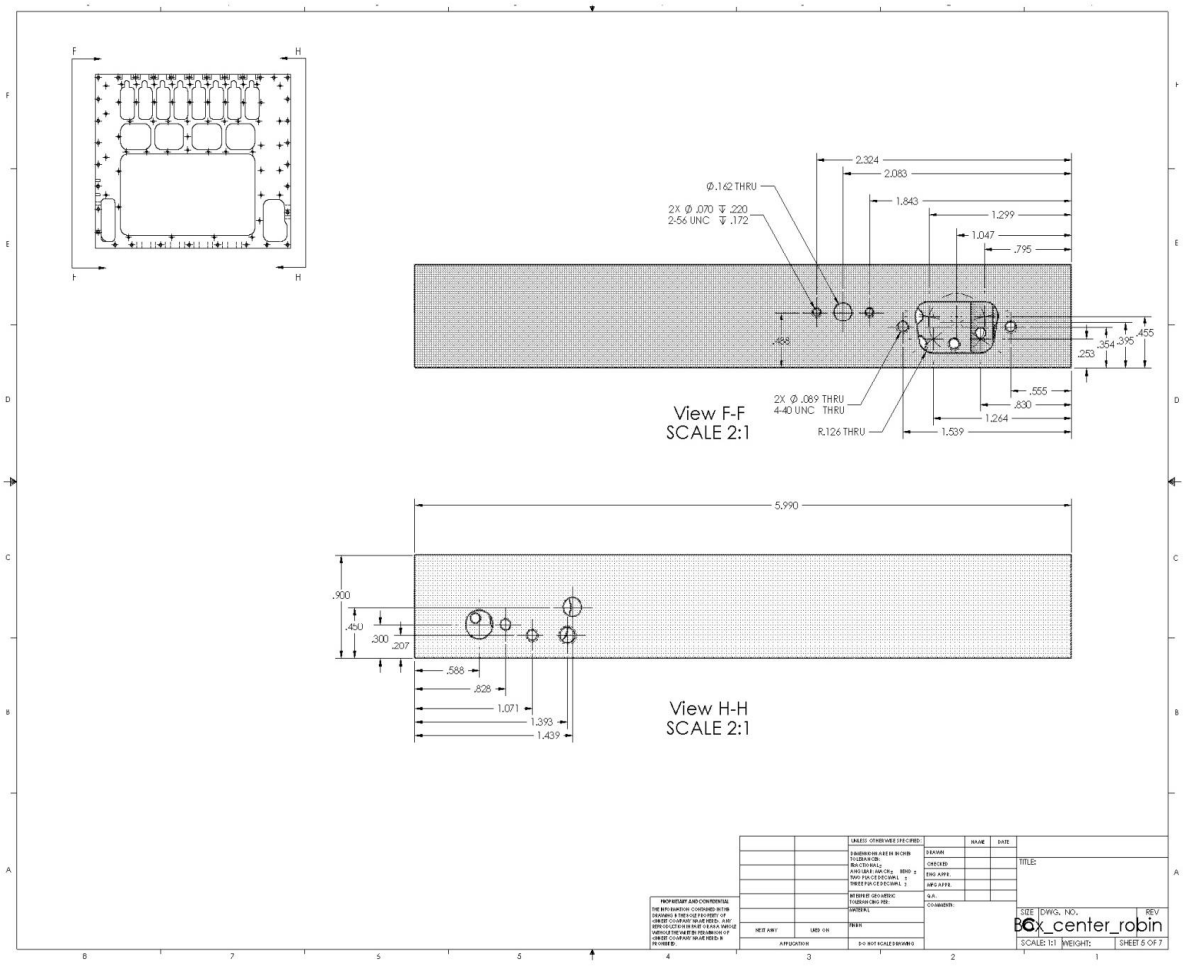
F
H
Ø.162 THRU
2X Ø .070 ↧ .220
2-56 UNC ↧ .172
2.324
2.083
1.843
1.299
1.047
.795
.888
.354
.395
.455
.253
2X Ø .089 THRU
4-40 UNC THRU
R.126 THRU
.555
.830
1.264
1.539
View F-F
SCALE 2:1
5.990
.900
.450
.300
.207
.588
.828
1.071
1.393
1.439
View H-H
SCALE 2:1
PROPRIETARY AND CONFIDENTIAL
UNLESS OTHERWISE SPECIFIED:
NAME
DATE
DRAWN
CHECKED
ENG APPR.
MFG APPR.
Q.A.
COMMENTS:
TITLE:
SIZE
DWG. NO.
REV
Box_center_robin
SCALE: 1:1
WEIGHT:
SHEET 5 OF 7

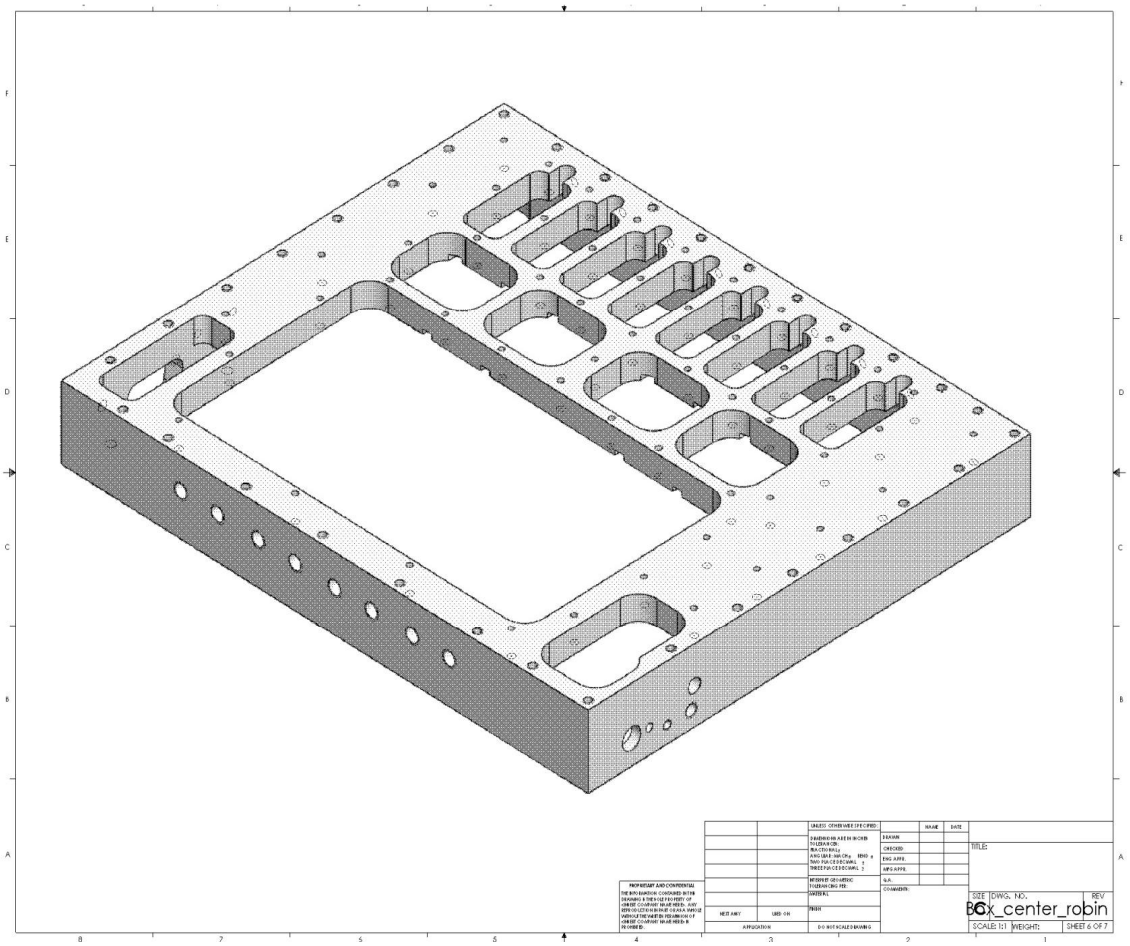
UNLESS OTHERWISE SPECIFIED:
NAME
DATE
DRAWN
CHECKED
ENG APPR.
MFG APPR.
Q.A.
COMMENTS:
TITLE:
SIZE
DWG. NO.
REV
Box_center_robin
SCALE: 1:1
WEIGHT:
SHEET 6 OF 7
NEXT ASSY
USED ON
APPLICATION
DO NOT SCALE DRAWING

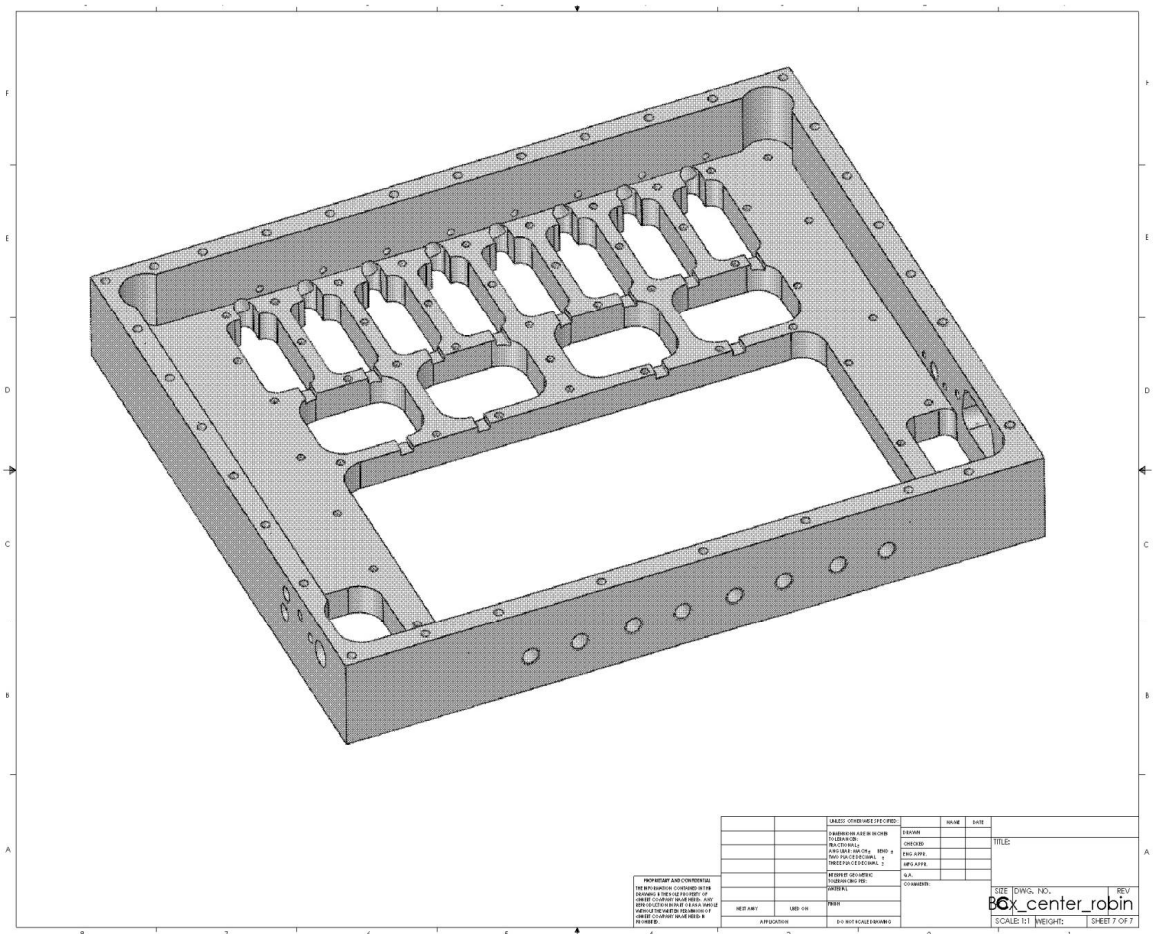
Box_center_robin

APPENDIX B

TEST RESULTS

Data set 1

Single CW Source

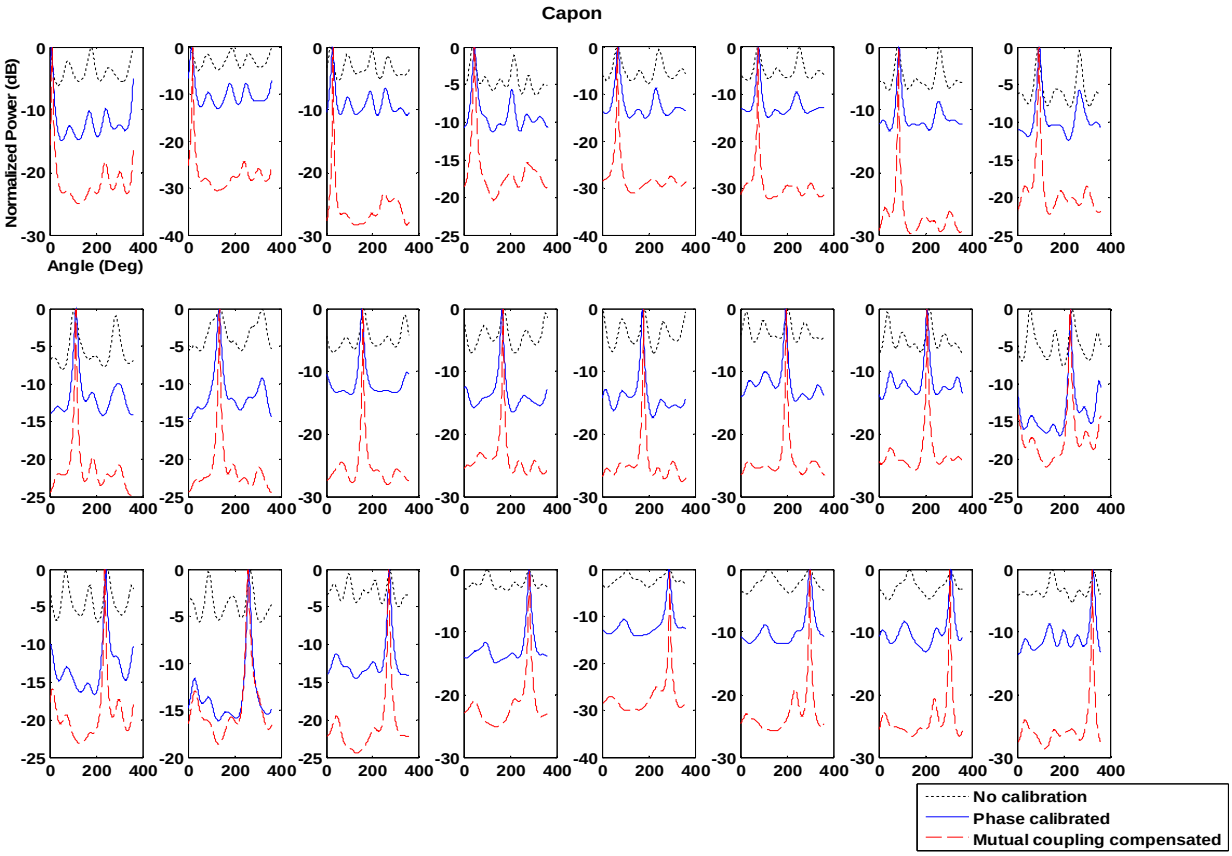
Capon
Normalized Power (dB)
Angle (Deg)
No calibration
Phase calibrated
Mutual coupling compensated

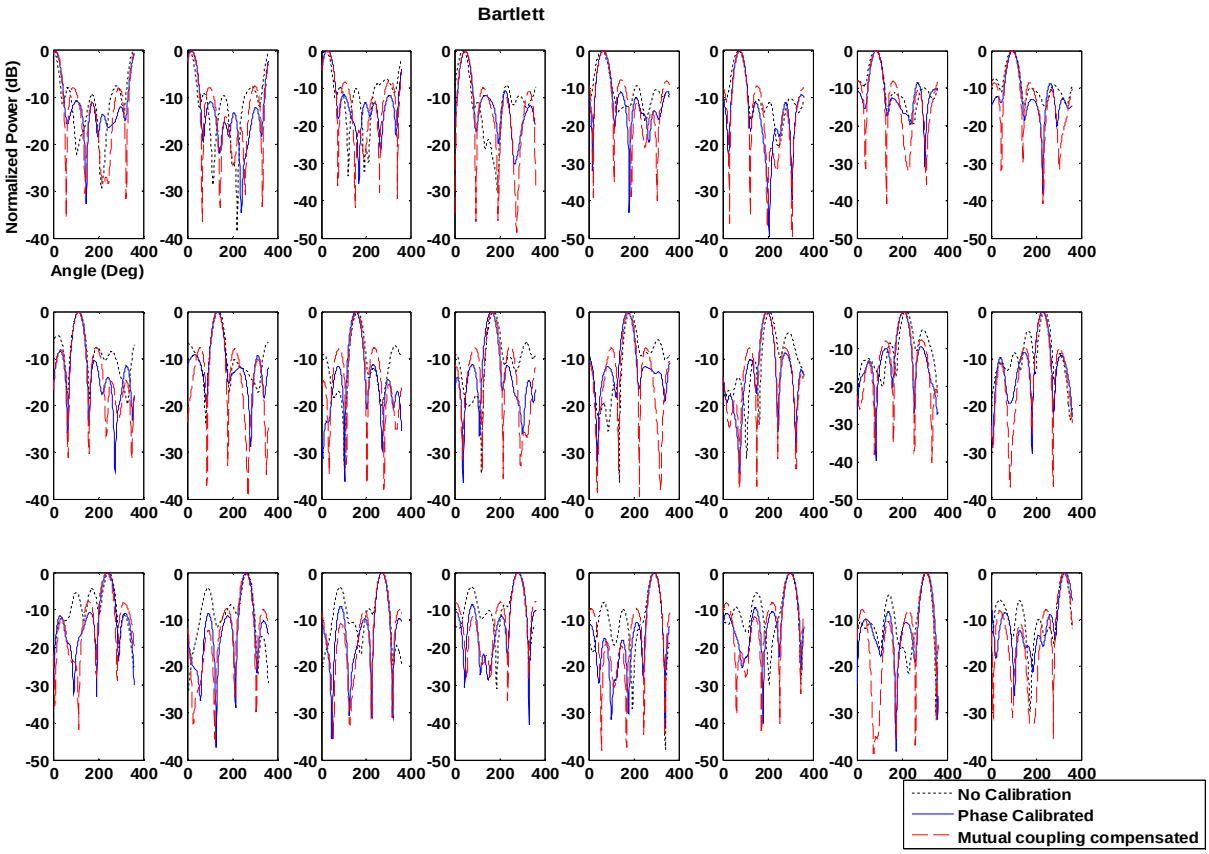
Bartlett
Normalized Power (dB)
Angle (Deg)
No Calibration
Phase Calibrated
Mutual coupling compensated

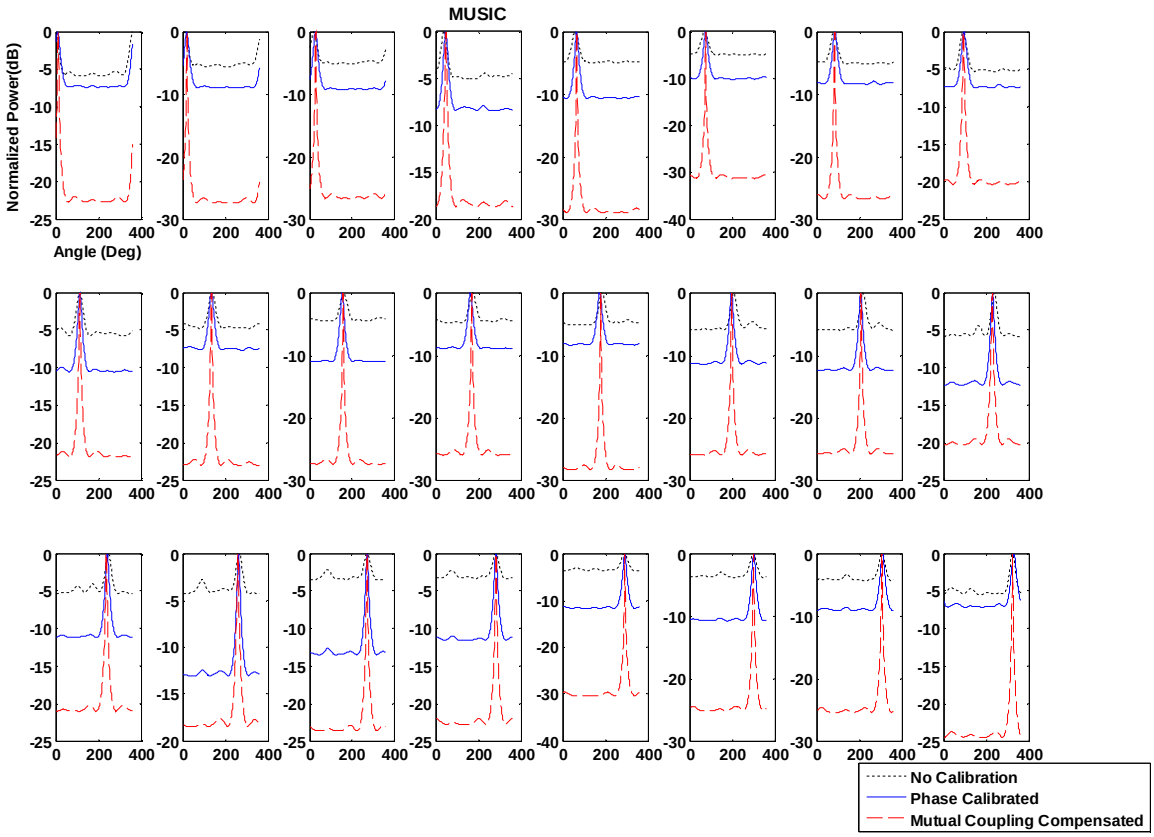
MUSIC
Normalized Power(dB)
Angle (Deg)
No Calibration
Phase Calibrated
Mutual Coupling Compensated

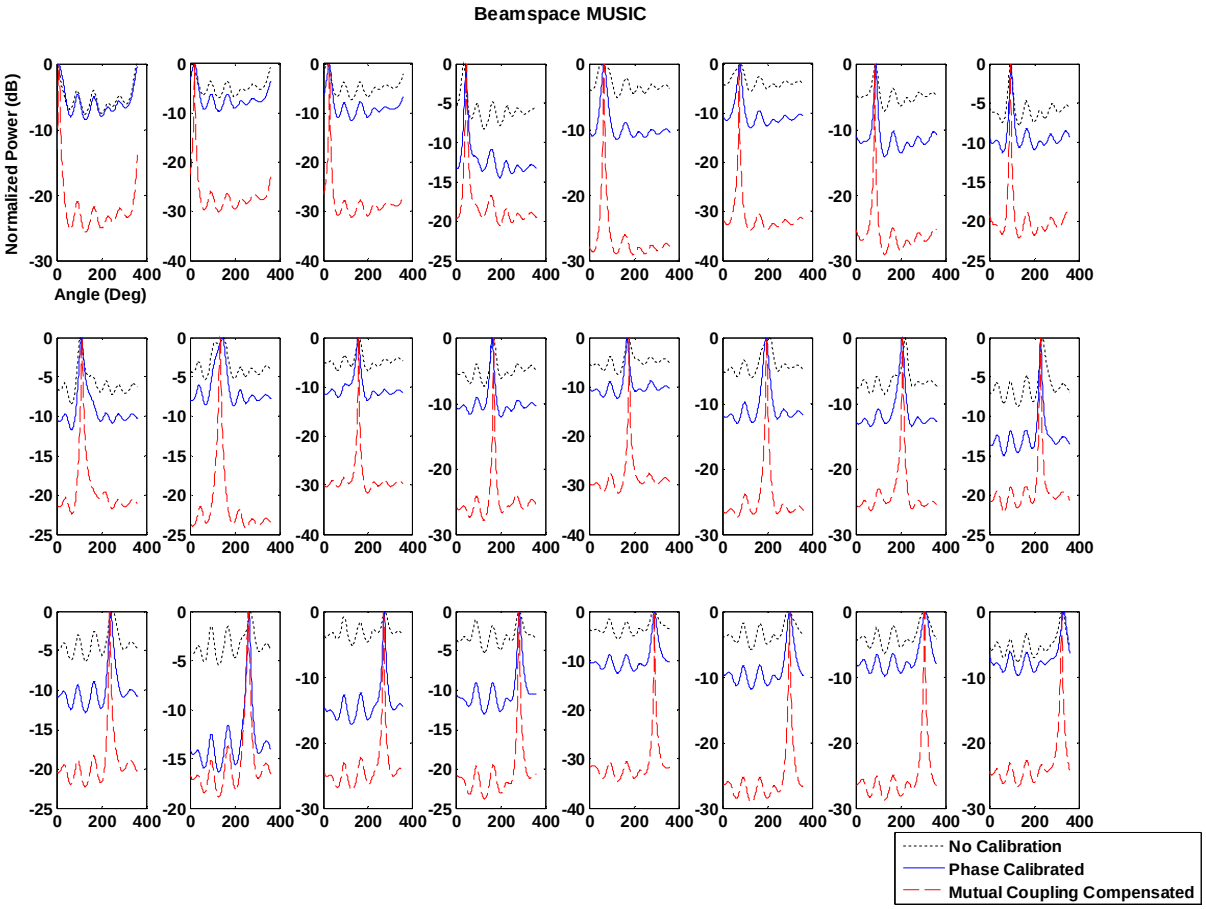
Beamspace MUSIC
Normalized Power (dB)
Angle (Deg)
No Calibration
Phase Calibrated
Mutual Coupling Compensated

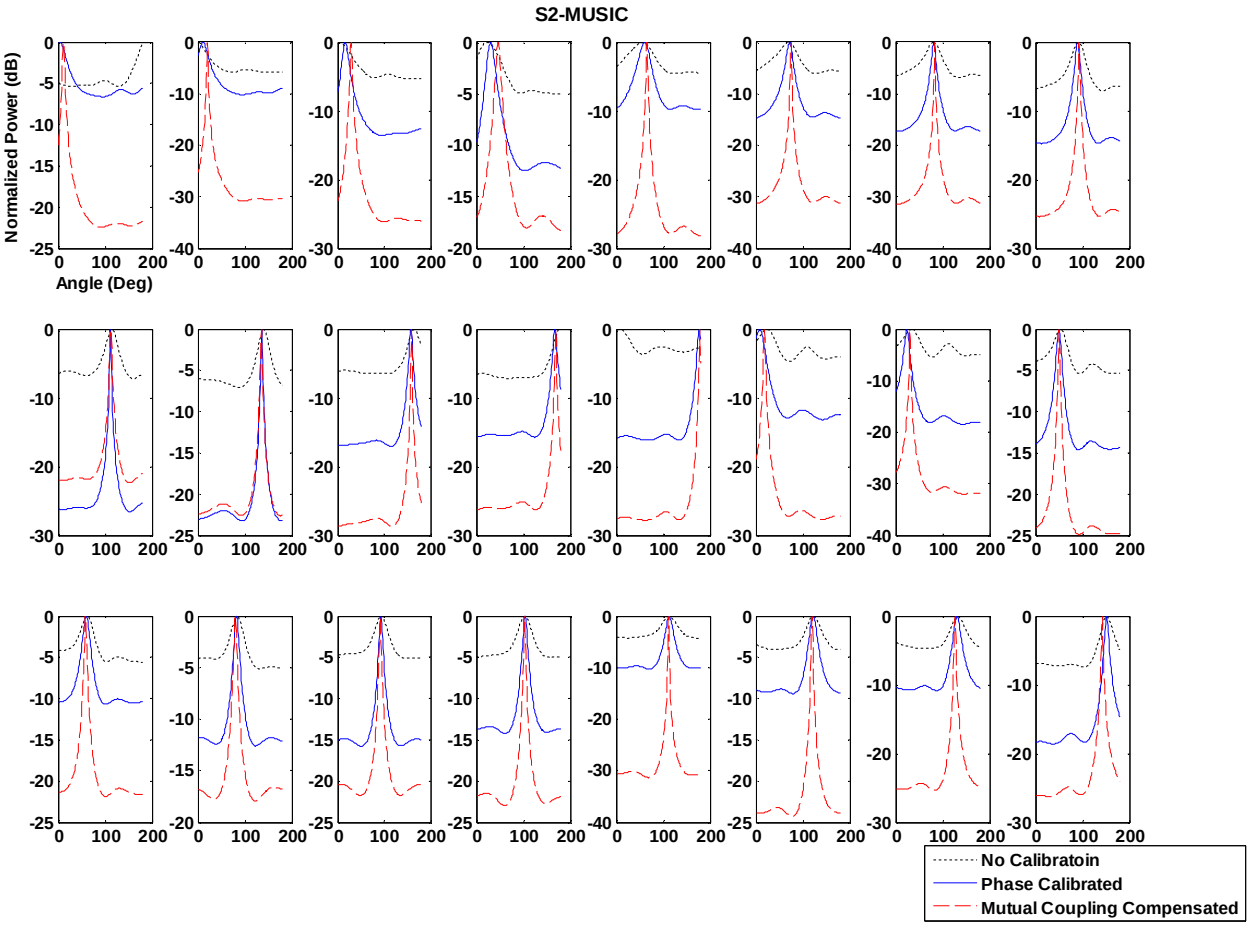
S2-MUSIC
Normalized Power (dB)
Angle (Deg)
No Calibratoin
Phase Calibrated
Mutual Coupling Compensated

Data set 2

Single CW Source

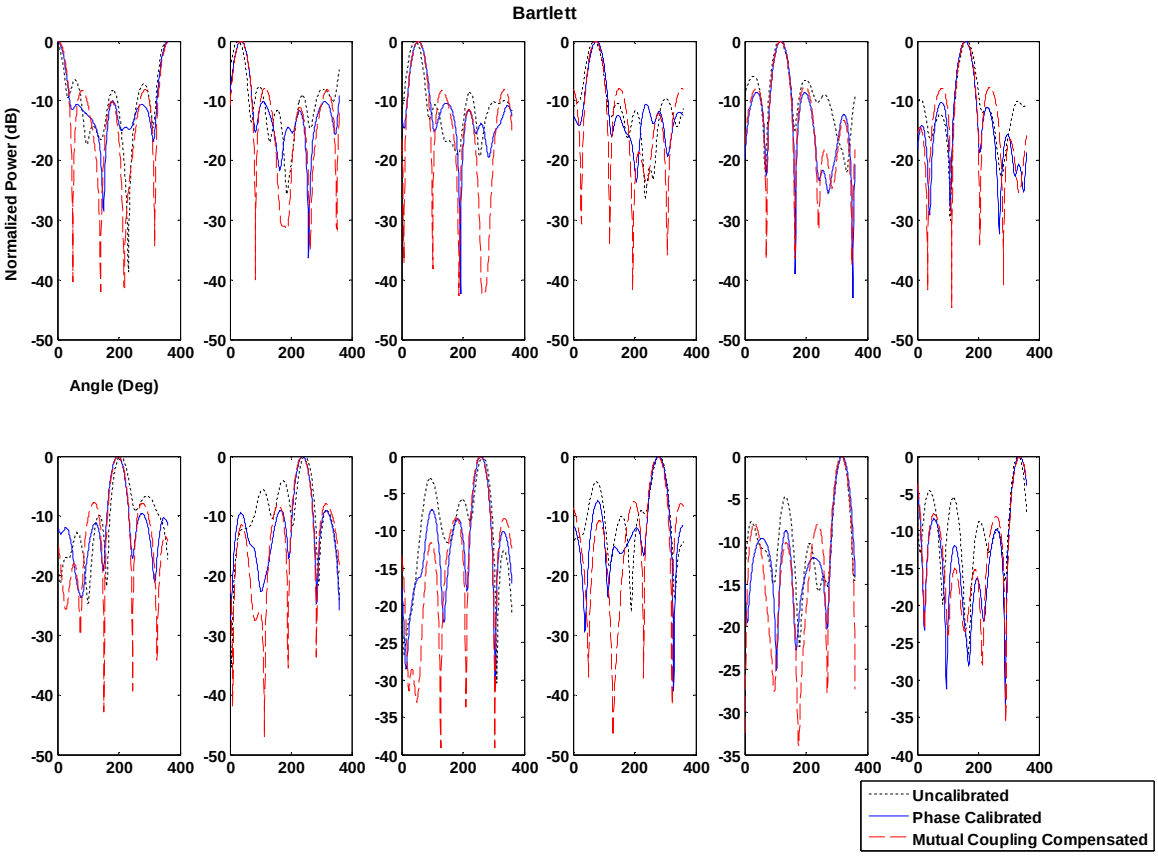
Bartlett
Normalized Power (dB)
Angle (Deg)
Uncalibrated
Phase Calibrated
Mutual Coupling Compensated

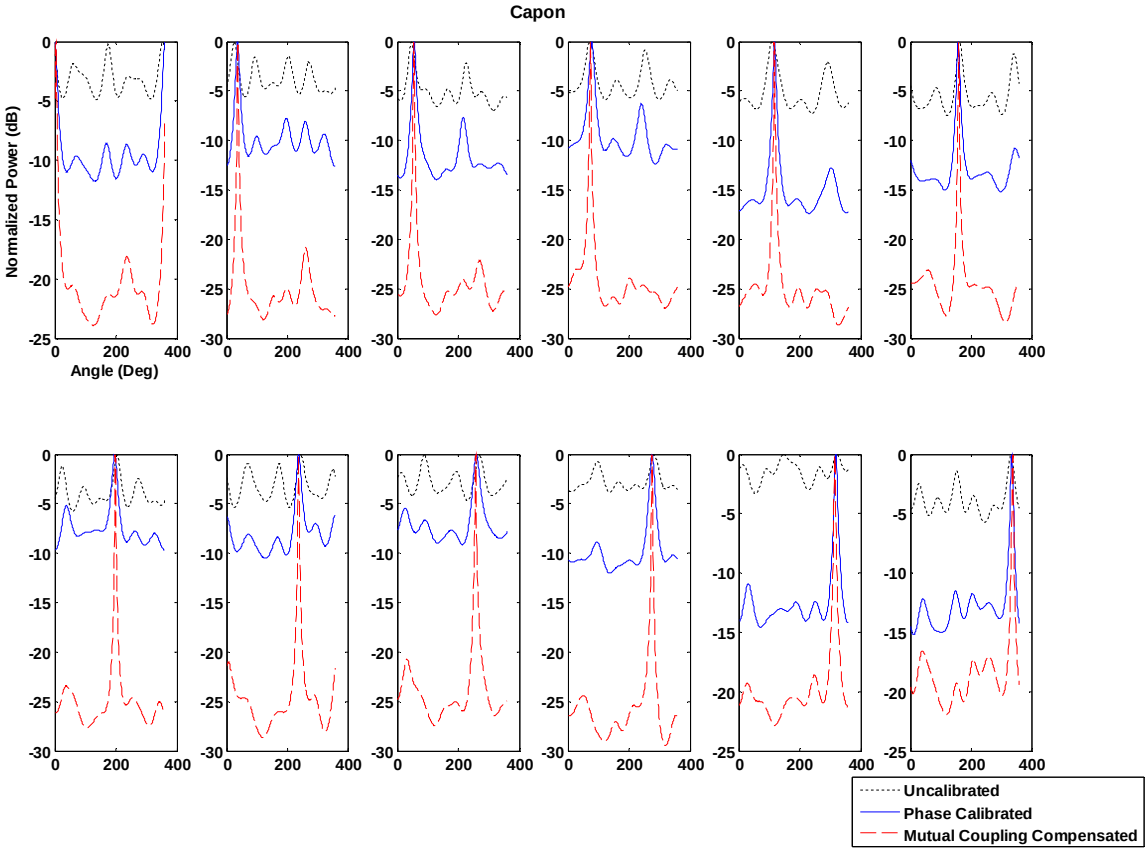
Capon
Normalized Power (dB)
Angle (Deg)
Uncalibrated
Phase Calibrated
Mutual Coupling Compensated

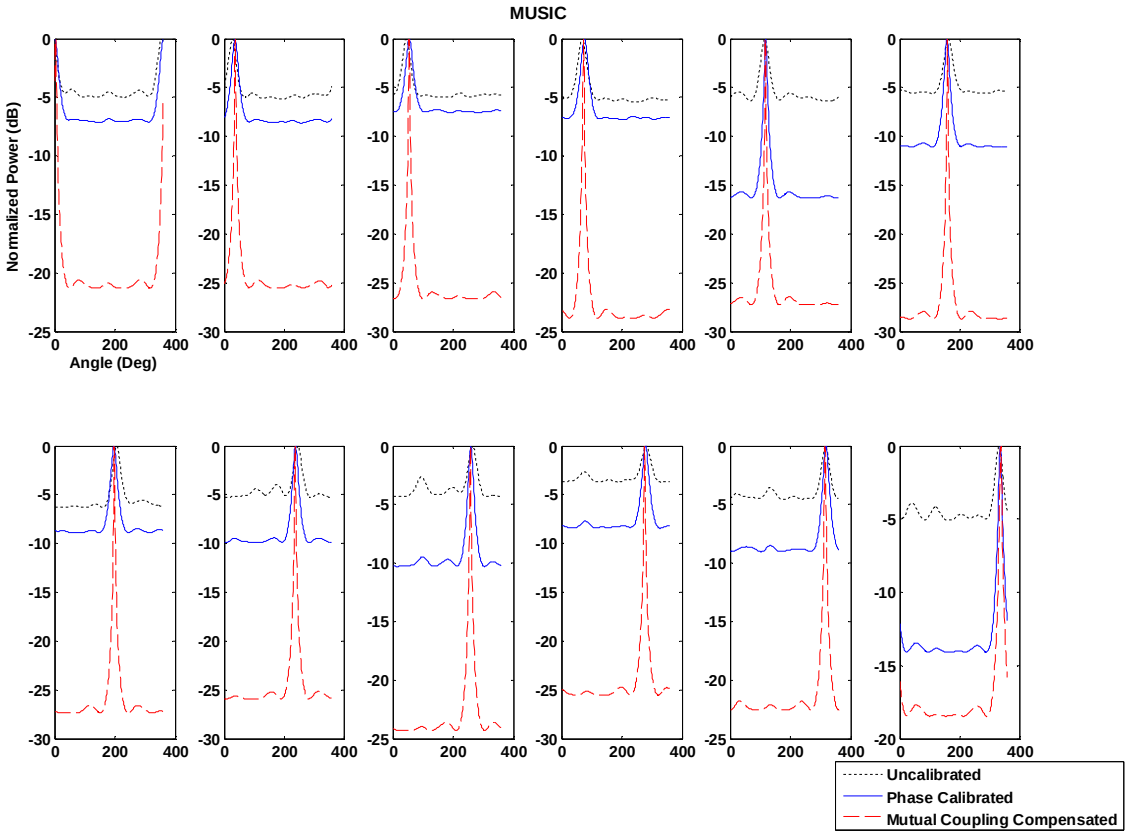
MUSIC
Normalized Power (dB)
Angle (Deg)
Uncalibrated
Phase Calibrated
Mutual Coupling Compensated

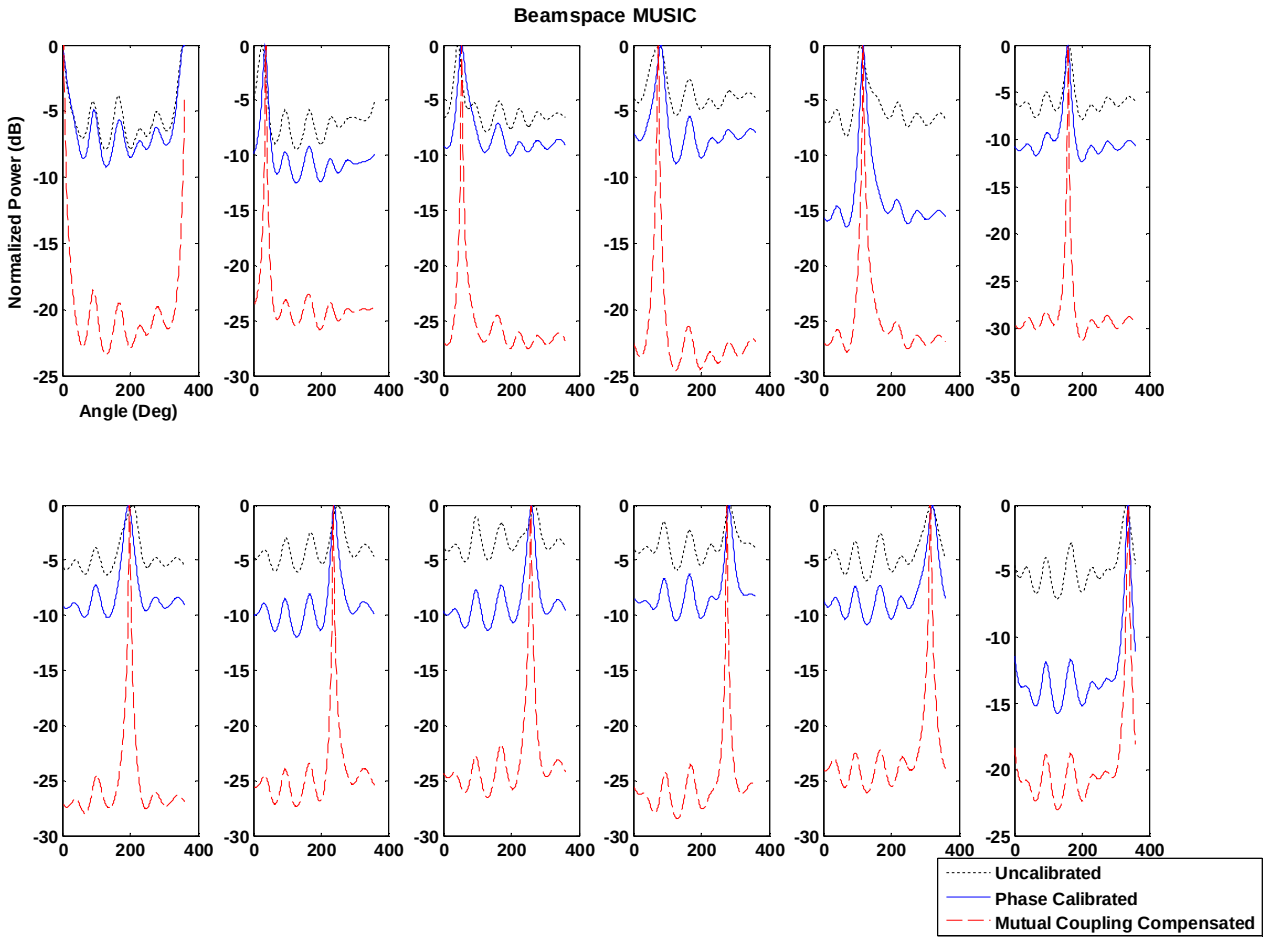
Beamspace MUSIC
Normalized Power (dB)
Angle (Deg)
Uncalibrated
Phase Calibrated
Mutual Coupling Compensated

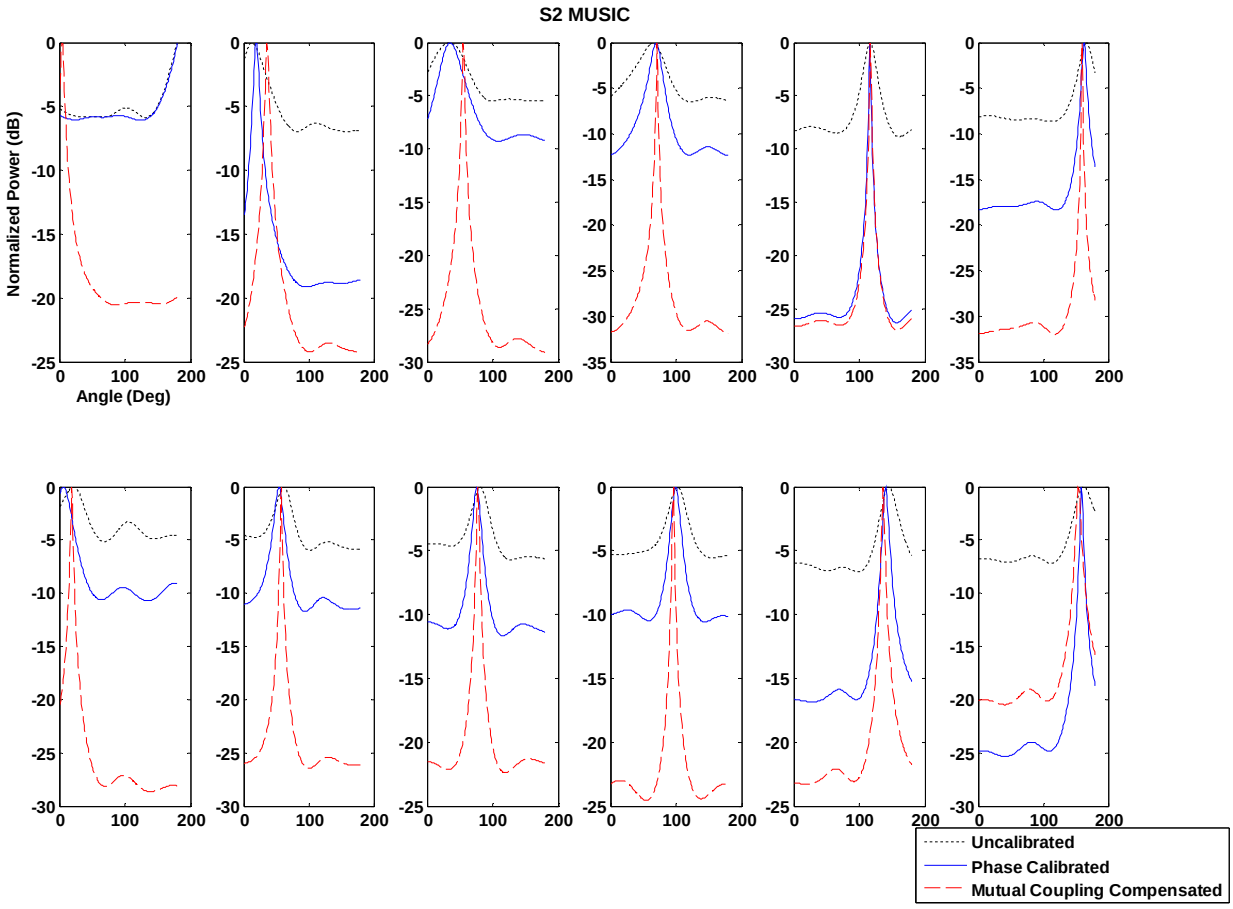
S2 MUSIC
Normalized Power (dB)
Angle (Deg)
Uncalibrated
Phase Calibrated
Mutual Coupling Compensated

Two CW signals with varying power difference

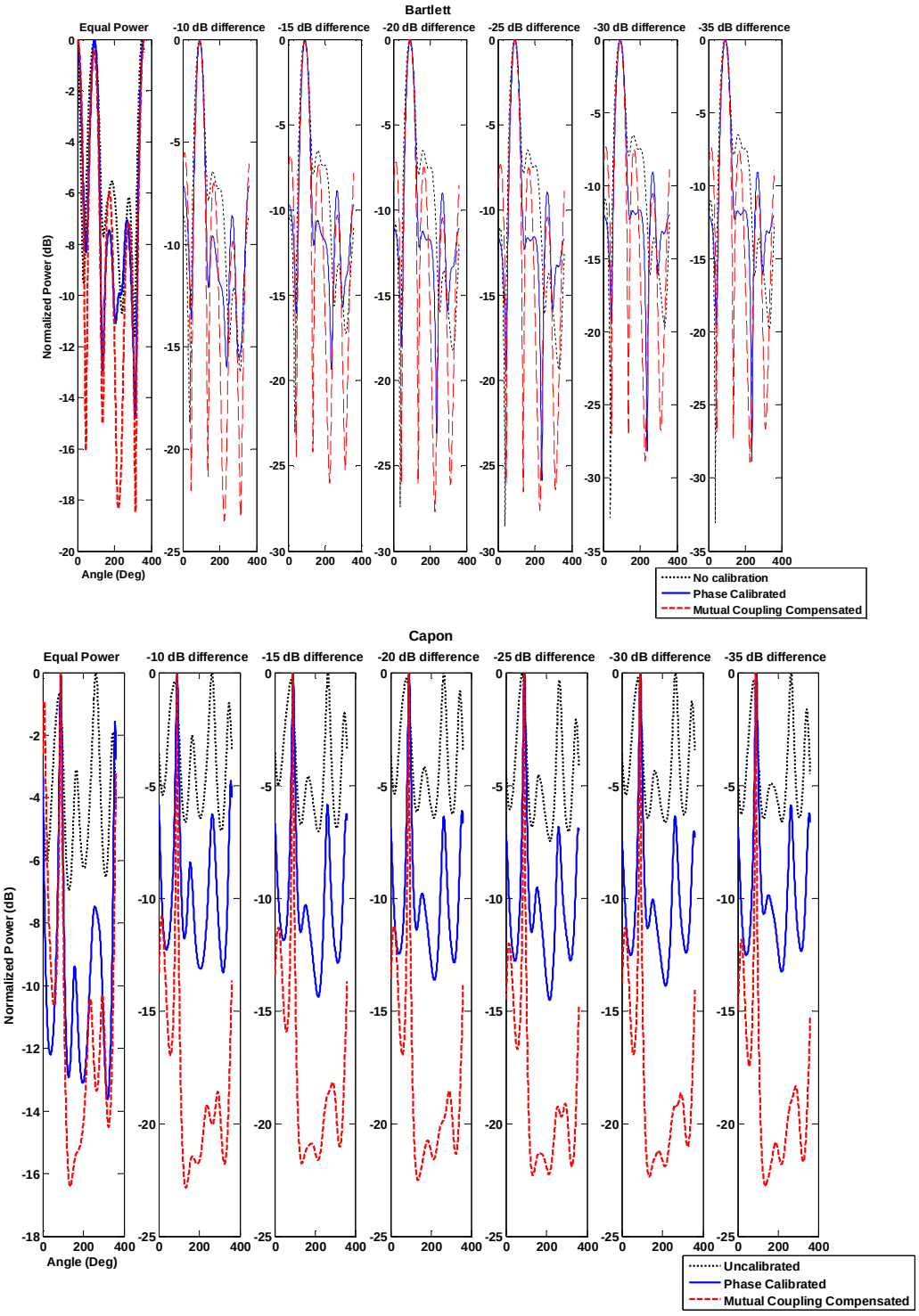
Bartlett
Equal Power
-10 dB difference
-15 dB difference
-20 dB difference
-25 dB difference
-30 dB difference
-35 dB difference
Normalized Power (dB)
Angle (Deg)
No calibration
Phase Calibrated
Mutual Coupling Compensated
Capon
Equal Power
-10 dB difference
-15 dB difference
-20 dB difference
-25 dB difference
-30 dB difference
-35 dB difference
Normalized Power (dB)
Angle (Deg)
Uncalibrated
Phase Calibrated
Mutual Coupling Compensated

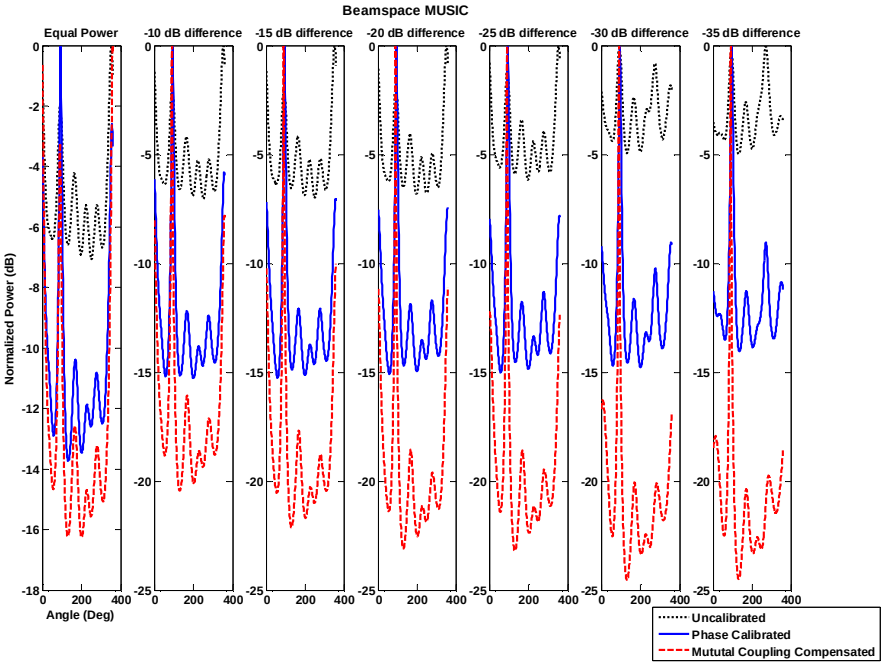
Beamspace MUSIC
Equal Power
-10 dB difference
-15 dB difference
-20 dB difference
-25 dB difference
-30 dB difference
-35 dB difference
Normalized Power (dB)
Angle (Deg)
Uncalibrated
Phase Calibrated
Mututal Coupling Compensated

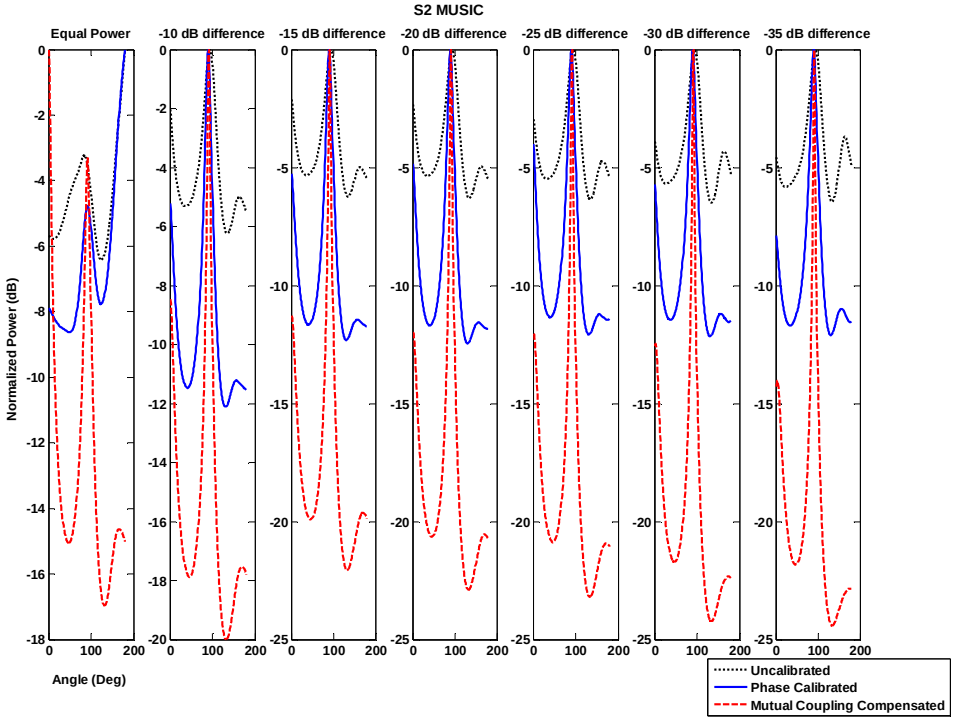
S2 MUSIC
Equal Power
-10 dB difference
-15 dB difference
-20 dB difference
-25 dB difference
-30 dB difference
-35 dB difference
Normalized Power (dB)
Angle (Deg)
Uncalibrated
Phase Calibrated
Mutual Coupling Compensated

APPENDIX C

MATLAB CODE

Algorithms base codes

Multiple algorithms based code, including

[46] Bartlett

[47] Capon

[48] MUSIC

[49] Adapted angular response

[50] Thermal noise algorithms

[51] Maximum entropy

```
%%%%%%%%%%%%%%%%%%%%%%%%%%%%%%%%%%%%%%%%%%%%%%%%%%%%%%%%%%%%%%%%%%%%%%%%

function [P_Bar_dB,P_MEM_dB,P_AAR_dB,P_MLM_dB,P_TNA_dB,P_Music_dB_EVD] =
many_alg(az1,az2,elements,power1,power2,noise,sector,samples)


Phi1 = az1;                     % Azimuth angled of the first incoming signal
Phi2 = az2;                     % Azimuth angled of the second incoming
signal
elements = elements;            % elements in antenna
ant_radius = 0.3812*elements;   % Antanna radius
P1 = power1;                    % Power of the first incoming signal
P2 = power2;                    % power of the second incoming signal
Noise_P = noise;                % noise power
Sector = sector;                % number of sectors to scan
SamPles = samples;              % Number of samples

%%% constant definition

f = 5.8e9;              %% operating frequency
c = 2.998e8;            %% speed of light
lamda = c/f;            %% operating wavelength
beta = (2*pi)/lamda;    %% wave number
eta = 120*pi;
theta = pi/2;           %% Elevation angle

%%% Sampling parameters

Win_per = SamPles/f;
```

```
T = 1/(f);
Samp = floor(Win_per/T);
t = linspace(0,Win_per,Samp);
theta = pi/2;          %% Elevation angle

%%% Sectors Spliting

k = 1:Sector;
for i = 1:elements;
   a_t(i,:) = exp(j*ant_radius*sin(theta)*cos(k*2*(pi/Sector)-
(2*(pi/elements)*i)));
end


%%% Array received signals and noise

S_t1 = (P1)*(exp(j*4*pi*f*t));
S_t2 = sqrt(P2)*(1+wgn(1,Samp,P2,'linear','complex'));
NoiSe = wgn(elements,Samp,Noise_P,'linear','complex');
x_t = a_t(:,Phi1)*S_t1 +a_t(:,Phi2)*S_t2 + NoiSe ;
Rxx = x_t*ctranspose(x_t)/Samp;


%%% Beam scan algorithm

P_Barlett = ctranspose(a_t)*Rxx*a_t;
P_barlett_spectrum = diag(P_Barlett);
P_Bar_norm = P_barlett_spectrum/max(P_barlett_spectrum);
P_Bar_dB = 10*log10(abs(P_Bar_norm));

%%% maximum entropy

iden = eye(elements,elements);


P_MEM =
1./(ctranspose(a_t)*inv(Rxx)*iden(1,:)'*ctranspose(iden(1,:)')*ctranspose(inv
(Rxx))*a_t);
P_MEM_spec = diag (P_MEM);
P_MEM_norm = P_MEM_spec/max(P_MEM_spec);
P_MEM_dB = 10*log10(abs(P_MEM_norm));


%%% Adapted angular response

P_AAR = ctranspose(a_t)*inv(Rxx)*a_t./(ctranspose(a_t)*inv(Rxx^2)*a_t);
P_AAR_spec = diag (P_AAR);
P_AAR_norm = P_AAR_spec/max(P_AAR_spec);
```

```
P_AAR_dB = 10*log10(abs(P_AAR_norm));


%%% Maximum likelihood (capon)

P_MLM = 1./(ctranspose(a_t)*inv(Rxx)*a_t);
P_MLM_spec = diag (P_MLM);
P_MLM_norm = P_MLM_spec/max(P_MLM_spec);
P_MLM_dB = 10*log10(abs(P_MLM_norm));


%%% thermal noise algorithm

P_TNA = 1./(ctranspose(a_t)*inv(Rxx^2)*a_t);
P_TNA_spec = diag (P_TNA);
P_TNA_norm = P_TNA_spec/max(P_TNA_spec);
P_TNA_dB = 10*log10(abs(P_TNA_norm));

%%% Multiple signal classification

[eig_VEC,diag_vec] = eig(Rxx);
[eigvals,ix] = sort(diag(diag_vec),'descend');
eig_VEC = eig_VEC(:,ix);
En = eig_VEC(:,3:elements);
P_Music =
1./(ctranspose(a_t)*eig_VEC(:,3:elements)*ctranspose(eig_VEC(:,3:elements))*a
_t);
P_Music_spectrum = diag(P_Music);
P_Music_norm = P_Music_spectrum/max(P_Music_spectrum);
P_Music_dB_EVD= 10*log10(abs(P_Music_norm));

figure
plot(P_Bar_dB)
hold on
plot(P_MEM_dB,'r')
plot(P_AAR_dB,'g')
plot(P_MLM_dB,'k')
plot(P_TNA_dB,'r:')
plot(P_Music_dB_EVD,'y')

%%%%%%%%%%%%%%%%%%%%%%%%%%%%%%%%%%%%%%%%%%%%%%%%%%%%%%%%%%%%%%%%%%%%%%%
Beamspace
%%%%%%%%%%%%%%%%%%%%%%%%%%%%%%%%%%%%%%%%%%%%%%%%%%%%%%%%%%%%%%%%%%%%%%%

function [P_Music_beam_dB] =
beamspace_MUSIC(Phi1,Phi2,elements,P1,P2,Noise,Sector,Points,Modes)

Phi1 = Phi1;                    % Azimuth angled of the first incoming signal
```

```
Phi2 = Phi2;                    % Azimuth angled of the second incoming
signal
elements = elements;            % elements in antenna
ant_radius = 0.3812*elements;   %ant_radius;% 3; % Antanna radius
P1 = 10^(P1/10);                % Power of the first incoming signal
P2 = 10^(P2/10);                % power of the second incoming signal
Noise_P = 10^(Noise/10);        % noise power
Sector = Sector;                % number of sectors to scan
SamPles = Points;               % Number of samples
if Phi1 == 0
    Phi1 = 360;
end

if Phi2 == 0
    Phi2 = 360;
end


%%% constant definition

f = 5.8e9;              %% operating frequency
c = 2.998e8;           %% speed of light
lamda = c/f;           %% operating wavelength
beta = (2*pi)/lamda;   %% wave number
eta = 120*pi;
theta = pi/2;          %% Elevation angle

%%% Sampling parameters

Win_per = SamPles/f;
T = 1/(f);
Samp = floor(Win_per/T);
t = linspace(0,Win_per,Samp);
theta = pi/2;          %% Elevation angle
%%% Sectors Spliting

k = 1:Sector;
for i = 1:elements;
   a_t(i,:) = exp(1i*ant_radius*sin(theta)*cos(k*2*(pi/Sector)-
(2*(pi/elements)*i)));
end


%%% Array received signals and noise

S_t1 = (P1)*(exp(j*4*pi*f*t));
S_t2 = sqrt(P2)*(1+wgn(1,Samp,P2,'linear','complex'));
NoiSe = wgn(elements,Samp,Noise_P,'linear','complex');
x_t = a_t(:,Phi1)*S_t1 +a_t(:,Phi2)*S_t2 + NoiSe ;
```

```
Rxx = x_t*ctranspose(x_t)/Samp;


%%% beamspace real MUSIC for UCA

%%% define the weight vector
n = 1:1:elements;
sy = (2*pi*n)/elements;
Modes = Modes;


%%% generating the mode vector
M1 = -Modes:1:0;
M2 = -1:-1:-Modes;
MM = cat(2,M1,M2);

%%% Weight vector
Cv = diag(1i.^(MM));
vec_count = 0;
for i = -Modes:1:Modes
vec_count = vec_count+1;
    V(:,vec_count) =sqrt(elements)*(1/elements)*exp(1i*i*sy)';
end


Feh = Cv*V';

%%% genetating the Beamspace manifold

a_bs = Feh*a_t;

%%% one can also generetate a_bs by using bessel function as follows:

ModeSS = Modes:1:Modes;
bess = diag(besselj(ModeSS,ant_radius));
vec_count = 0;
kk = 1:Sector;
for i = -Modes:1:Modes;
    vec_count = vec_count+1;
    v_phi(vec_count,:) =
sqrt(elements)*exp(1i*ant_radius*sin(theta)*cos(k*2*(pi/Sector)-
(2*(pi/elements)*i)));
end


%%% getting W that has centro hermitian rows
M_prim = 2*Modes +1;
ss = -Modes:1:Modes;
```

```
max_beam_num = 2*Modes+1;
beam_num = 1:1:max_beam_num;
W_ch = (1/sqrt(M_prim))*exp(-1i*ss'*beam_num);


Frh = W_ch'*Feh;
b_theta = Frh*a_t;

y_t = Frh*x_t;
Ryy = y_t*ctranspose(y_t);
Ryy_real = real(Ryy);

[eig_VEC_beam,diag_vec_beam] = eig(Ryy_real);
[eigvals_beam,ix_beam] = sort(diag(diag_vec_beam),'descend');
eig_VEC_beam = eig_VEC_beam(:,ix_beam);
En_beam = eig_VEC_beam(:,3:max_beam_num);
P_Music_beam = 1./(ctranspose(b_theta)*En_beam*ctranspose(En_beam)*b_theta);
P_Music_spectrum_beam = diag(P_Music_beam);
P_Music_norm_beam = P_Music_spectrum_beam/max(P_Music_spectrum_beam);
P_Music_beam_dB = 10*log10(P_Music_norm_beam);

%%%%%%%%%%%%%%%%%%%%%%%%%%%%%%%%%%%%%%%%%%%%%%%%%%%%%%%%%%%%%%%%%%%%%%%
```

Spatial Selective MUSIC base algorithm

```
%%%%%%%%%%%%%%%%%%%%%%%%%%%%%%%%%%%%%%%%%%%%%%%%%%%%%%%%%%%%%%%%%%%%%%%

function [angle_music1,angle_music2,angle_s2_music1, angle_s2_music2] =
S2MUSIC_two_sig(angle1,angle2,elements,P1,P2,Noise,points,var_elem,bb,bbb)


% clear all

format long

Phi1 = angle1*10;  % Azimuth angled of the first incoming signal
Phi2 = angle2*10;  % Azimuth angled of the second incoming signal

if Phi1 == 0
    Phi1 = 3600;
end

if Phi2 == 0
    Phi2 = 3600;
end
```

```
ant_radius = 0.3812*elements; % Antanna radius
P1 = 10^(P1/10);              % Power of the first incoming signal
P2 = 10^(P2/10);              % power of the second incoming signal
Noise_P = 10^(Noise/10);      % noise power
Sector = 3600;                % number of sectors to scan
SamPles = points;             % Number of samples

%%% constant definition

f = 5.8e9;              %% operating frequency
c = 2.998e8;            %% speed of light

%%% Sampling parameters

Win_per = SamPles/f;
T = 1/(f);
Samp = floor(Win_per/T);
t = linspace(0,Win_per,Samp);
theta = pi/2;          %% Elevation angle
%%% Sectors Spliting

k = 1:Sector;
for i = 1:elements;
   a_t2(i,:) = exp(j*ant_radius*sin(theta)*cos(k*2*(pi/Sector)-
(2*(pi/elements)*i)));
end

%%% Array received signals and noise

S_t1 = (P1)*(exp(j*4*pi*f*t));
S_t2 = sqrt(P2)*(1+wgn(1,Samp,P2,'linear','complex'));
NoiSe = wgn(elements,Samp,Noise_P,'linear','complex');
x_t = a_t(:,Phi1)*S_t1 + NoiSe + a_t(:,Phi2)*S_t2;


var_elem = 5;

    if var_elem == 3
        if locs_1(1)>=1 && locs_1(1)<=90
            shift_S2 = 0;
            x_t1 = x_t(1:3,:);
            Rxx1 =   1/size(x_t1,2) *x_t1 * x_t1';
            a_t_s2 = a_t2(1:3,1:90);
            a_t_s2_corr = a_s2_corr1(1:3,1:90);
        elseif locs_1(1)>=91 && locs_1(1)<=180
            shift_S2 = 90;
            x_t1 = x_t(3:5,:);
            Rxx1 =   1/size(x_t1,2) *x_t1 * x_t1';
```

```
        a_t_s2 = a_t2(3:5,91:180);
        a_t_s2_corr = a_s2_corr1(3:5,91:180);
    elseif locs_1(1)>=181 && locs_1(1)<=240
        shift_S2 = 180;
        x_t1 = x_t(5:7,:);
        Rxx1 =   1/size(x_t1,2) *x_t1 * x_t1';
        a_t_s2 = a_t2(5:7,181:270);
        a_t_s2_corr = a_s2_corr1(1:3,181:270);%91:180);
    elseif locs_1(1)>=241 && locs_1(1)<=360
        shift_S2 = 240;
        x1 = x_t(6:8,:);
        Rxx1 =   1/size(x_t1,2) *x_t1 * x_t1';
        a_t_s2 = a_t2(6:8,271:360);
        a_t_s2_corr = a_s2_corr1(6:8,271:360);
    end

elseif var_elem == 4
    if locs_1(1)>=1 && locs_1(1)<=120
        shift_S2 = 0;
        x_t1 = x_t(1:4,:);
        Rxx1 =   1/size(x_t1,2) *x_t1 * x_t1';
        a_t_s2 = a_t2(1:4,1:120);
        a_t_s2_corr = a_s2_corr1(1:4,1:120);
    elseif locs_1(1)>=121 && locs_1(1)<=240
        shift_S2 = 120;
        x_t1 = x_t(4:7,:);
        Rxx1 =   1/size(x_t1,2) *x_t1 * x_t1';
        a_t_s2 = a_t2(4:7,121:240);
        a_t_s2_corr = a_s2_corr1(4:7,121:240);
    elseif locs_1(1)>=241 && locs_1(1)<=360
        shift_S2 = 240;
        x_t1 = x_t(5:8,:);
        Rxx1 =   1/size(x_t1,2) *x_t1 * x_t1';
        a_t_s2 = a_t2(5:8,241:360);
        a_t_s2_corr = a_s2_corr1(5:8,241:360);
    end
elseif var_elem == 5
    if locs_1(1)>=1 && locs_1(1)<=180
        shift_S2 = 0;
        x_t1 = x_t(1:5,:);
        Rxx1 =   1/size(x_t1,2) *x_t1 * x_t1';
        a_t_s2 = a_t2(1:5,1:180);
        a_t_s2_corr = a_s2_corr1(1:5,1:180);
    elseif locs_1(1)>=181 && locs_1(1)<=360
        shift_S2 = 180;
        x_t1 = x_t(4:8,:);
        Rxx1 =   1/size(x_t1,2) *x_t1 * x_t1';
        a_t_s2 = a_t2(4:8,181:360);
        a_t_s2_corr = a_s2_corr1(4:8,181:360);
    end
end
```

```
%%% S2 MUSIC spetrum generation

[eig_VEC1,diag_vec1] = eig(Rxx1);
[eigvals1,ix1] = sort(diag(diag_vec1),'descend');
eig_VEC1 = eig_VEC1(:,ix1);
En1 = eig_VEC1(:,2:length(Rxx1));

P_S2_Music = 1./(ctranspose(a_t_s2)*En1*ctranspose(En1)*a_t_s2);
P_S2_Music_spectrum = diag(P_S2_Music);
P_S2_Music_norm = P_S2_Music_spectrum/max(P_S2_Music_spectrum);
P_S2_Music_dB =  10*log10(abs(P_S2_Music_norm));

figure
title('S2-MUSIC')
subplot(2,9,loop-18)
x_ax = linspace(1,180,180);
plot(x_ax+shift_S2,P_S2_Music_dB);

%%%%%%%%%%%%%%%%%%%%%%%%%%%%%%%%%%%%%%%%%%%%%%%%%%%%%%%%%%%%%%%%%%%%%%%
```

Element spacing varying code example

```
%%%%%%%%%%%%%%%%%%%%%%%%%%%%%%%%%%%%%%%%%%%%%%%%%%%%%%%%%%%%%%%%%%%%%%%

%%%% fixed SNR = 10
%%% var element spacing

for xx = 1:200

    [P_Bar_dB,P_cap_dB,P_Music_dB,P_S2_Music_dB] =
S2MUSIC(45,8,10,0,1000,5,1,1,0.1);
    P_Bar_dB_p1(:,xx) = P_Bar_dB;
    P_cap_dB_p1(:,xx) = P_cap_dB;
    P_Music_dB_p1(:,xx) = P_Music_dB;
    P_S2_Music_dB_p1(:,xx) = P_S2_Music_dB;
```

```
end
save('lamda_var_p1',
'P_Bar_dB_p1','P_cap_dB_p1','P_Music_dB_p1','P_S2_Music_dB_p1')

%% note that the above loop is repeated for varying elements spacing which is
the last variable in the function's parameter


%%%%%%%%%%%%%%%%%%%%%%%%%%%%%%%%%%%%%%%%%%%%%%%%%%%%%%%%%%%%%%%%%%%%%%%%%%%

%%% Beamspace

for xx = 1:200
    P_Music_beam_dB = beamspace_singlesource(45,8,10,0,3600,1000,7,0.1);
    P_Beam_p1(:,xx) = P_Music_beam_dB;
end
save('lamda_var_beam_p1', 'P_Beam_p1')
clear all
```

Processing example

```
%%%%%%%%%%%%%%%%%%%%%%%%%%%%%%%%%%%%%%%%%%%%%%%%%%%%%%%%%%%%%%%%%%%%%%%%%%%

clear all
load lamda_var_p1
load lamda_var_beam_p1
for i = 1:200
     [x_bar,locs_bar] =findpeaks(real(P_Bar_dB_p1(:,i)),'sortstr','descend');
     [x_cap,locs_cap] =findpeaks(real(P_cap_dB_p1(:,i)),'sortstr','descend');
     [x_music,locs_music]
=findpeaks(real(P_Music_dB_p1(:,i)),'sortstr','descend');
     [x_s2,locs_s2]
=findpeaks(real(P_S2_Music_dB_p1(:,i)),'sortstr','descend');
     [x_beam,locs_beam] =findpeaks(real(P_Beam_p1(:,i)),'sortstr','descend');
      bar(i) = locs_bar(1);
      cap(i) = locs_cap(1);
      music(i) = locs_music(1);
      s2(i) = locs_s2(1);
      beam(i) = locs_beam(1);
end
MSE_bar_p1 = sqrt(sum(abs(bar-450))/200);
MSE_cap_p1 = sqrt(sum(abs(cap-450))/200);
MSE_music_p1 = sqrt(sum(abs(music-450))/200);
MSE_s2_p1 = sqrt(sum(abs(s2-450))/200);
MSE_beam_p1 = sqrt(sum(abs(beam-450))/200);


save('MSE_p1','MSE_bar_p1','MSE_cap_p1','MSE_music_p1','MSE_s2_p1','MSE_beam_
p1')
```

```
%%% on a different m file the saved variables are loaded and organized for
plotting

factor = [0.1 0.2 0.3 0.4 0.5 0.6 0.7 0.8 0.9 1 1.1 1.2 1.3 1.4 1.5 ];

MSE_all_bar = [MSE_bar_p1 MSE_bar_p2 MSE_bar_p3 MSE_bar_p4 MSE_bar_p5
MSE_bar_p6 MSE_bar_p7 MSE_bar_p8 MSE_bar_p9 ...
    MSE_bar_1 MSE_bar_1p1 MSE_bar_1p2 MSE_bar_1p3 MSE_bar_1p4 MSE_bar_1p5];
MSE_all_cap = [MSE_cap_p1 MSE_cap_p2 MSE_cap_p3 MSE_cap_p4 MSE_cap_p5
MSE_cap_p6 MSE_cap_p7 MSE_cap_p8 MSE_cap_p9 ...
    MSE_cap_1 MSE_cap_1p1 MSE_cap_1p2 MSE_cap_1p3 MSE_cap_1p4 MSE_cap_1p5];
MSE_all_music = [MSE_music_p1 MSE_music_p2 MSE_music_p3 MSE_music_p4
MSE_music_p5 MSE_music_p6 MSE_music_p7 MSE_music_p8 MSE_music_p9 ...
    MSE_music_1 MSE_music_1p1 MSE_music_1p2 MSE_music_1p3 MSE_music_1p4
MSE_music_1p5];
MSE_all_s2 = [MSE_s2_p1 MSE_s2_p2 MSE_s2_p3 MSE_s2_p4 MSE_s2_p5 MSE_s2_p6
MSE_s2_p7 MSE_s2_p8 MSE_s2_p9 ...
    MSE_s2_1 MSE_s2_1p1 MSE_s2_1p2 MSE_s2_1p3 MSE_s2_1p4 MSE_s2_1p5];
MSE_all_beam = [MSE_beam_p1 MSE_beam_p2 MSE_beam_p3 MSE_beam_p4 MSE_beam_p5
MSE_beam_p6 MSE_beam_p7 MSE_beam_p8 MSE_beam_p9 ...
    MSE_beam_1 MSE_beam_1p1 MSE_beam_1p2 MSE_beam_1p3 MSE_beam_1p4
MSE_beam_1p5];


figure

plot(factor,MSE_all_bar/10,':*')
hold on
plot(factor,MSE_all_cap/10,'r')
plot(factor,MSE_all_music/10,'k')
plot(factor,MSE_all_s2/10,'g:')
plot(factor,MSE_all_beam/10,'m')
plot(0.37*ones(1,length(factor)),linspace(0,0.14,length(factor)),':')
legend('Bartlett','Maximum likelihood','MUSIC','S2 MUSIC','Beamspace MUSIC')
xlabel('Element spacing factor (Lamda)')
ylabel('RMSE (deg)')


%%%%%%%%%%%%%%%%%%%%%%%%%%%%%%%%%%%%%%%%%%%%%%%%%%%%%%%%%%%%%%%%%%%%%%%%
```

Example code for resolution as the number of sampling is the variable, here the number of samples used is 100 and is highlighted, “hist” and “imagesc” were used to plot the results for better visualization of simulation results.

```
%%%%%%%%%%%%%%%%%%%%%%%%%%%%%%%%%%%%%%%%%%%%%%%%%%%%%%%%%%%%%%%%%%%%%%%%%%%%%

%function [P_Bar_dB,P_cap_dB,P_Music_dB,P_S2_Music_dB,P_Music_beam_dB] =
%S2MUSIC_two_sig(angle1,angle2,elements,P1,P2,Noise,sect,points,var_elem,bb,b
%bb,del_f,Modes)

clear all

for i = 1:360

[P_Bar_dB,P_cap_dB,P_Music_dB,P_S2_Music_dB,P_Music_beam_dB] =
S2MUSIC_two_sig(180,i,8,20,20,0,360,100,5,1,1,10e6,7);

P_Bar_dB_10(:,i) =  P_Bar_dB;
P_cap_dB_10(:,i) = P_cap_dB;
P_Music_dB_10(:,i)= P_Music_dB;
P_S2_Music_dB_10(:,i) = P_S2_Music_dB;
P_Music_beam_dB_10(:,i) = P_Music_beam_dB;

end




save('res_samp_10','P_Bar_dB_10','P_cap_dB_10','P_Music_dB_10','P_S2_Music_dB
_10','P_Music_beam_dB_10')
%%%% Bartlett
for i = 1:360
        [x_bar,locs_bar]
=findpeaks(real(P_Bar_dB_10(:,i)),'sortstr','descend','minpeakheight',-25);
    for h = 1:length(locs_bar)
        locs_Bar(i,h) = locs_bar(h);
        x_Bar(i,h) = x_bar(h);
    end
    if length(locs_Bar) > 1
        if i < 180
            if locs_Bar(i,1)>locs_Bar(i,2)
            switCH1 = locs_Bar(i,2);
            switCH2 = x_Bar(i,2);
            locs_Bar(i,2) = locs_Bar(i,1);
            locs_Bar(i,1) = switCH1;
            x_Bar(i,2) = x_Bar(i,1);
            x_Bar(i,1) = switCH2;

            end
        if i > 180
            if locs_Bar(i,1)<locs_Bar(i,2)
            switCH1 = locs_Bar(i,2);
             switCH2 = x_Bar(i,2);
```

```
            locs_Bar(i,2) = locs_Bar(i,1);
            locs_Bar(i,1) = switCH1;
            x_Bar(i,2) = x_Bar(i,1);
            x_Bar(i,1) = switCH2;
            end
        end
        end
        end
 end
%%%% ML
for i = 1:360
        [x_cap,locs_cap]
=findpeaks(real(P_cap_dB_10(:,i)),'sortstr','descend','minpeakheight',-25);
    for h = 1:length(locs_cap)
        locs_Cap(i,h) = locs_cap(h);
        x_Cap(i,h) = x_cap(h);
    end
    if length(locs_Cap) > 1
        if i < 180
            if locs_Cap(i,1)>locs_Cap(i,2)
            switCH1 = locs_Cap(i,2);
            switCH2 = x_Cap(i,2);
            locs_Cap(i,2) = locs_Cap(i,1);
            locs_Cap(i,1) = switCH1;
            x_Cap(i,2) = x_Cap(i,1);
            x_Cap(i,1) = switCH2;

            end
        if i > 180
            if locs_Cap(i,1)<locs_Cap(i,2)
            switCH1 = locs_Cap(i,2);
             switCH2 = x_Cap(i,2);
            locs_Cap(i,2) = locs_Cap(i,1);
            locs_Cap(i,1) = switCH1;
            x_Cap(i,2) = x_Cap(i,1);
            x_Cap(i,1) = switCH2;
            end
        end
        end
        end
 end

%%%% MUSIC
for i = 1:360
        [x_music,locs_music]
=findpeaks(real(P_Music_dB_10(:,i)),'sortstr','descend','minpeakheight',-25);
    for h = 1:length(locs_music)
        locs_Music(i,h) = locs_music(h);
        x_Music(i,h) = x_music(h);
    end
    if length(locs_Music) > 1
```

```
        if i < 180
            if locs_Music(i,1)>locs_Music(i,2)
            switCH1 = locs_Music(i,2);
            switCH2 = x_Music(i,2);
            locs_Music(i,2) = locs_Music(i,1);
            locs_Music(i,1) = switCH1;
            x_Music(i,2) = x_Music(i,1);
            x_Music(i,1) = switCH2;

            end
        if i > 180
            if locs_Music(i,1)<locs_Music(i,2)
            switCH1 = locs_Music(i,2);
             switCH2 = x_Music(i,2);
            locs_Music(i,2) = locs_Music(i,1);
            locs_Music(i,1) = switCH1;
            x_Music(i,2) = x_Music(i,1);
            x_Music(i,1) = switCH2;
            end
        end
        end
        end
 end
%%%%% Beam


for i = 1:360
        [x_beam,locs_beam]
=findpeaks(real(P_Music_beam_dB_10(:,i)),'sortstr','descend','minpeakheight',
-25);
    for h = 1:length(locs_beam)
        locs_Beam(i,h) = locs_beam(h);
        x_Beam(i,h) = x_beam(h);
    end
    if length(locs_Beam) > 1
        if i < 180
            if locs_Beam(i,1)>locs_Beam(i,2)
            switCH1 = locs_Beam(i,2);
            switCH2 = x_Beam(i,2);
            locs_Beam(i,2) = locs_Beam(i,1);
            locs_Beam(i,1) = switCH1;
            x_Beam(i,2) = x_Beam(i,1);
            x_Beam(i,1) = switCH2;

            end
        if i > 180
            if locs_Beam(i,1)<locs_Beam(i,2)
            switCH1 = locs_Beam(i,2);
             switCH2 = x_Beam(i,2);
            locs_Beam(i,2) = locs_Beam(i,1);
```

```
            locs_Beam(i,1) = switCH1;
            x_Beam(i,2) = x_Beam(i,1);
            x_Beam(i,1) = switCH2;
            end
        end
        end
        end
 end

%%%% S2


 for i = 1:225
        [x_s2,locs_s2]
=findpeaks(real(P_S2_Music_dB_10(:,i)),'sortstr','descend','minpeakheight',-
25);
    for h = 1:length(locs_s2)
        locs_S2(i,h) = locs_s2(h);
        x_S2(i,h) = x_s2(h);
    end
    if length(locs_S2) > 1
        if i < 180
            if locs_S2(i,1)>locs_S2(i,2)
            switCH1 = locs_S2(i,2);
            switCH2 = x_S2(i,2);
            locs_S2(i,2) = locs_S2(i,1);
            locs_S2(i,1) = switCH1;
            x_S2(i,2) = x_S2(i,1);
            x_S2(i,1) = switCH2;

            end
        if i > 180
            if locs_S2(i,1)<locs_S2(i,2)
            switCH1 = locs_S2(i,2);
             switCH2 = x_S2(i,2);
            locs_S2(i,2) = locs_S2(i,1);
            locs_S2(i,1) = switCH1;
            x_S2(i,2) = x_S2(i,1);
            x_S2(i,1) = switCH2;
            end
        end
        end
        end
 end

histbar = hist(locs_Bar.',[1:360]);
histcap = hist(locs_Cap.',[1:360]);
histmusic = hist(locs_Music.',[1:360]);
histbeam = hist(locs_Beam.',[1:360]);
hists2 = hist(locs_S2.',[1:225]);
```

```
figure
% axes('FontWeight','bold','FontSize',14)
subplot(3,2,1)
imagesc(histbar.',[0,10]);
title('Bartlett Histogram','FontSize',14,'FontWeight','bold')
ylabel('Set Angle [deg]','FontSize',14,'FontWeight','bold')
xlabel('Detected Angle [deg]','FontSize',14,'FontWeight','bold')
subplot(3,2,2)
imagesc(histcap.',[0,10]);
title('ML Histogram','FontSize',14,'FontWeight','bold')
ylabel('Set Angle [deg]','FontSize',14,'FontWeight','bold')
xlabel('Detected Angle [deg]','FontSize',14,'FontWeight','bold')
subplot(3,2,3)
imagesc(histmusic.',[0,10]);
title('MUSIC Histogram','FontSize',14,'FontWeight','bold')
ylabel('Set Angle [deg]','FontSize',14,'FontWeight','bold')
xlabel('Detected Angle [deg]','FontSize',14,'FontWeight','bold')
subplot(3,2,4)
imagesc(histbeam.',[0,10]);
title('Beamspace MUSIC Histogram','FontSize',14,'FontWeight','bold')
ylabel('Set Angle [deg]','FontSize',14,'FontWeight','bold')
xlabel('Detected Angle [deg]','FontSize',14,'FontWeight','bold')
subplot(3,2,5)
imagesc(hists2.',[0,10]);
title('S2 MUSIC Histogram','FontSize',14,'FontWeight','bold')
ylabel('Set Angle [deg]','FontSize',14,'FontWeight','bold')
xlabel('Detected Angle [deg]','FontSize',14,'FontWeight','bold')

cm = colormap(jet);
cm(1,:)=[1,1,1];
colormap(cm)

%%%%%%%%%%%%%%%%%%%%%%%%%%%%%%%%%%%%%%%%%%%%%%%%%%%%%%%%%%%%%%%%%%%%%%%%%%%
```